

Control of Magnetic Robots:
Solid Medium Transmission and Milli-Scale Magnetic Swimmer

by
Haoran Zhao

A dissertation submitted to the Department of Electrical and Computer Engineering,
Cullen College of Engineering
in partial fulfillment of the requirements for the degree of

Doctor of Philosophy
in Electrical Engineering

Chair of Committee: Dr. Aaron T. Becker

Committee Member: Dr. Han Zhu

Committee Member: Dr. Rose T. Faghih

Committee Member: Dr. Paul Ruchhoeft

Committee Member: Dr. Miao Pan

Committee Member: Dr. Julien Leclerc

University of Houston
December 2020

Copyright 2020, Haoran Zhao

ACKNOWLEDGEMENTS

Foremost, I would like to express my heartfelt thanks to my Ph.D. advisor Dr. Aaron T. Becker. I'm proudly grateful and fortunate to accept his gratitude offer to be one of his Ph.D. students and join his research lab. Dr. Becker has constantly shared his great passion for robotics and life, offered me valuable insights and inspirations, and trained my critical thinking ability to conquer the complex problem. All of the work presented in this dissertation could not have been possible without his support, advice, and encouragement.

I greatly appreciate Dr. Han Zhu, Dr. Rose T. Faghih, Dr. Paul Ruchhoeft, Dr. Miao Pan, and Dr. Julien Leclerc for being my defense committee members and offering insightful suggestions for my research. Thank Dr. Julien Leclerc for his wealth of experience in magnetics and control, who also always covered my back for providing such great support and help. It was a pleasure to work with him. I want to express my thanks to Dr. Nikolaos V. Tsekos and Dr. Liu Xin who have helped me with solid medium transmission (SMT) mechanism experiments, Michael J. Heffernan and Rahul Korpu, who have closely worked with me on designing and refining the 1-DoF and 2-DoF SMT manipulators.

Thanks to other co-authors of my work, Cristina Morales Mojica, Jose Velazco-Garcia, Ioannis Seimenis, Ernst LeissHabib M. Zaid, Dipan J. Shah, and Andrew Webb. I am thankful for my current and past colleagues and alumni of the Robotic Swarm Control Lab, Nick Anderson, Daniel Bao, Daniel Biediger, Shriya Bhatnagar, Javier Garcia, Rhema Ike, Benedict Isichei, Parth Joshi, Lillian Lin, Jarrett Lonsford, Arun Mahadev, Sheryl Manzoor, Victor Montano, An Nguyen, Adi Pasic, Dr. Shiva Shahrokhi, Steban Soto, Mohammad Sultan, Mable Wan, Mike Yannuzzi, and Dr. Li Huang. I am thankful to Dr. Robert S. Provence for introducing me to Dr. Becker.

Finally, this thesis is dedicated to my parents Juan Liu and Yimin Zhao, step-father Fuquan Gao, and my wife Yan Li for having so much love, care, support for me, and always being with me.

ABSTRACT

Magnetic robots show great potential for revolutionizing many aspects of medicine and clinical applications. The human body is transparent to a low-frequency magnetic field. Generally, a *low-frequency* is considered less than 300 Hz. Magnetic resonance imaging (MRI) systems typically use a maximum slew rate of 200 mT/m/ms to limit the frequency. MRI is a powerful *diagnostic* modality for interventions and surgeries. However, MRIs are not used for performing interventions because the MRI has a very high magnetic field and is size constrained. The MRI opening is typically a cylinder that is 30cm in diameter and must accommodate a patient, gradient coils, and the MRI bed. This dissertation provides the design and implementation of a remotely-driven, MR-compatible robotic manipulator, and a force transmission mechanism for controlling that robot.

Magnetism is also a promising modality for controlling robots. Magnetically actuated robots could perform minimally invasive surgery. Such robots could be employed for many clinical and biomedical applications, ranging from in vitro to in vivo applications of diagnosis and therapy. Part two of this dissertation examines the control, design optimization, and applications of a spiral-shaped magnetic robot. The primary application is focused on blood clot removal. For clot removal, magnetic robots should be controlled and navigated in 3D environments. This requires control algorithms for high accuracy path-following in 3D fluidic environments. The dissertation provides frameworks, design concepts, and control theories for accurate control during blood clot removal. A further change for clot removal is that the clots are removed deep inside the human body. These areas are not visible to cameras, so control of the robots requires imaging techniques. This dissertation presents a process using an ultrasound scanner mounted on a six-axis robot arm to image and tracking the 6 mm long by 2.5 mm diameter magnetic swimmer as it moving in models of human vasculature.

TABLE OF CONTENTS

ACKNOWLEDGEMENTS	iii
ABSTRACT	iv
LIST OF TABLES	vii
LIST OF FIGURES	ix
1 INTRODUCTION	1
1.1 Motivations and Objectives	1
1.2 Dissertation Organization	4
2 SOLID MEDIUM TRANSMISSION	6
2.1 Introduction	6
2.2 SMT Backbone	10
2.3 Friction in the SMT Mechanism	13
2.4 Preliminary Experiment Studies	15
2.4.1 Experimental Set-Up	15
2.4.2 Closed-Loop SMT Control	17
2.5 MR Studies	20
2.6 Design of SMT-Actuated Manipulators	23
2.6.1 Linear Manipulator	23
2.6.2 Rotation-Translation-Stage (RTS)	24
2.6.3 RTS Manipulator Kinematics	26
2.7 Two-DoF Manipulator Configuration Space	29
2.8 Experiment Studies on Manipulators	30
2.8.1 Experimental Set-Up	30
2.8.2 One-DoF Linear Manipulator Experiment Results	32
2.8.3 Two-DoF Manipulator Experiment Results	34
3 MILLI-SCALE MAGNETIC SWIMMER	36
3.1 Introduction	36
3.2 Magnetic Field Control	38
3.2.1 Magnetic Manipulator	38
3.2.2 Magnetic Field	40
3.2.3 Inverse Magnetics Calculation	40
3.2.4 Gradient Force Compensation	43
3.3 Preliminary Study on Pure Spiral-type Swimmer	46
3.3.1 Closed-loop PI Controller	47
3.3.2 Swimmer Design and Fabrication	48
3.3.3 Experimental Optimization on Swimmer Design	49
3.4 3D Navigation with PI Controller	51
3.4.1 Preliminary 3D Navigation Study with PI Controller	51
3.4.2 Orientation Controller	51
3.4.3 3D Navigation Study with PI Controller and Orientation Controller	54
3.5 3D Navigation with Adaptive Control	54

3.5.1	Experimental Setup	55
3.5.2	Optimization Studies on Helical Tip Design	56
3.5.3	Model Reference Adaptive Control(MRAC)	57
3.5.4	Controller Comparison	60
3.5.5	Path-Following Using MRAC	61
3.6	In Vitro Clinical Application Studies	63
3.6.1	Motivation of Blood Clot Removal Studies	63
3.6.2	Blood Clot Removal In Vitro Study	64
3.6.3	In Vitro Study Results	65
3.6.4	Combined 3D Navigation and Blood Clot Removal	67
4	ULTRASOUND GUIDANCE STUDIES	69
4.1	Introduction	69
4.2	Robot Arm Control	70
4.2.1	Kinematics of UR3	70
4.2.2	Hybrid Control	75
4.2.3	Preliminary Results of Hybrid Control	76
4.3	Ultrasound Image Detection	78
4.3.1	Ultrasound Programming	79
4.3.2	Swimmer Detection	88
4.4	Experimental Studies	95
4.4.1	Experimental Setup	95
4.4.2	Swimmer Detection Implementation	97
4.4.3	1D Tracking Studies	98
5	CONCLUSION	100
5.1	Conclusion	100
5.2	Future Work	103
	BIBLIOGRAPHY	105

LIST OF TABLES

1	The Spiral-type Swimmer Designs	55
2	Controller Comparison	56
3	Comparison between the removal rate of different swimmer designs at 45 Hz. A single test was performed for each design. Design B has the highest removal rate. Legend: ■ = diamond powder, □ = acrylate, ■ = drill bit.	66
4	UR3 DH Parameters	73

LIST OF FIGURES

1	(a) and (b) illustrates the solid medium transmission (SMT). (c) shows a milli-scale magnetic swimmer.	1
2	SMT schematics: (a) illustrates the pattern of SMT sphere packing. (b) illustrates the combination of SMT using spacer and sphere. (c) shows the sphere zigzag packing pattern. (d) presents sphere and spacer zigzag packing pattern. The spacers are hollow along central axis and the spheres fit partly inside the spacer.	8
3	One-DoF manipulator driven by SMT mounted on an UR3 robot arm. The flexible transmission lines can follow the robot arm’s movement moving from the left-side to the right-side.	9
4	Compression ratios studies for tubing bend diameter $D_{\text{bend}} = 5D_{\text{sphere}}$: (a) Compression ratio for $ID_{\text{tube}} = D_{\text{sphere}}$ shown with a black dot. (b) Compression ratio when spheres and spacers are pushed to outside wall shown with a green triangle. (c) Compression ratio for zigzag packing shown with a red star.	12
5	SMT major component studyies: (a) length of SMT line. (b) Friction coefficients of materials. (c) Ratio of ID_{tube} and D_{sphere} . (d) length of interval spacer.	15
6	The experimental setups: (a) Block diagram of the system. (b) Photograph of the experimental platform.	16
7	Control studies and system identifications: (a) system output of a 20 mm step input. (b) system output of a 40 mm step input. (c) 3 rd order and 2 nd order models comparison. (d) The comparison of the estimated system error and experiment results.	18
8	SMT positioning control studies: (a) The mean and standard deviation of displacement error. (b) The mean and standard deviation of system response delay. Each data point contains 10 trials.	19
9	SMT MR compatibility results: (a) shows a snapshot of the MR marker. (b) - (d) show MRI frames of the marker driven by the manipulator.	21
10	The schematics of end loop actuator: (1) Upper stage. (2) Bottom stage (3) Inner lumen. (4) Screw hole. (5, 6) Channel end edges. (7, 8) are tubing fittings and adapters. (9) Carriage of optical encoder. (10) Slot in upper stage. (11) Piston. (12) Optical encoder strip. (13, 14) are Stop switches.	23
11	RTS 3D schematics: (1, 2) are the SMT tubing connectors. (3) is the screw holes. (4) is the optical encoder and strip to record translation motion. (5) is the optical encoder and strip to record rotation motion. (6) is the tool carriage. (7) is the inner channel of rotation. (8) is the inner block. (9) is the extended piston. (10) is the Mount slot. (11) is the inner channel of translation. (12) is the ball-and-socket A . (13) is the sprocket. (14) is a bridge connection. And (15) is the ball bearing.	24
12	Top and bottom views of Physical prototype model.	25
13	The RTS 3D schematics model and the coordinate frames for kinematic studies.	26
14	The workspace of two stacked RTS robots. (a) and (b) are the sector of bounded by 4 arcs. (c) and (d) is this workspace rotated about the z -axis.	28
15	Experimental setups: (a) Isometric view of RST (b) One-DoF isolation study (c) Motor & motor base (d) Electronics box.	31
16	System diagram of Two-DoF: (a) Control diagram (b) Signal flow.	32
17	Experimental results of One-DoF: (a) Response tim (b) Settling time. Each box-and-whisker marker concludes 10 trials.	33

18	Experimental results of RST: (a) The settling time of rotation. (b) MS-control results of rotation. (c) The settling time of translation. (d) MS-control results of translation.	35
19	(a) Helix shape. (b) Spiral shape. (c) Twist shape.	36
20	Lab-built magnetic system and schematics of magnetic swimmer. (a) The magnetic manipulator platform. (b) The cross section schematic. (c) The magnetic swimmer.	39
21	The Numerical study results of the relationship of the angle between actual and approximated magnetization of swimmer in the simulated workspace. The “app” stands “approximated” and “act” stands “actual.”	44
22	Experimental results of the Gradient force along circular paths.	46
23	System control and signal flow diagrams.	47
24	Different robot designs experimentally tested.	48
25	Maximum linear velocity vs Magnetic field rotational frequency of four robot robots. Each data point represents 10 trials.	49
26	Experimental results of path-following following experiments.	52
27	Path-following results by a helical swimmer. (A) 3D path-following results of two sets parameter values. (B) Path-following error. (C) and (D) show parameter studies on γ and β . Each data point represents 10 laps around the path.	53
28	Plot of the path followed by the millimeter-scale swimmer during navigation through a tube. On this figure, the swimmer completes the trajectory four times.	54
29	The PI controller Path-following results. (a) The path-following error. (b) The average error for each swimmer. Each marker represents 15 circular laps.	55
30	System diagrams: (a) The band-pass frequency of one coil. (b) and (c) are control and hardware diagrams.	57
31	The experimental results of the comparison between PI controller and MRAC. The desired trajectory is a circle with z -axis = 0 mm, radius = 60 mm.	61
32	Experimental results of two motion studies using MRAC controller. Both experiments include 10 trails.	62
33	Picture of three swimmers inside PDMS channels.	64
34	model fit of blood clot removal rate vs rotation frequency.	66
35	Snapshots from the video the combined 3D closed-loop path following and blood clot removal experiment.	68
36	The joint frames of UR robot.	71
37	Hybrid control architecture.	75
38	Schematics of ultrasound prob holder and fake model.	77
39	Preliminary results of hybride control: (a) shows the docking and tracking process, (b) presents the force recorded during the tracking.	78
40	Echogenicity results of the metal coating.	88
41	Ground truth study: The sequence images presented the Doppler detection results, which is aligned with the central axis of the ultrasound transducer.	89
42	Detection diagram.	91
43	System network.	95
44	Flow diagram of the system.	96
45	Hardware setup for 1D tracking study.	97
46	The flow diagram of the swimmer detection.	98
47	Sequence images of 1D tracking.	98

1 INTRODUCTION

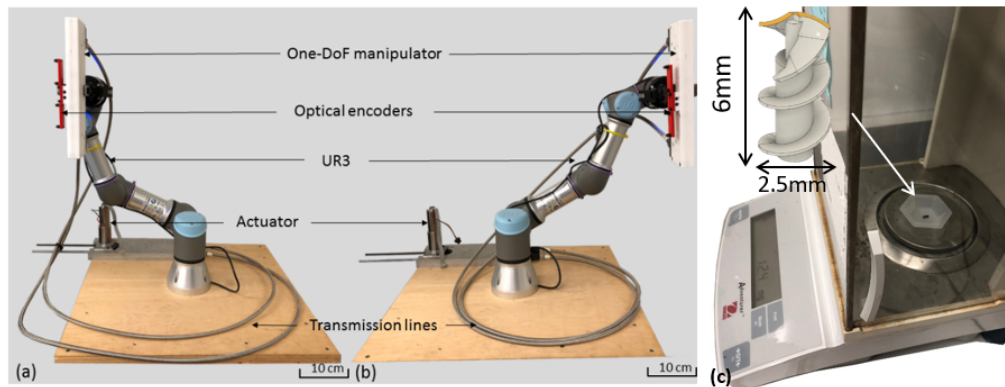


Figure 1: (a) and (b) illustrates the solid medium transmission (SMT). (c) shows a milli-scale magnetic swimmer.

This dissertation investigates two methods for the control of magnetic robots. Figure 1 (a) and (b) shows on left, a solid medium transmission (SMT). SMT is a technology used to use a normal electric motor outside an MRI to actuate a mechanism inside the bore of an MRI scanner. The first half of this dissertation (chapter 1-4) covers SMT robots. Figure 1 (c) shows a milli-scale magnetic swimmer, a 6 mm long device that, when immersed in liquid, and subjected to a rotating magnetic field, will propel itself through the liquid.

1.1 Motivations and Objectives

Untethered mobile milli- and micro-robots have great potential value in the aspects of healthcare, bioengineering, and medical applications. Untethered milli- and micro-robots are especially promising approaches for biological and medical tasks. Their size enables them to access milli-scale regions; the lack of tether enables them to reach remote locations. The robots can be equipped with a wide range of end-effectors to enable many functions.

They have many potential applications that include blood clot removal, cell manipulation, active disease diagnosis imaging, drug delivery, mobile in-situ sensing, targeted therapy, minimally invasive or non-invasive surgical interventions, and more. There are two major approaches for designing, fabricating, and controlling untethered mobile small-scale robots. Our work mainly focuses on the *off-board approach*:

1. *On-board approach*: The untethered miniature mobile robot is self-contained and self-propelled. All functionalities to operate autonomously or with a remote mode are contained on-board.
2. *Off-board approach*: The untethered mobile milli/micro-robotic system is externally actuated, sensed, controlled. Moreover, the robot is powered by external sources.

The two most significant active visual imaging methods for disease diagnosis are endoscopic techniques and laparoscopic techniques. For example, in [1], a capsule milli-robot with an integrated CMOS camera was proposed for actively imaging a 3D type stomach surface. A remote magnetic manipulator actuated this capsule. This system was called a magnetically-actuated soft capsule endoscope (MASCE). After patients swallow this device, it reaches its destination in the stomach within a few seconds. The MASCE can be controlled by the external magnetic field to perform simple movements such as rolling inside the stomach for navigation and position control. Simultaneously, the MASCE can acquire images of the stomach's 3D surface for diagnosis.

For mobile in-situ sensing, Ergeneman et al. conducted a preliminary study of a magnetically controlled untethered magnetic micro-robot that could achieve optical oxygen sensing for intraocular measurements inside the eye [2]. This device enabled measurements at locations that are prohibitively invasive to sense with laparoscopic techniques. The robot integrated an optical luminescence sensor and a magnetic steering system.

Martel et al. designed a system using magnetic resonance imaging (MRI) to propel an untethered micro-robot inside a living swine (in vivo) [3] in 2007. The navigation was guided by the MRI imaging, but the MRI also provided the propulsive magnetic force to move a 1.5 mm diameter ferromagnetic bead in the carotid artery of a living swine.

Targeted therapy (also called targeted drug delivery) is the task of bringing drug particles to the desired location (and only to that location). Targeted drug delivery would enable using more smaller quantities of more powerful drugs because the drugs are not distributed systemically but instead are delivered directly to the target. A fast and reliable technique for targeted drug delivery could revolutionize medicine. Mobile untethered milli-/micro-robots can release therapeutic, biological, and chemical substances at a specific target location with precisely controlled amounts by externally controlled mechanisms. Thus, potential side effects can be minimized because stronger amounts of

the substance could be delivered faster and more efficiently. Moreover, the recovery time cycle of patients can be significantly shortened. Active capsule endoscopes were proposed to deliver drugs in the GI tract using passive or active drug release methods in [4]. Remotely triggered drug release mechanisms were described in [5]. Additionally, remote-controlled drug delivery using untethered robots was shown in [6–8].

For many of these aforementioned potential applications, the micro-robots are driven by an external control mechanism. Most groups have chosen to use an external magnetic field for the external control mechanism. Of magnetic robots, magnetic helical-shaped robots are one of the most well-known and well-researched untethered mobile magnetic milli-/micro-scale design concepts. Many strategies and algorithms have been developed for fabrication, navigation, and control of the helical robots, and these have been developed over a wide span of robot sizes from milli-scale to nano-scale. Surveys and reviews of magnetic helical-shaped robots are presented in [9–11]. The helical robots are designed with a spring-like tail, but the spiral-type helical magnetic robots are a screw-like design. However, spiral-type helical magnetic robots have not been investigated or explored as much as helical-shaped micro- and nano-robots. Because of their corkscrew shape, spiral-type robots are suitable for drilling, grounding, and heating [12]. Moreover, most of the current related works were focused on controlling an untethered robot in 2D environments. These environments range from tubular channels with a few bifurcations to open areas to demonstrate 2D motions. There have been few studies on control or on tracking performance in 3D environments. To investigate magnetic swimmers, researchers have developed many external magnetic field systems. The dominant form of magnetic systems in hospitals is MRI scanners. MRI has the potential to be a reasonable external input platform for magnetic robot manipulation because an MRI can provide a uniform magnetic field and provide precise 2D or 3D imaging feedback. However, to perform MRI-guided intervention or minimally invasive surgery using a miniature magnetic robot as an integrated surgery system is currently not feasible because of the MRI scanner's narrow cylindrical chamber. This narrow cylindrical core inside MRI scanners limits access to patients and therefore limits the size of the robots that could be used. The strong magnetic field in and around the MRI place additional limitations on the materials that can be used in an MRI-compatible robot. Moreover, the

robots must be made so that they do not interfere with the MRI scanner's imaging techniques. MR-compatible robotic manipulators and a teleoperate mechanical maneuver mechanism are needed to address these limitations.

The objectives of this dissertation include the following aspects:

1. Exploring an MR compatible teleoperate mechanism for force transmission.
2. Proposing two MR-compatible manipulators and closed-loop positioning control for the manipulator actuated by the teleoperate transmission mechanism.
3. Demonstrate the lab-built magnetic platform for the control studies.
4. Design and optimize the milli-scale spiral-type swimmer for 3D navigation.
5. Explore the closed-loop control algorithms for 3D navigation on the spiral-type miniature magnetic robot.
6. Investigate in vitro potential medical or biomedical applications.
7. Demonstrate the feasibility of using ultrasound as a feedback sensor and robot arm to carry the ultrasound probe and track swimmer.

1.2 Dissertation Organization

The dissertation is arranged as follows: Chapter 2 presents the proposed teleoperate mechanical maneuver mechanism for force transmission. The analysis of the ideal mathematical model and the experimental results of the solid medium transmission's key components are presented. Three types of mechanisms for an MRI-compatible manipulator are proposed. The positioning control of 1D and 2D manipulators and MR compatibility of the first-generation 1D manipulator are demonstrated. Chapter 3 presents the lab-built magnetic system's mechanism, then investigates the design optimization on a milli-scale spiral-type miniature magnetic robot and the 3D navigation performance comparison of several proposed control methods. Chapter 4 analyses the preliminary study and feasibility of using ultrasound as a feedback sensor and robot arm to carry the ultrasound probe

and track swimmer. Chapter 5 concludes the current results shown in the dissertation and discusses the potential future works.

2 SOLID MEDIUM TRANSMISSION

2.1 Introduction

Magnetic resonance imaging (MRI) is one of the most powerful diagnostic clinical devices to establish in pre-operative planning for interventions and surgeries. Because of the lack of ionizing radiation, excellent soft-tissue contrast, and an internal coordinate system, MRI is also advanced and developed for real-time inner operative guidance. Engineers and scientists have optimized mechanical transmission systems for centuries. Examples of transmission mechanisms include cables, belts, driveshafts, mechanical linkages, and fluidic power transmission systems, as indicated in [13–19]. Many of these mechanisms were a success of engineering optimization for particular applications and tasks. However, every mechanism has both advantages and disadvantages. An advanced inner MRI operative, MR-compatible robotic manipulators plus mechanisms have been proposed for remotely operating interventional tools [20–24]. These techniques are proposed to address limited access to patients through a cylindrical chamber inside MRI scanners. These mechanisms and manipulators must meet the following requirements:

1. It can operate inside a cylinder with a 60-70 cm diameter, including the patient lying on the MRI scanner's couch.
2. It can work in magnetic fields whose magnitude may go up to 3 Tesla and rapidly changing magnetic field gradients from 40 mT/m/ms to 200 mT/m/ms).
3. Safety requirement.
4. It can not induce any imaging artifacts, such as distortion of the field gradients or production of electromagnetic interference (EMI).

Because of the limited space inside the MRI scanners, most MR manipulators are invented by placing the power units or sources outside the gantry, which is away from the scanner's isocenter, and the manipulator of intervention is mounted by/on the patient. In this case, a transmission mechanism is necessary to build the connection between the powering unit and the manipulator. The mechanical drives are proposed in [25–28] and fluidic systems is demonstrated in [29–35]. Mechanical

approaches offered enhanced kinematic performance, and they are successfully employed for both general and anatomy applications. Ultrasonic motors (USM) are generally used because of the high resolution, nonmagnetic characteristic. Other advantages are linear or rotary motor structure and have powerless braking. Fluidic transmissions were also studied as an alternative MR compatible manipulation mechanisms, such as pneumatic transmission system [30–34] and hydraulic transmission system [34, 35]. They can offer a flexible conduit and can be made of nonmagnetic and nonconductive materials. The PneuStep is one of the pioneer pneumatic stepper motor developed for MR compatible manipulators [36]. Although all these works were proposed for MR compatible manipulation, each actuation frame shows advantages and barriers. For example, most mechanical approaches require a rigid structure and secured transmission routing. These limitations may be suitable for the clinical applications of the prostate [29], breast [26], or brain [27]; however, a flexible routing may be necessary for logistics furthermore ergonomics, for example, access to patient crossing the obstructing arrangements in the MRI scanner room.

Because of the motor size and EMI, USM is normally placed at a distance away from the MRI scanner's isocenter. Thus, a structural provision or mechanical linkages is required for the connection [26, 37]. The EMI produced by USM can cause 40%-60% reduction in SNR, which indicated in [25, 28, 29, 38–40]. It may be compensated by interleaving imaging and actuation [38], shielding [28, 40], and filtered drivers [39]. Alternatively, motors or power source should be placed out of the scanner room to avoid EMI [25, 36, 39, 41]. The direct-drive actuators show more reliable kinematic performance in MR manipulation comparison study [41].

This section proposed an alternative mechanism called solid media transmission (SMT), a fluidic actuator. Still, solid media, spheres interleaved with spacers, are filled in its conduits, as shown in Fig. 2. Because it is a motor-based design, most hydraulic/pneumatic systems use ultrasonic motors to achieve high efficiency and performance, which are more complicated and expensive, while SMT using an EM motor. Additionally, SMT can avoid the leakage problem of the traditional fluidic systems. The groundbreaking studies [42] illustrated the feasibility of SMT actuation with an open-loop controller. Dr. Huang introduced force amplifiers and multi-port manifolds for the SMT system [43].

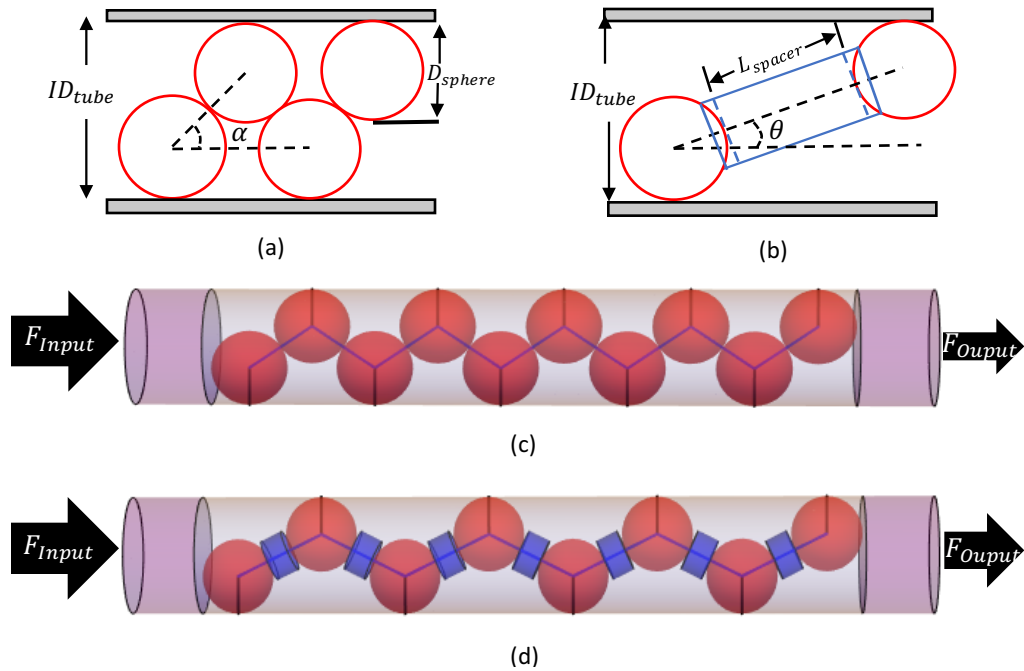


Figure 2: SMT schematics: (a) illustrates the pattern of SMT sphere packing. (b) illustrates the combination of SMT using spacer and sphere. (c) shows the sphere zigzag packing pattern. (d) presents sphere and spacer zigzag packing pattern. The spacers are hollow along central axis and the spheres fit partly inside the spacer.

We previously published three papers within this context [42–44] about the solid media transmission (SMT). The SMT transmission mechanism employs conduits filled with a force-transmitting medium, and the tubes are flexible to be curved to route for transmission requirements. A one-DoF SMT-actuated linear manipulator is mounted on a UR3 robot arm shown in Fig. 3. The robot arm is utilized as fixed support to demonstrate the flexibility of SMT lines as similar to hydraulic hoses. Repetitive elemental units or pairs (spheres or pairs of spheres and spacers) were filled into the SMT transmission line. And the units or pairs form a firm backbone, which is transversely self-adjustable to fit the channels' routing shape. SMT's original motivation was to drive manipulators inside MRI scanners to perform interventions [42, 44, 45]. As a mechanical aspect, these studies proved satisfactory kinematic performance and MR compatibility for such potential applications. The SMT

system can offer high flexibility, scalability to meet the request of manipulators. All above mentioned preliminary works, including the force amplifiers and multi-port manifolds demonstrated in [43], support the idea that the SMT system is a leakage-free, fluid-less yet fluidic-like system, which may serve as an alternative transmission mechanism for other specialties.

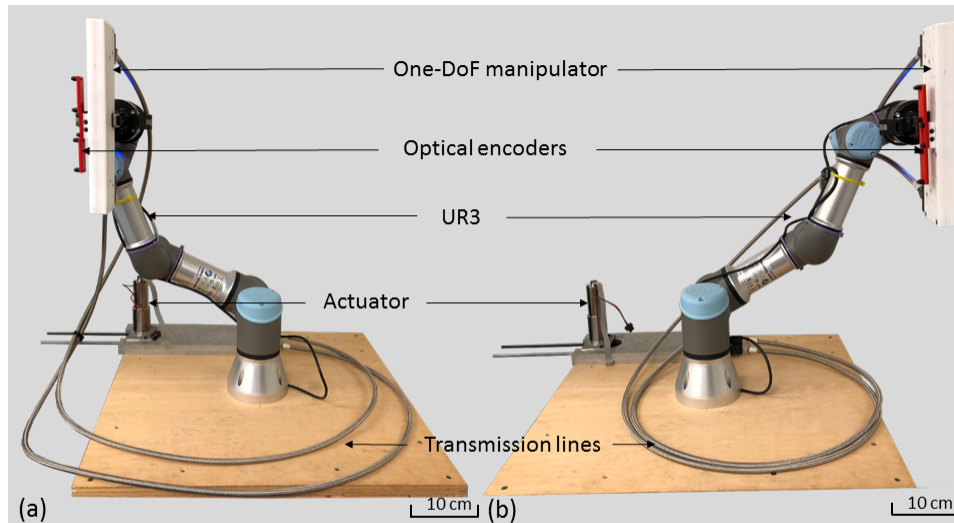


Figure 3: One-DoF manipulator driven by SMT mounted on an UR3 robot arm. The flexible transmission lines can follow the robot arm's movement moving from the left-side to the right-side.

Because SMT is a recently proposed mechanism, the purpose of the first part of this section is to examine the fundamental features of this undiscovered technique. In the following studies, we firstly developed an ideal mathematical model for the SMT mechanism. Then we assessed the common physics properties such as friction, dimensions of componentry, and media packing patterns. Experimental studies were concentrated on the closed-loop control of the SMT. It demonstrated the ability for sub-millimeter accuracy with the challenge of achieving a steady media packing pattern. The MR compatibility experiment studies were performed with a one degree-of-freedom (DoF) SMT-compatible manipulator. We assessed this mechanism's MR compatibility and the possibility of using conventional EM motors inside an MRI scanner room. In the later section, the advanced

studies will be presented. The purpose of the second part is to demonstrate the design concepts of 1D and 2D positioning manipulator and verify the hypothesis proposed in [46]. A one-degree-of-freedom manipulator with different combinations of spheres and conduits was utilized to validate the theory that the materials and dimensions dominate the SMT performance. Experimental studies were mainly performed with a proportional-integral (PI) controller for our 1D manipulator, and a master-slave controller was employed for our 2D SMT-actuated manipulator.

2.2 SMT Backbone

The SMT mechanism is majorly composed of solid discrete media packing inside a transmission conduit. The solid media packing pattern is illustrated in Fig. 2. The spheres are with a diameter of D_{sphere} , spacers are with a length of L_{spacer} , and the inner diameter of conduit is presented as ID_{tube} . When the media is packed inside the conduit, they formed a zigzag pattern, and greatly exaggerated schematics are shown in Fig. 2. There is a small gap between the spheres and tubing walls in the real world, minimized by zigzagging. The packing pattern of SMT media is formed by applying a force that tends to achieve the minimum compression ratio. The compression ratio is defined as the horizontal distance between two spheres divided by the sphere diameter (i.e., the ratio of $(\text{sphere}_i - \text{sphere}_{i-1})_x$ and D_{sphere}). In this way, the solid media are naturally arranged into this zigzag pattern since the sphere diameter D_{sphere} should be less than the inner tubing diameter ID_{tube} to ensure all media can freely move forward and backward inside the conduit. Furthermore, the ratio of ID_{tube} and D_{sphere} must not be as small as possible because it needs to prevent the packing pattern that collapsing on itself and forming multiple points of contact. This allowable ratio is

$$\frac{ID_{\text{tube}}}{D_{\text{sphere}}} \in \left(1, 1 + \frac{\sqrt{3}}{2} \right). \quad (1)$$

The simplest pattern of SMT is to be only filled with spheres, and it can be driven by an extending pushing rod through outside the conduit lumen. For the sphere-only case, when a driven force is applied, the spheres are packed in a zigzag pattern. Fig. 2(a) shows the angle α between the central

axis of the conduit and the center to the center vector of adjacent spheres, which is defined as

$$\alpha = \arcsin \left(\frac{ID_{\text{tube}} - D_{\text{sphere}}}{D_{\text{sphere}}} \right). \quad (2)$$

For the combination of spheres and spacers, the angle θ is defined as the angle between the central axis of the conduit and the center to the center vector of the adjacent spheres shown in Fig. 2(b), which is

$$\theta = \arcsin \left(\frac{ID_{\text{tube}} - D_{\text{sphere}}}{D_{\text{sphere}} + L_{\text{spacer}}} \right). \quad (3)$$

Spacers increase the efficiency of force transmission. Comparing equation (2) with (3) shows that lengthening the spacer reduces the angle between the axis of the channel and the center-to-center line of the sphere, which means spacers reduce the magnitude of forces orthogonal to the pushing direction and increase the force transmitted along the central axis of the tubing.

For a variety of MR compatible actuated devices, the SMT line must be routed from the power source to the isocenter inside the scanner gantry and, thus, assume a curved posture. Packing arrangements are different in straight and bent tubing. When spheres with cylindrical spacers are used and pass through a curve, an additional important geometric feature is considered to avoid a spacer binding or collide with the conduit wall. The bending radius $D_{\text{bend}}/2$ of a given conduit with diameter ID_{tube} and the length L_{spacer} of a spacer determines the maximum diameter D_{spacer} of the spacer, which is the case that there is only one intersection point between the outline of a spacer and the inner wall of tubing. The simplified equation is

$$D_{\text{spacer}} \in \left[0, \cos \left(\arcsin \left(\frac{L_{\text{spacer}} + D_{\text{sphere}}}{D_{\text{bend}} + ID_{\text{tube}} - D_{\text{sphere}}} \right) \right) \cdot (D_{\text{bend}} + ID_{\text{tube}} - D_{\text{sphere}}) - (D_{\text{bend}} - ID_{\text{tube}}) \right]. \quad (4)$$

Inside a bend, the SMT backbone arranges itself to minimize the compression ratio. As illustrated in Fig. 4, in an arc, the spheres are either all are pushed against the outer wall of the tube as Fig. 4(b) or are in a pattern that zigzags parallel to the axis of curvature along the tube centerline as Fig. 4(c). If the spheres are centered in the tube, the angle advanced along the bend from one sphere

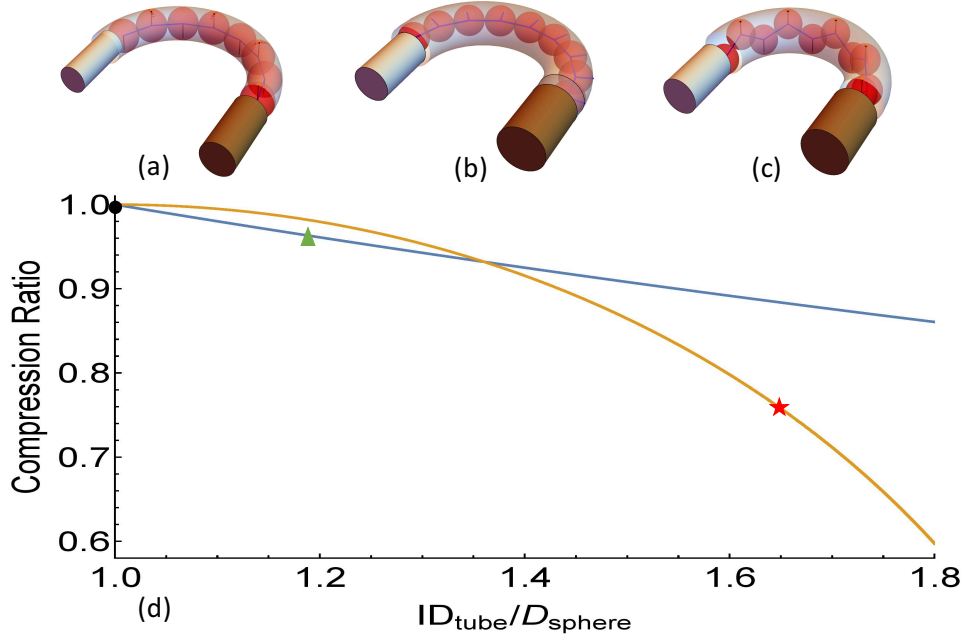


Figure 4: Compression ratios studies for tubing bend diameter $D_{\text{bend}} = 5D_{\text{sphere}}$: (a) Compression ratio for $ID_{\text{tube}} = D_{\text{sphere}}$ shown with a black dot. (b) Compression ratio when spheres and spacers are pushed to outside wall shown with a green triangle. (c) Compression ratio for zigzag packing shown with a red star.

to the next is

$$\beta = \arccos \left(1 - \frac{2D_{\text{sphere}}^2}{D_{\text{bend}}^2} \right). \quad (5)$$

When the spheres are all are pushed against the outer wall of the tubing, the angle advanced along the bend from one sphere to the next is

$$\gamma = \arccos \left(1 - \frac{2D_{\text{sphere}}^2}{(D_{\text{tube}} - D_{\text{sphere}} + D_{\text{bend}})^2} \right) \quad (6)$$

and the compression ratio is

$$\eta_1 = \frac{\gamma}{\beta}. \quad (7)$$

For the zigzag pattern, the angle advanced along the bend from one sphere to the next is

$$\delta = \arccos\left(\frac{D_{\text{bend}}^2 + 2(D_{\text{tube}} - 4)D_{\text{tube}}}{2D_{\text{bend}}^2}\right) \quad (8)$$

and the compression ratio is

$$\eta_2 = \frac{\delta}{\beta}. \quad (9)$$

For low ratios of $\frac{ID_{\text{tube}}}{D_{\text{sphere}}}$ the spheres are pushed to the outside of the bend, and for high ratios the spheres assume a zigzag pattern. The switch occurs when η_1 equals η_2 .

As shown in Fig. 4(a), when the ratio of ID_{tube} and D_{sphere} is one, the compression ratio is one. When the compression ratio is less than the switching point, the packing pattern has the spheres pushed to the outer rim of the tubing, as shown in Fig. 4(b). Beyond the switching point, spheres and spacers form a zigzag pattern, as shown in Fig. 4(c).

2.3 Friction in the SMT Mechanism

Friction is commonly existing in all mechanical systems such as bearings, fluidic system cylinders, and transmissions. Any two surfaces in relative movement with the physical interface can also produce friction. For the SMT system, friction is the dominant reason for system delay and force transmission deficiency. [43] demonstrated that when the mass of a solid media is relatively small compared to physical forces, we can safely neglect the effect of gravity. Moreover, experimental observations confirm that the spheres perform slide without any rolling movement in the SMT mechanism studies (i.e., dimensions and materials). Hence, our model only considers sliding spheres. In the ideal mathematical model, spacers and spheres are tightly connected and not considering deformation. This ideal friction model analyzes the system qualitatively, and we did not consider the effect of the Coefficient of Friction (COF) difference. According to the prior work [13] and considering the complexity of analyzing the entire SMT backbone in one calculation, we decomposed the SMT backbone into an individual combination. Then we modeled the friction of the whole backbone iteratively with a piecewise function. The entire process only considered Coulomb friction.

When $N_{\text{sphere}} = 2$, the center to center Euclidean distance Z of the two adjacent spheres is

$$Z = \sqrt{2D_{\text{sphere}}(L_{\text{spacer}} + ID_{\text{tube}}) + L_{\text{spacer}}^2 - ID_{\text{tube}}^2}. \quad (10)$$

The relationship between input and output force of two spheres is

$$F_{\text{Out}}(2) = F_{\text{In}} \left(1 - 2\mu \frac{ID_{\text{tube}} - D_{\text{sphere}}}{Z} \right), \quad (11)$$

where μ is the conduit friction coefficient. For a given length L_{SMT} of the SMT conduit, the least number of spheres N_{sphere} which is needed to form a packed backbone is calculated by

$$N_{\text{sphere}} = \frac{L_{\text{SMT}}}{Z}. \quad (12)$$

After assigning c equal to the right part of equation (5), now, the output force is

$$F_{\text{Out}}(N_{\text{sphere}}) = c \left(1 - \mu \frac{ID_{\text{tube}} - D_{\text{sphere}}}{Z} \right)^{N_{\text{sphere}} - 2}. \quad (13)$$

The manually preload process allows representing the spacer and sphere as one rigid body. The spacers between spheres can reduce the angle between the channel's axis and the euclidian distance between the center of two adjacent spheres when spheres are the only friction model components. In an SMT system, normal forces only exist between spheres and the tubing against the conduit's inner wall. When the input force applies on the first ball, this force will be spread one by one. For the special case, there is only one sphere in the conduit. The input force is nearly equal to the output force. If there are only two-spheres in the conduit, it will form two contact surfaces, and two normal forces exist. One more contact surface will be added by adding one sphere. The consequence of this phenomenon is reflected in the coefficient of μ . In equation (5), the coefficient is equal to 2. But it is equal to 1 in equation (7). The friction terms are therefore applied in series. And the output force turns out to be the product of similar terms.

The SMT mechanism's certain features are highlighted in the simulation results in Fig. 5. As

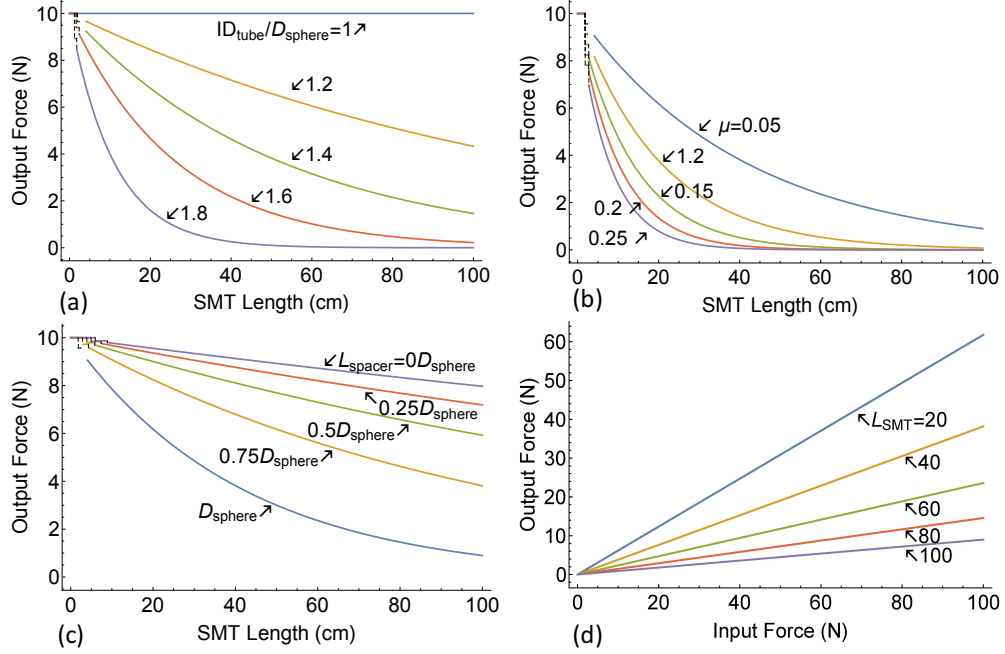


Figure 5: SMT major component studies: (a) length of SMT line. (b) Friction coefficients of materials. (c) Ratio of ID_{tube} and D_{sphere} . (d) length of interval spacer.

shown in Fig. 5(a), the friction of the SMT backbone increases while the length of the tubing increases (i.e. the N_{sphere}). So we can conclude that the tubing should be as short as possible to reduce friction but achieve the goal distance. As marked in Fig. 5(b) to (d), The solutions for improving force transmission efficiency are the following: using low friction componentry material, reducing the ID_{tube} of the transmission conduit, or extending the length of the spacer. The Mathematica simulation code is available at [47].

2.4 Preliminary Experiment Studies

2.4.1 Experimental Set-Up

To further investigate the SMT mechanism's properties, we built a customized experimental platform shown in Fig. 6. A PC-based real-time controller (Advanced Control Education Kit1103,

dSPACE Inc Wixom, MI) was employed. The dSPACE is the system's main controller, which calculated a corresponding pulse-width modulation (PWM), directional signal, and enabling signal based on the velocity and displacement requests. These signals are then sent to an ESCON servo motor (ESCON 50/5, USA subsidiary). The gear reduction ratio is 43:1, and the rack and pinion actuated two opposite-movement rods to actuate two 1-meter long SMT lines bidirectionally. The SMT transmission conduits were then connected to the manipulator with an optical encoder (ENX16 EASY 1024 CPI, USA subsidiary) for recording the displacement; the dSPACE controller sampled the signal of the optical encoder and calculated the displacement. All the control and measurement code was programmed in Simulink. The real-time control code was then automatically generated and downloaded to the PPC750GX and TMS320F240 DSP, located on the DS1103 board, respectively. We also used the control desk (dSPACE GmbH, US subsidiary) to monitor and track experimental data in real-time.

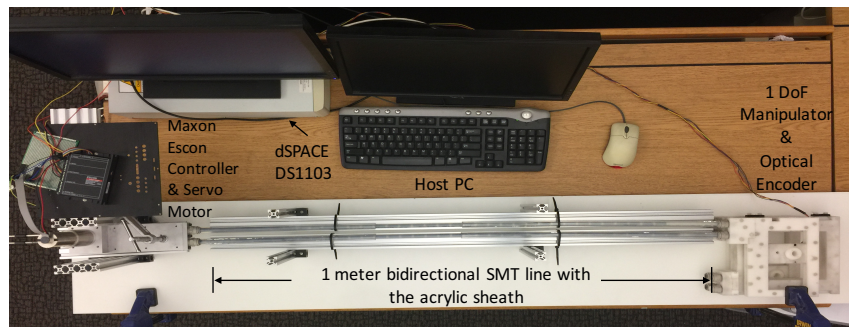
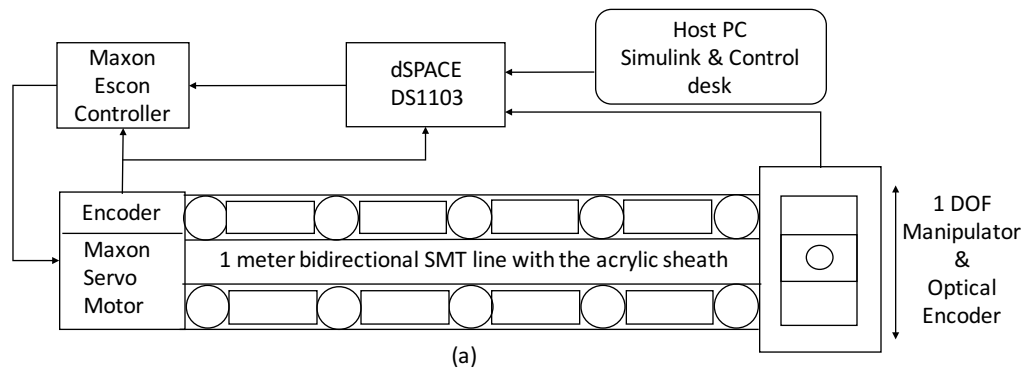


Figure 6: The experimental setups: (a) Block diagram of the system. (b) Photograph of the experimental platform.

For closed-loop control studies, a 1 meter long nylon tubing with an $ID = 7$ mm and an $OD = 9$ mm, which is filled with $D_{\text{sphere}} = 6.23$ mm nylon spheres and nylon spacers with $L_{\text{spacer}} = 20$ mm is used. The experimental data were gained and plotted at 1kHz. We insert the nylon tubing into a UV-extruded acrylic tube with $OD = 15$ mm and $ID = 9.35$ mm. The external UV-extruded acrylic tube was employed as the purpose of ensuring the channel's rigidity and prevent elastic deformation of nylon tubing.

2.4.2 Closed-Loop SMT Control

The SMT setup exhibited displacement errors and response delays due to backlash in the open-loop. When the gaps exist between media, the motor's force loses contact with the load, and it only drives itself, rods, and shaft but not the load. The problem of the backlash has been investigated since the 1940s. The harmful effects of backlash include steady-state increase error and system stability. The issues exist in robotic arms [48] and rolling mills [15]. To minimize the impact of backlash, we examined closed-loop positioning control. As [49] indicated, feedback can be from the side of the motor, load, or motor and the load side. We use feedback from both the motor and manipulator side with optical encoders mounted on them in our design. The Maxon encoder is utilized as feedback from the motor side is for velocity control, and the feedback from the manipulator side is used for positioning control.

Because the backlash can introduce phase lags that can cause oscillations or instabilities in the controlled system. We designed and imitated a modified dual loop PID controller as described in [50], to compensate for backlash. The feedback from the motor and manipulator side contributes to controlling the system transient. The motor displacement(X_m) is sketched to meet the transient requirement. The optical encoder measures the displacement (X_l). Using the angular difference signal

$$X_d = X_m - X_l. \quad (14)$$

The feedback in the steady state is equal to

$$-X_m + \frac{1}{Ts + 1}(X_m - X_l). \quad (15)$$

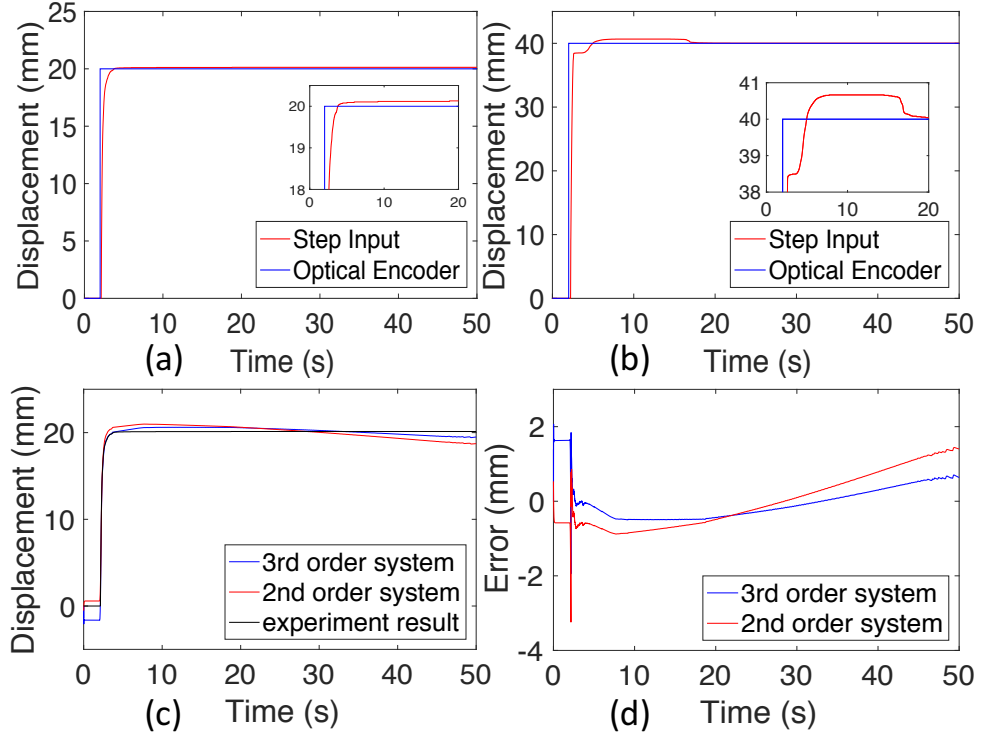


Figure 7: Control studies and system identifications: (a) system output of a 20 mm step input. (b) system output of a 40 mm step input. (c) 3rd order and 2nd order models comparison. (d) The comparison of the estimated system error and experiment results.

If the time constant $T = 0$, the equation will be equal $-X_1$. As T tends to infinity, the result approaches $-X_m$.

According to our prior works [42], we found that there are three key elements of the SMT system: the ratio of ID_{tube} and D_{sphere} , friction coefficient μ , and the elasticity coefficient of the conduit. Because we do not have a finite element analysis (FEA) model of the SMT backbone. To explore the appropriate number of state variables for presenting most system characteristics, we used the MATLAB System Identification toolbox. The system identification toolbox can estimate the continuous and discrete transfer function in the time domain and state-space form. The toolbox mainly uses the algorithm of the State Variable Filter (SVF) and Instrument Variable (IV) shown in [51] and [52]. The 20 mm step signal and 40 mm step signals were compared by giving the step input signal at 2 seconds and keep it for 50 seconds. As the results shown in Fig. 7(a) and (b), the overshoot of 40 mm step signal is much higher than the overshoot of 20 mm step. Conduit's

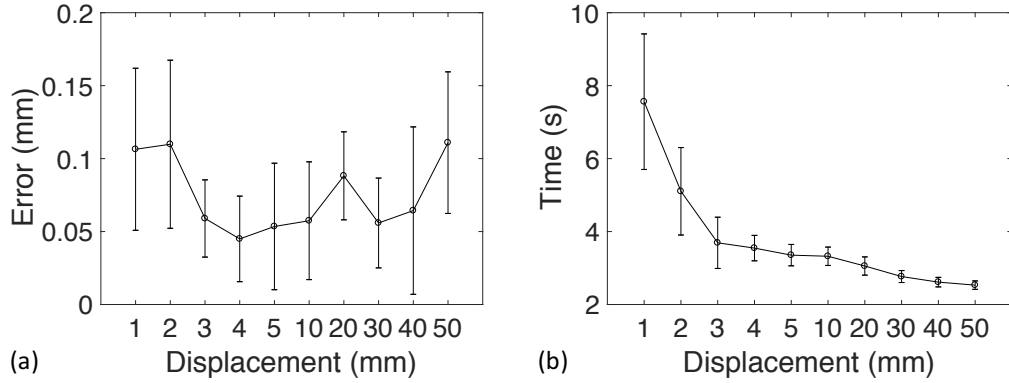


Figure 8: SMT positioning control studies: (a) The mean and standard deviation of displacement error. (b) The mean and standard deviation of system response delay. Each data point contains 10 trials.

elastic deformation may induce the flat pattern of the overshoot. We also used the MATLAB System Identification toolbox to assess the system's number of orders. This study reported that when the system is modeled as a 2nd order system, the fit ratio is about 82.5%. While the fit ratio reaches 92.3% when it is modeled as a 3rd order system. This result confirms that the system may have three dominant states.

The magnitude of step commands is proportional to the PID controller's proportion gain, increasing overshoot at the responding period. Because the DC motor has a maximum acceleration, it can be saturated by the input signal. To decrease the overshoot impact, we shift the step input function to a ramp function. The magnitude of ramp function input in the tests were 1, 2, 3, 4, 5 mm and 10, 20, 30, 40, 50 mm. Each test contains ten trials with random direction. The trial is counted when the steady-state error is within 1%, and the positioning data's resolution is 0.0001 mm. The average displacement error of this system was 0.075 mm with a standard deviation is 0.042 mm (total n=100 measurements) shown in Fig. 8(a). It also demonstrates that the 1-m long nylon SMT can achieve a sub-millimeter positioning control accuracy. We present the error of closed-loop positioning control

to show SMT's feasibility, stability, and effectiveness of the PID controller. Additionally, Fig. 8(b) shows the response delay ranging from 7.56 ± 1.85 s to 2.53 ± 0.11 s, and the average is 3.75 ± 0.53 s. An interesting result was observed from the results: the delay was inversely related to the displacement input magnitude. According to the model studies in the previous section, this phenomenon is mainly induced by friction and elastic deformation. These two resistance forces weaken the input force and reduce the system's sensitivity level. All the results are shown in Fig. 8(b).

2.5 MR Studies

MR studies to evaluate the SMT mechanism's compatibility following NEMA were performed on a 1.5 T scanner at Avanto, Siemens Healthcare. We used the 1-DoF manipulator driven by a 4-m long SMT line (the nylon tubing did not insert in an external acrylic sheath). With the above setup, We placed the servo motor and an electronics box positioned sideways of the MRI scanner in the MRI scanner room, which is orthogonal to the magnet axis. The motor and electronics box was placed outside the 5 Gauss line at 2.5 m away. The electronics box components are regulated power supplies, motor controllers, and filters. They can communicate with the Host PC, placed outside the scanner room via an optical cable through the wall waveguide. According to our prior results [42] and [53], we tried to reduce EMI by the following approach:

1. A custom-made Faraday cage surrounded the electronics box.
2. All the cables and the electronics box were shielded and grounded together to the scanner room ground.
3. A low pass filter was implemented for the input signals.

We have performed three MR studies (transmission and reception, homogenous phantoms, and a TrueFISP pulse sequence) using the MRI scanner's main RF coil. The technical parameters are the following: TR = 3.2 ms; TE = 1.46 ms; Excitation Angle = 85° ; matrix size = 192×192 ; field of view = 192×192 mm²; slice thickness = 10 mm).

For the signal transmission and reception studies, the images were collected following two conditions. First, we defined the baseline of the phantom by placing no hardware. Second, the 1-DoF

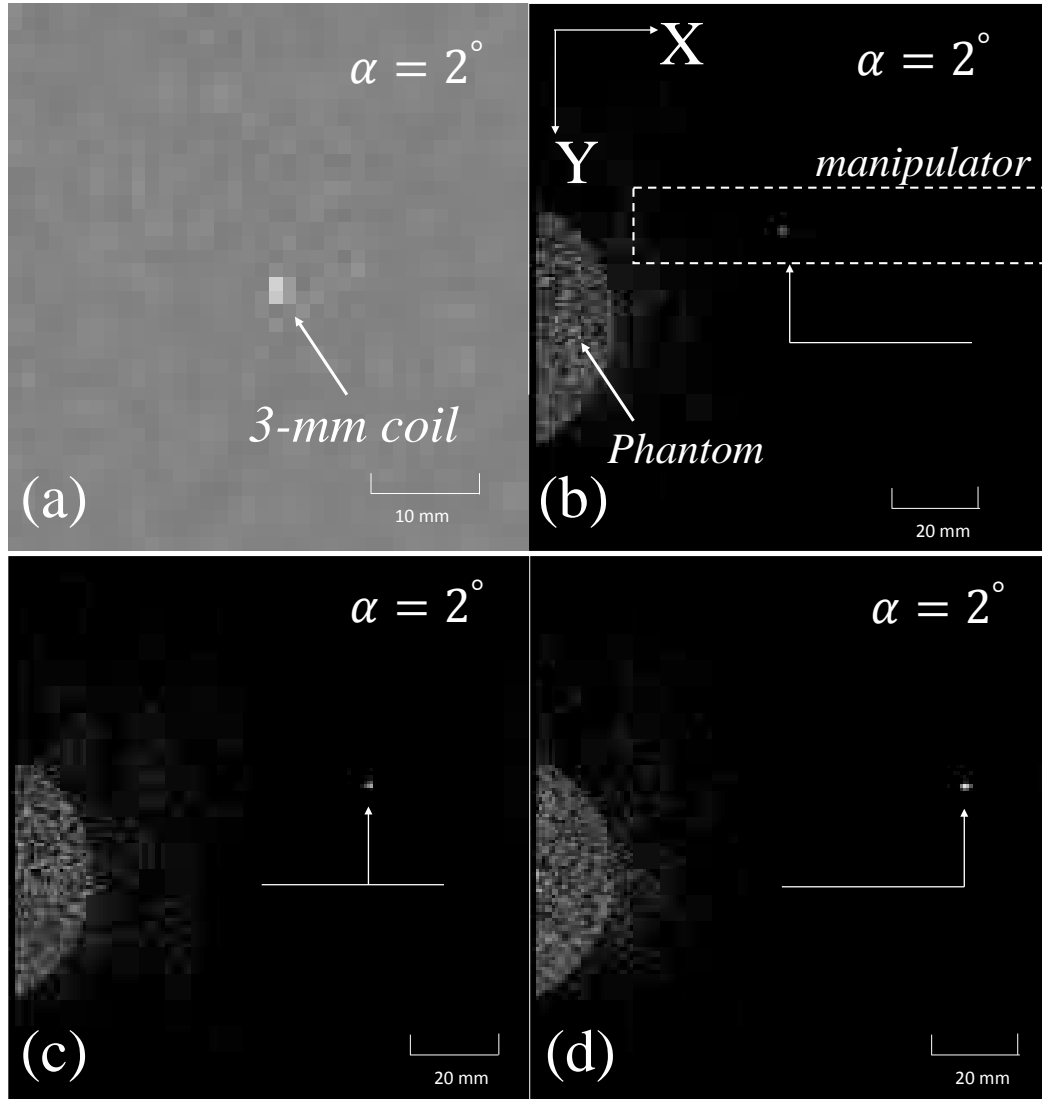


Figure 9: SMT MR compatibility results: (a) shows a snapshot of the MR marker. (b) - (d) show MRI frames of the marker driven by the manipulator.

was secured over the phantom and connected to the SMT transmission line. But there are no electronics or motors placed in the room. Because of the MR inert material, no observable difference exists between the two conditions. In the homogenous phantoms study, there are 20 images collected for each following conditions: (I) The baseline and power off, (II) power on but motor idle, (III) motor on without signal filtered, (IV) motor on with signal filtered. The signal-to-noise ratio (SNR) was analyzed based on the collected images. The SNR is defined as a ratio of the collected running signal and baseline the signal over the phantom region-of-interest (ROI). The SNR results were normalized and reported in the form of the mean \pm std. The SNR of baseline Condition I is 100

$\pm 8\%$, the SNR of Condition II is $99 \pm 9\%$, the SNR of Condition III is $13 \pm 8\%$, and in Condition IV, the SNR is $89 \pm 9\%$. Filtering, shielding, and grounding of the Faraday cage can recover the SNR by 11% of the baseline losses, which is indicated in our previous studies [42] and [53]. The third study evaluated the tracking performance of a 3-mm diameter solenoid inductively-coupled RF coil marker driven by the SMT-actuated manipulator. The MR marker was attached to the 1-DoF manipulator, which was secured onto the patient couch. The manipulator was actuated to move forth and back. And the images were collected among the same TrueFISP, but with a very small excitation angle of 2° . This small excitation angle is needed to operate the inductively coupled coils. Fig. 9(a) shows a snapshot of the marker. The image is zoomed to evaluate the noise level. From the result, we can conclude that the motor did not affect imaging. Fig. 9(b) to (d) show the collected frames during the manipulator movement, which is highlighted by the dashed white box representing the three moments of the MR marker coil. All studies performed above confirmed that the servo motor-driven SMT manipulators could be tracked with coupled coils.

As [54] indicated, the material such as nylon and Delrin are validated as MR safe materials for SMT setup. In our work, the SMT line was driven by ordinary EM motors, which are not MR compatible, and placed in the MR room. Similarly, the works shown in [55] presented an FDA-cleared MRI-radiation therapy system with 180 DC servomotors, a valve phantom shown in [56], and our cardiac phantom in [53]. As we mentioned above, the EMI can be reduced by placing electronics beyond the 5 Gauss line, using a low-pass filter for the signal, and grounded Faraday shielding. As the results show in [42, 53], the filtered SNR is about 89% vs. unfiltered SNR 13%. We use EM motors because they: (i) have high off-the-shelf availability, (ii) are low cost, (iii) are high torque, and (iv) have been well examined in the engineering community. The system is labeled as MRI “conditional”, not “compatible” due to the EM motor and the SNR reduction units. The system must be placed beyond the 5G line around the MRI scanner. Though the items have been demonstrated to pose no known hazards in [54], we still need to perform further studies on whether they can be used in human studies.

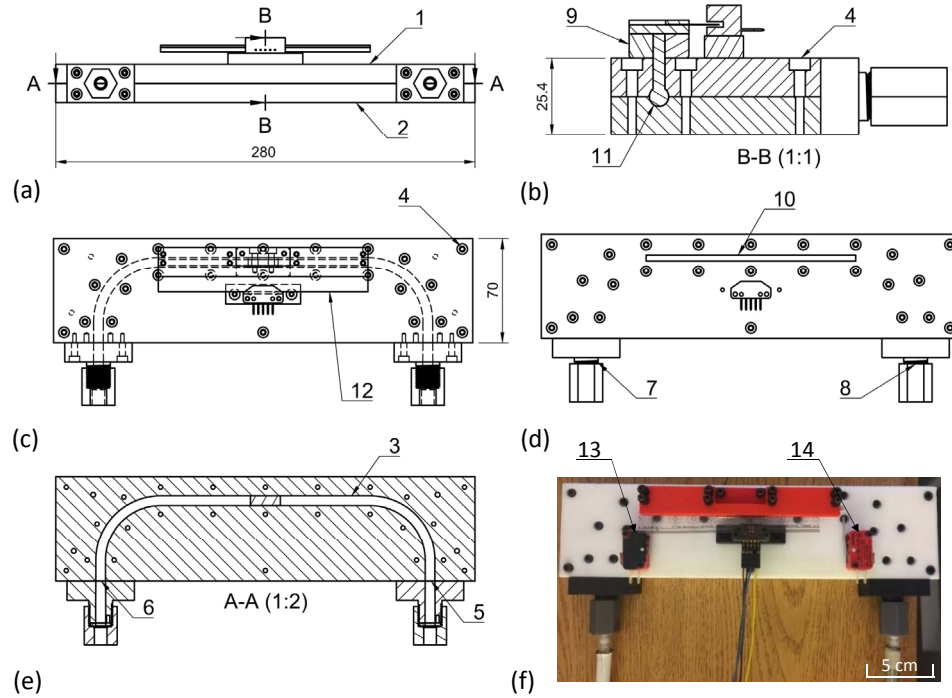


Figure 10: The schematics of end loop actuator: (1) Upper stage. (2) Bottom stage (3) Inner lumen. (4) Screw hole. (5, 6) Channel end edges. (7, 8) are tubing fittings and adapters. (9) Carriage of optical encoder. (10) Slot in upper stage. (11) Piston. (12) Optical encoder strip. (13, 14) are Stop switches.

2.6 Design of SMT-Actuated Manipulators

2.6.1 Linear Manipulator

The CAD schematics and a photograph of our second-generation one-DoF linear manipulator are illustrated in Fig. 10. The one-DoF manipulator is practically devised and optimized in the schematics and manufacturing. The manipulator consists of four CNC-ed components: upper and bottom Delrin stages as (1) and (2) (280 mm × 70 mm), the half SMT lumen as (3), and several screw holes as (4). When the two stages were screwed together, the full lumen was formed with an inner diameter $ID_{\text{channel}} = 6.48$ mm. The customized SMT tubing connectors as (7) and (8) were connected at the end edges (5) and (6). The lumen in the connector transitions from an inner diameter $ID = 6.7$ mm to an inner diameter $ID = 6.48$ mm in the channel, where the spheres of the SMT backbone can move freely without any obstruction. The SMT-actuated carriage (9) has a 20 mm extension beneath itself, and it enters into the inner channel via a slot (10) in the upper

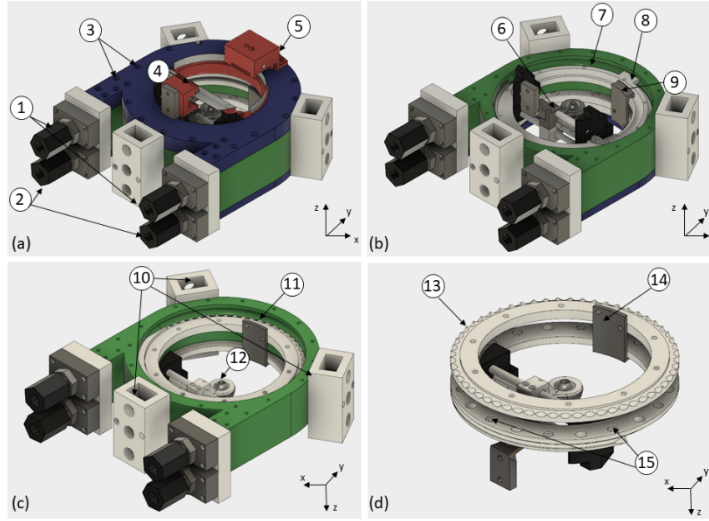


Figure 11: RTS 3D schematics: (1, 2) are the SMT tubing connectors. (3) is the screw holes. (4) is the optical encoder and strip to record translation motion. (5) is the optical encoder and strip to record rotation motion. (6) is the tool carriage. (7) is the inner channel of rotation. (8) is the inner block. (9) is the extended piston. (10) is the Mount slot. (11) is the inner channel of translation. (12) is the ball-and-socket A . (13) is the sprocket. (14) is a bridge connection. And (15) is the ball bearing.

stage (1). The 20 mm long extension (11) worked like a piston and pushed by the SMT media to move bidirectionally. An optical encoder strip (12) (EM1 module, US Digital, Vancouver, WA) was mounted on the carriage (9), and the carriage can move in a range of ± 50 mm. Two switches (13) and (14) were placed on the left and right boundary for safety. The optical encoder's analog signal was fed to the cRIO as the feedback information for the closed-loop control.

2.6.2 Rotation-Translation-Stage (RTS)

The first generation of 2D SMT-driven robot, Rotation-Translation-Stage (RTS), is illustrated in Fig. 11, and it shows the 3D schematics and the photographs of the prototype. The RTS manipulator has two actuated degree of freedom: (i) a rotating ring as DoF-1 (The rotation angle α is in the range ± 90 deg), and (ii) a prismatic translation carriage as DoF-2 (The translational range r is in the range ± 20 mm). The inner channels (7) and (11) are with an inner diameter $ID_{\text{channel}} = 6.48$ mm, and several screw holes as (3) were CNC-ed. Each DoF channel end was connected to the customized tubing connectors (1) and (2). The lumen transitions happened in the connector are from $ID = 6.7$ mm in the tubing to $ID = 6.48$ mm. This design concept is the same as the end loop manipulator

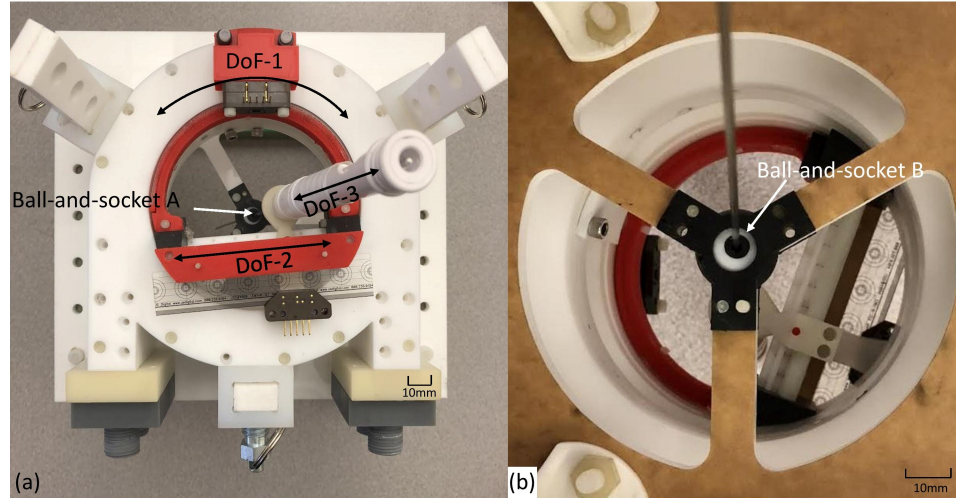


Figure 12: Top and bottom views of Physical prototype model.

to ensure the media can move freely in the channel. For the rotation DoF-1, the SMT transmission line pushes the block (8) inside the channel and changes the rotation angle controlled by the closed-loop controller. The rotational displacement is recorded by optical strip and encoder (5) (EM1 module, US Digital, Vancouver, WA). The translation movement is under the effect of rotational input DoF-1 because there is a bridge (14) with an extended piston (9), which connects the upper stage actuated by DoF-2 with the spheres actuated by DoF-1. DoF-2 moves the extended piston (9) and pushes the carriage (6) drive the tool mounted through the ball-and-socket A (12). The linear displacement of DoF-2 was recorded by the optical strip and encoder (4) mounted on the carriage. To improve the translation force's efficiency through the bridge, we utilize a sprocket design (13) rather than a smooth channel for the DOF-1 (7). Additionally, ball bearings were incorporated between layers (15) to reduce the channel walls' resistance while rotating. The RTS can be attached by three slots (10) or spring-loaded latches. With the mechanical structure of RTS, the ball-and-socket (12) can be placed inside a circle with a radius of ± 20 mm. And the distal end of the tool is permanently anchored onto the frame of the RTS robot. If a needle is placed between A and B as shown in Fig. 12, the tip of the needle can be pointed at any location $(x_{tip}, y_{tip}, z_{tip})$ of the spherical cone workspace.

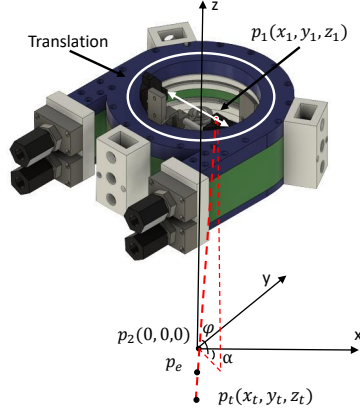


Figure 13: The RTS 3D schematics model and the coordinate frames for kinematic studies.

2.6.3 RTS Manipulator Kinematics

The RTS robot does not possess a serial kinematic chain's properties, so we used linear algebra calculation rather than homogeneous transformation matrices to simplify the forward kinematics calculation. This study focused on two stages RTS robots with two fixed ball-and-sockets rather than one stages RTS. The subscripts are used to denote which stage is referenced. Given the translation displacement T_1 and rotation angle α_1 , the coordinate of the central ball-and-socket on the first layer stage can be computed as $P_1 = [x_1, y_1, z_1]^T$. And given the translation displacement T_2 and rotation angle α_2 , the coordinate of the central ball-and-socket on the second layer stage is computed as $P_2 = [x_2, y_2, z_2]$. Because of the separation s between the two stages, the needle was assumed to have a minimum insertion depth d_{\min} , and the range of insertion is d_{insert} , and maximum insertion depth is $d_{\text{insert}} \in [0, d_{\max}]$. The needle entrance point P_e is

$$\vec{P}_e = \vec{P}_1 + d_{\min} \frac{\vec{P}_1 - \vec{P}_2}{\|\vec{P}_1 - \vec{P}_2\|_2}, \quad (16)$$

and the target point P_t is:

$$\vec{P}_t = \vec{P}_1 + (d_{\min} + d_{\text{insert}}) \frac{\vec{P}_1 - \vec{P}_2}{\|\vec{P}_1 - \vec{P}_2\|_2}. \quad (17)$$

Because of the RTS robot's design concept, it is abstracted as a torus for rotation and a rod across the center of the torus for translation, as shown in Fig. 13. Only a single stage RTS was utilized in the experiment, which means the coordinates of P_2 are $[0, 0, 0]^\top$, so the kinematics analysis is only based on the one stages RTS unite. Two pairs of SMT conduits drive the one-stage RTS, so the system inputs of two-DoF are two linear displacement inputs. The rotational angle α_1 could be converted from displacement input as

$$\alpha_1 = \frac{R}{2\pi r} 2\pi = \frac{R}{r}, \quad (18)$$

where R is the rotational input, r is rotational radius. The elevation angle φ is

$$\varphi = \arctan\left(\frac{T_1}{s}\right), \quad (19)$$

where T is translation input. The $P_1 (x_1, y_1, z_1)$ is

$$x_1 = T_1 \cos \alpha_1 \quad (20)$$

$$\text{and } y_1 = T_1 \sin \alpha_1, \quad (21)$$

where s is the separation distance between two stages, and it is equal to z_1 . If the target point is considered concluding needle insertion length d_{insert} , the P_t is

$$x_t = x_1 - (d_{\min} + d_{\text{insert}}) \cos \varphi \sin \alpha_1, \quad (22)$$

$$y_t = y_1 - (d_{\min} + d_{\text{insert}}) \cos \varphi \sin \alpha_1, \quad (23)$$

$$\text{and } z_t = z_1 - (d_{\min} + d_{\text{insert}}) \cos \varphi \sin \alpha_1. \quad (24)$$

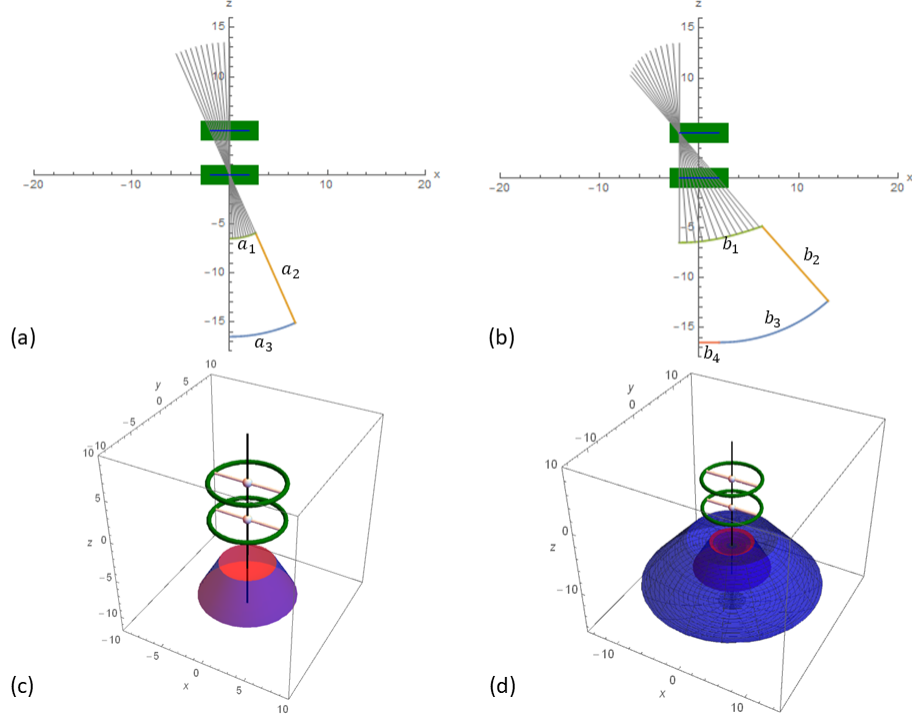


Figure 14: The workspace of two stacked RTS robots. (a) and (b) are the sector of bounded by 4 arcs. (c) and (d) is this workspace rotated about the z -axis.

Given a target position coordinate P_t , needle entrance point P_e , and needle insert length d_{insert} , the ball-and-socket coordinates of two layers are calculated by substituting the givens to (16) and (17). So, the solutions can be computed as the following equations

$$x = T \cos \alpha, \quad (25)$$

$$y = T \sin \alpha, \quad (26)$$

$$\text{and } \alpha = \arctan\left(\frac{y}{x}\right). \quad (27)$$

To satisfy the movement range of DoF-1 and symmetric design, these calculations must satisfy the following constraints

$$\begin{cases} T = -|T| & x < 0 \\ T = |T| & 0 \leq x. \end{cases} \quad (28)$$

2.7 Two-DoF Manipulator Configuration Space

This section investigates the robot configuration space based on the previous kinematics calculations to better understand the RTS robot's characteristics. The workspace of the RTS is a spherical cone because of the symmetric design. A cross-section defines the workspace in the xz plane, and the completed workspace is gained by revolving arcs about the z -axis is shown as Fig. 14 (a) and (b). In Fig. 14, the RTS is presented as a dark green rectangle, as in Fig. 11. For the first case shown as Fig. 14 (a) and (c), there is only one stage RTS. Thus, The cross-section of this configuration space only consists of three arcs. The parameter $t \in [0, 1]$. The equation of the top arc $(x, z) = a_1(t)$ is

$$x = d_{\min} \sin \left(\arctan \left(\frac{rt}{s} \right) \right) \quad (29)$$

$$\text{and } z = -d_{\min} \cos \left(\arctan \left(\frac{rt}{s} \right) \right). \quad (30)$$

The equation of the side slant $(x, z) = a_2(t)$ is given by

$$x = (d_{\min} + td_{\max}) \sin \left(\arctan \left(\frac{rt}{s} \right) \right) \quad (31)$$

$$\text{and } z = -(d_{\min} + td_{\max}) \cos \left(\arctan \left(\frac{rt}{s} \right) \right). \quad (32)$$

The equation of the bottom arc $(x, z) = a_3(t)$ is

$$x = (d_{\min} + d_{\max}) \sin \left(\arctan \left(\frac{rt}{s} \right) \right) \quad (33)$$

$$\text{and } z = -(d_{\min} + d_{\max}) \cos \left(\arctan \left(\frac{rt}{s} \right) \right). \quad (34)$$

The second case is shown in Fig. 14(b) and (d), which has two stacked RTS robots. The cross-section of configuration space consists of four arcs. The equation of the top arc $(x, z) = b_1(t)$ is

$$x = 2r \left(t - \frac{1}{2} \right) + d_{\min} \sin \left(\arctan \left(\frac{2rt}{s} \right) \right) \quad (35)$$

$$\text{and } z = -d_{\min} \cos \left(\arctan \left(\frac{2rt}{s} \right) \right). \quad (36)$$

The equation of the side slant $(x, z) = b_2(t)$ is given by

$$x = r + (d_{\min} + td_{\max}) \sin \left(\arctan \left(\frac{2rt}{s} \right) \right) \quad (37)$$

$$\text{and } z = -(d_{\min} + td_{\max}) \cos \left(\arctan \left(\frac{2rt}{s} \right) \right). \quad (38)$$

The equation of the bottom arc $(x, z) = b_3(t)$ is

$$x = 2r \left(t - \frac{1}{2} \right) + (d_{\min} + d_{\max}) \sin \left(\arctan \left(\frac{2rt}{s} \right) \right) \quad (39)$$

$$\text{and } z = -(d_{\min} + d_{\max}) \cos \left(\arctan \left(\frac{rt}{s} \right) \right), \quad (40)$$

and the equation of the flat bottom arc $(x, z) = b_4(t)$ is

$$x = rt \quad (41)$$

$$\text{and } z = -d_{\min} - d_{\max}. \quad (42)$$

After revolving these arcs about the z -axis, the final configuration space was plotted in Fig. 14 (c) and (d). Although this paper is focusing on the discussion of a single RTS, two stacked RTS robots can extend a four times larger workspace.

2.8 Experiment Studies on Manipulators

2.8.1 Experimental Set-Up

All the experiments run until the steady-state error is within 0.05 mm to the goals. The customized one-DoF positioning manipulator is shown in Fig. 10(f). The two-DoF positioning manipulator RST is presented as Fig. 15(a). A parallel pair of SMT lines bidirectionally actuated both manipulators. Each SMT pair was powered by a servo motor, as shown in Fig. 15(c), and driven by a control unit as shown in Fig. 15(d). National Instrument Compact RIO (cRIO) (NI Inc. Austin,

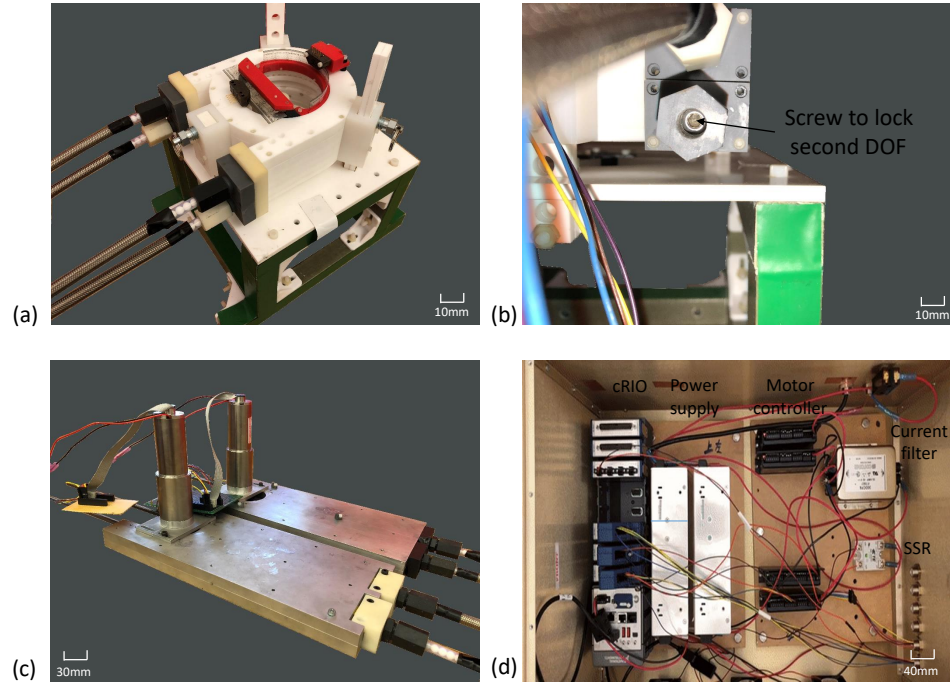


Figure 15: Experimental setups: (a) Isometric view of RST (b) One-DoF isolation study (c) Motor & motor base (d) Electronics box.

USA) was served as a PC-based real-time controller. The control and measurement conversion code was first programmed in LabVIEW, then downloaded to cRIO to drive motor and data acquisition. To make all components compact, we customized an electronics box. The electronics box is powered by a 120 V AC source. A solid-state relay, fuse, switch, and an emergency button was added for safety purposes. The Maxon servo motor (Maxon DCX35L GB KL 24 V, USA subsidiary) powers a dual rack and pinion with a 43 : 1 reduction ratio. And it can convert the rotational motion to linear motion by actuating two rods to provide a bidirectional actuation. The RTS signal flow diagram is shown in Fig. 16(b). The one-DoF manipulator system is similar to RTS, but only one transmission line pair. The positioning control studies on the RTS used two parallel pairs of braided PTFE tubing with an $ID = 6.7$ mm and $OD = 8.3$ mm (AFLEXHOSE, USA, LLC), which has a stainless-steel jacket and PTFE inner tubing. Because the two-DoF of RTS robot are dependent, we conducted closed-loop studies into three cases: First, one of two layers of RTS was blocked by screws, as shown in Fig. 15(b), and the accuracy of each degree-of-freedom was evaluated separately. Second,

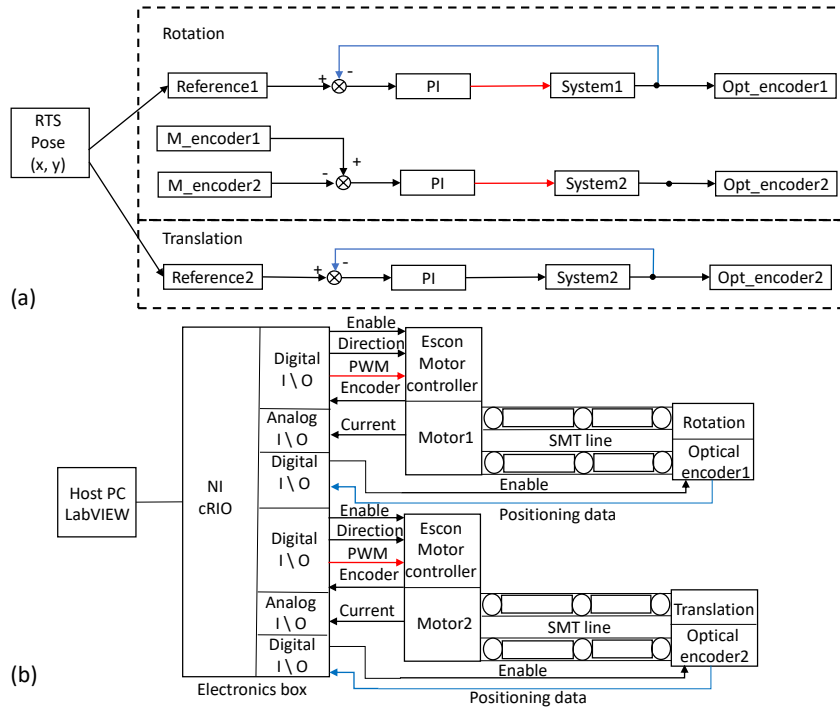


Figure 16: System diagram of Two-DoF: (a) Control diagram (b) Signal flow.

both DoF were connected with one pair of the transmission line, and only the corresponding motor powered on for testing. Third, both motors were powered on for rotation and translation. All the above tests were implemented with PI controllers, and the controller's gains are tuned with the trial and error approach. The PI closed-loop diagram is similar to the translation diagram shown in Fig. 16(a), and the gains remain the same in all rest of the experiments. However, because the two-DoF of RTS are dependent, to compensate and improve the system synchronization performance, we implemented a master-slave controller (MS-control) [57]. The output of the DoF-1 served as the reference for the slave DoF-2. The master-slave closed-loop diagram of rotation is shown as Fig. 16(a).

2.8.2 One-DoF Linear Manipulator Experiment Results

In our previous works [42, 46], we found that the friction between the tubing and solid media, tubing elastic deformation, and conduit length is three key elements of the SMT characteristic study. To improve system performance, we first analyzed the performance of materials with different friction coefficients. Because of the weight and shattering concerns of media, we only experimented

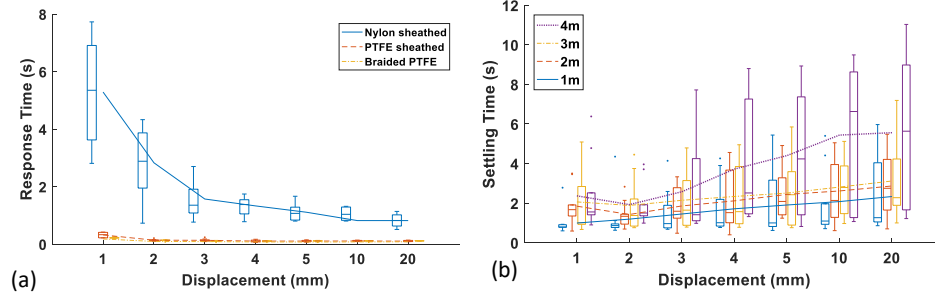


Figure 17: Experimental results of One-DoF: (a) Response time (b) Settling time. Each box-and-whisker marker concludes 10 trials.

with nylon (2 – 4 GPa) and PTFE (0.5 GPa). And they are the most common commercially available materials on the market. The friction coefficient of nylon to nylon is approximately equal to 0.2, and the friction coefficient of PTFE to PTFE is approximately equal to 0.04. We used 1 m long nylon and PTFE tubing with an inner diameter $ID = 7$ mm and an $OD = 9$ mm. Both the nylon tubing and the PTFE tubing were inserted into a UV-acrylic sheath ($ID = 9.35$ mm, $OD = 15$ mm) to ensure the rigidity of the channel and prevent elastic deformation of tubing when the motor applies instant force and while solid media is moving. Moreover, the acrylic sheathes were zip-tied to an aluminum rail to ensure and straighten the transmission line. Although the acrylic sheathes limited the elastic deformation, there still was a 0.35 mm gap between the outer wall of tubing and the inner wall of the sheath. The 1 m braided PTFE tubing with an $ID = 6.7$ mm and $OD = 8.3$ mm (AFLEXHOSE, USA, LLC) was also used for testing. To evaluate the effect of conduit length, we used up to 4 m long braided PTFE tubing in experiments.

For friction coefficients studies, we input step functions as reference signal with the magnitudes of 1, 2, 3, 4, 5, 10, and 20 mm. Figure 17 shows experimental results and plotted in each box-and-whisker; each marker represents ten randomized direction trials. As Fig. 17(a) shows, the average response time of nylon tubing and nylon spheres combination inserted into an acrylic sheath is about 1.97 s. The PTFE spheres and tubing combination reduced the average response time to 0.15 s. To further limit tubing expansion, we used a PTFE stainless-steel braided tubing and PTFE spheres pair. This pair shortens the average response time to 0.1 s, which indicates lower friction and

better-constrained conduit lead to better results. Next, we investigated the impact of transmission conduit lengths from 1 m to 4 m. Fig. 17(b) shows that the settling time increases as the length increases from 1.76 s for 1 m to 4.12 s for 4 m. Although the position accuracy for all length and material experiments always reached the optical encoder's resolution, which was 0.05 mm. With the combination of the latest generation of manipulator design and PTFE braided conduit, our new system can achieve a two times faster response time and ten times faster settling time than our previous system in [46].

2.8.3 Two-DoF Manipulator Experiment Results

For the RTS positioning control studies, we separately investigated three cases *isolate*, *separate*, and *MS-control*, as mentioned above. We input step functions as reference signal with the magnitudes of 1, 2, 3, 4, 5, and 10 mm. Each set was repeated ten times with a randomized direction. Fig. 18(a) shows the settling time results of rotation (DoF-1) . There are two optical recorders with 0.05 mm resolution that was used to record displacement. The settling time of the *isolate* case is higher than the others, and it shows an uptrend from 1.5 s to 2.2 s. Because translation and rotation DoF of RTS are dependent, when the screw blocked it, the solid media in the RTS and conduits were highly compressed, which caused a high resistance. While the magnitude of input reference increased, the settling time increased. The settling time of the second case is from 1.7 s to 1.4 s. These results confirm the hypothesis in our previous work [42, 46], that the resistance forces can weaken the input force and decrease the level of system sensitivity. So the settling time becomes high if the system input is small. With two pairs of transmission conduits connected, the settling time of the *separate* case is shorter than the *isolate* case with the same compression problem. The master-slave control method compensated for the two motor synchronization problems and reduced the solid media compression issue. The settling time is in the range from 0.8 s to 1.6 s, which achieved a better performance than the *separate* or *isolate* cases.

The settling time of translation is shown as Fig. 18(c). Because of the compression issue, the measured settling time of *isolate* case is not predictable, which is in the range from 0.8 s to 1.9 s. For the *separate* and *MS-control* cases, both were controlled by the PI controller, so they had a

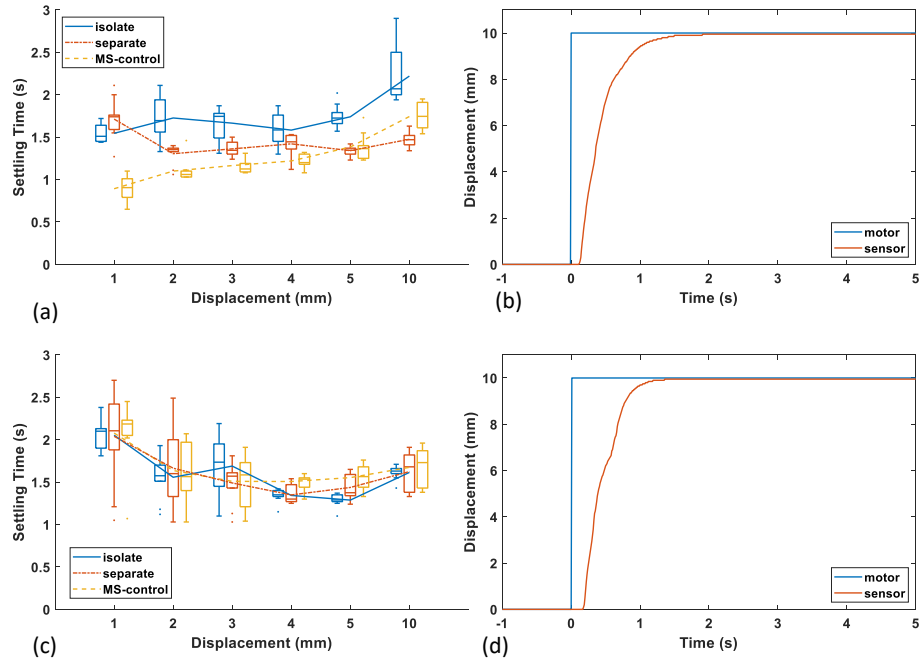


Figure 18: Experimental results of RST: (a) The settling time of rotation. (b) MS-control results of rotation. (c) The settling time of translation. (d) MS-control results of translation.

similar pattern. The settling time is from 1.5 s to 2.5 s. This slight difference is because when DoF-1 changes, the solid media's inner packing pattern also changed unpredictably and influenced the system performance. Figure 18(c) and (d) show the bidirectional step input response result of the system. For all trials, the system accuracy resolved the optical encoder (0.05 mm).

3 MILLI-SCALE MAGNETIC SWIMMER

3.1 Introduction

Magnetic milli-, micro- and nano-robots could be embedded in many biomedical diagnosis and therapy applications ranging from in vitro to in vivo [10, 58–60]. Magnetic robots show great potential for revolutionizing many aspects of medicine because the human body is transparent to low-frequency magnetic fields. When the magnetic field variation ratio is in a safe range, low-frequency magnetic fields are harmless to the human body and other living organisms.

Many magnetic robots are bio-inspired, usually by microorganisms. *Escherichia coli* (*E. coli*) bacteria can swim in low-Reynolds number (Re) liquids using their rotating helical-shaped flagella as molecular motors [61]. This phenomenon was first described by the biologist Berg in 1973. In 1976, Purcell [62] explained that helical swimming is one of the three dominant swimming methods for microorganisms in low Reynolds number (Re) environments. Inspired by this natural behavior, in 1996, Dr. Honda and his group [63] proposed the first magnetic, helical-shaped, centimeter-sized swimmer. The swimmer was teleoperated by an external rotating magnetic field and swam in a low Re environment. After that, these types of magnetically-driven robots have been investigated by many scientists and engineers. For further details, representative surveys and literature review include [9–11]. 2D studies of helical robots such as mechanical design analysis, gravity compensation, and motion control are reported in [11, 59, 64–67]. 3D path-following studies have been proposed in [68, 69].

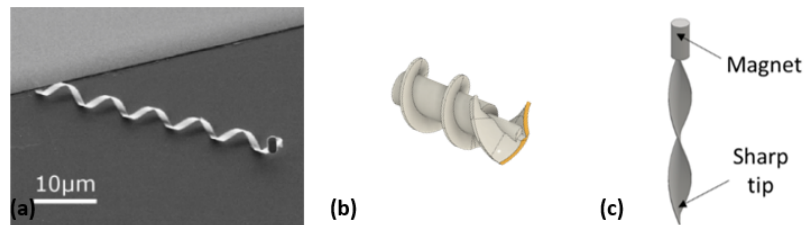


Figure 19: (a) Helix shape. (b) Spiral shape. (c) Twist shape.

There are several design shapes for helical swimmers and a variety of actuation methods. These variations are described in the survey [9]. The three most common shapes for helical magnetic robots are helix, spiral, and twist shown in Fig. 19. The most popular external magnetic sources as a

control input are Helmholtz coils [70] and rotating permanent magnets as in [65, 71]. An interesting alternative was called the DeltaMag, an electromagnetic manipulation system with parallel mobile coils [72]. A mobile set of 3 DeltaMag like EM coils was used to move helical swimmers (and oscillating swimmers) in 2D with camera vision feedback [73].

This chapter focuses on spiral-type (also known as screw-type) swimmers. Spiral-type swimmers have many parameters suitable for exploration. This is probably due to the fabrication challenges of building tiny objects. Spiral-type robots are composed of three main components: a magnet, cylindrical body, and spiral-shaped fins. The magnet can be inserted into a chamber in the cylindrical body. Alternatively, to improve the thrust efficiency, the magnets can be the main body of the swimmer. The magnet magnetization vector should be orthogonal to the central axis of the main cylindrical body. A torque produced by an external magnetic field can be applied to rotate the swimmer and produce a thrust to drive swimmers to swim in a fluidic environment such as [74]. Because of the corkscrew shape design, the spiral-type swimmer also can drill into solid matters. In [74, 75], researchers demonstrated that spiral-shaped magnetic robots could drill through a piece of bovine meat. This groundbreaking (tissue-breaking) result shows great potential for biomedical and clinical applications such as tissue fenestration and blood clot removal. Ishiyama et al. demonstrated that spiral-type swimmers could also provide multiple optional functions that are useful for medical applications [12]. Zhou proposed another clinical application to use this kind of robot as an endoscopic capsule [76]. All works mentioned above focus on the applications and control in 2D environments and a tubular channel with a few bifurcations. In contrast, this chapter investigates and applies control theories in 3D environments.

This chapter first mathematically analyzes how to control the magnetic field using our lab-built magnetic system in Section 3.2. Then we will discuss the current problem within this system, and a method was proposed to compensate for this undesired behavior for the control performance in Section 3.2.4. Next, we present experimental optimization studies of our first spiral-typed magnetic swimmer design and 3D navigation with PI controller studies in Section 3.3 and Section 3.4. Additionally, a Model Reference Adaptive Control (MRAC) was implemented for 3D path-following and compared to a conventional proportional-integrator (PI) controller in Section 3.5. Finally, we

apply this for blood clot removal, a potential biomedical application in Section 3.6. For blood clot removal, we performed optimization studies of tooltip design. We also conducted a study of blood clot removal rates and 3D navigation. All the presented work in this chapter was published in [77–80].

3.2 Magnetic Field Control

This section presents a lab-built magnetic manipulator for 3D navigation and an efficient way to reduce the effect of an undesired gradient force.

3.2.1 Magnetic Manipulator

The lab-built magnetic manipulator system was designed and optimized for controlling miniature swimmers in a 3D environment [77,81]. Figure 20 shows a picture of our magnetic system. The system can generate a magnetic field to apply a torque and/or a gradient force on magnetic objects. In Section 3.2.3, the amount of flux density, force, and torque can be calculated according to the needs of 3D control using the inverse magnetic. A side length of 150 mm fluid-filled, cube-shaped workspace is designed and placed in the center of the manipulator for 3D navigation studies. Three pairs of electromagnetic coils were placed along the xyz -axes to generate an external magnetic field. Each pair of the electromagnet coils are placed on opposite sides along the same axis, and a distance of 300 mm separates them. This manipulator does not provide a uniform magnetic field. The electromagnets can be cooled using liquid nitrogen to increase the magnitude of the magnetic fields [81]. However, this feature was not implemented in these studies.

Twelve power supplies power the whole magnetic system in the current-mode. Each power supply can internally perform a current regulation. For the current system’s circuit connection, the current controlling is better than the voltage controlling because the magnitude of the magnetic field is proportional to the magnitude of the input current. Each coil pairs are connected to two series-connected Kepco BOP 20 – 50 (20 A, 50 V) power supplies. For each coil, the whole power system can provide a total of 20 A and 100 V, which is 12 kW power in total. All power supplies are controlled by the six analog outputs produced by National Instruments (NI) Ethercat input/output

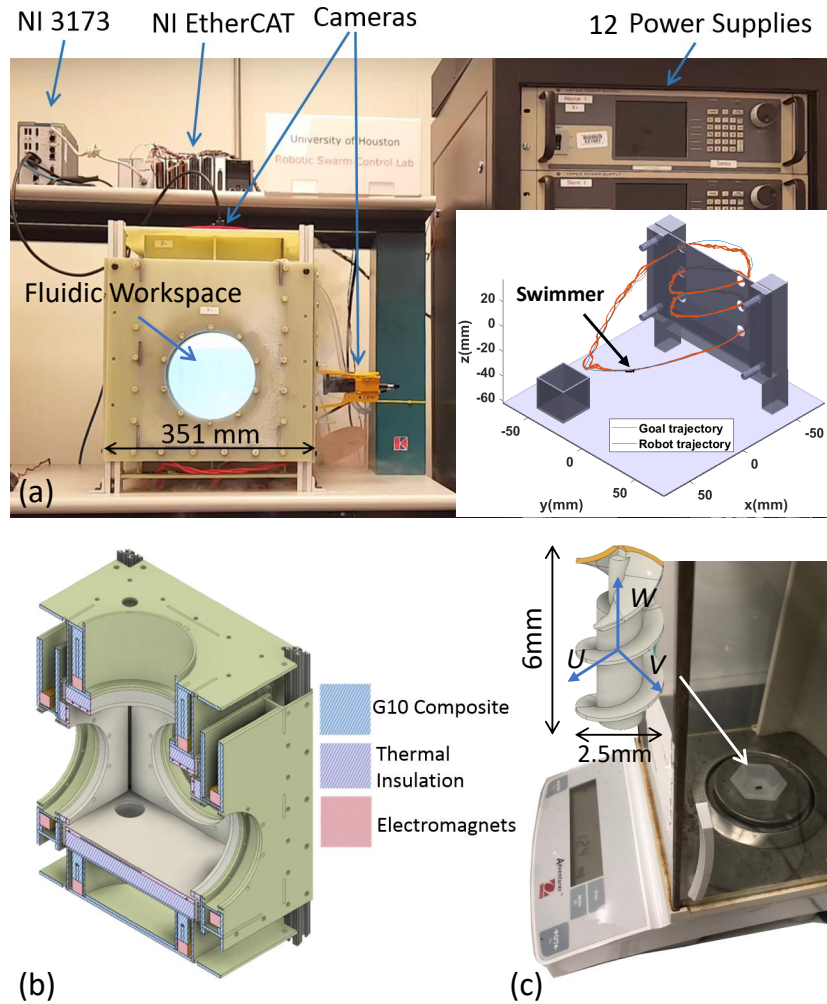


Figure 20: Lab-built magnetic system and schematics of magnetic swimmer. (a) The magnetic manipulator platform. (b) The cross section schematic. (c) The magnetic swimmer.

interface. One thermocouples were glued to each electromagnet coil to monitor overheating. The NI industrial controller IC 3173 is used as the system processor for the swimmer and current control. Two Basler aCA2040 cameras are placed on the top and right sides of the workspace, which forms an orthogonal view of the workspace to measure the 3D position of the magnetic swimmers in realtime(350-400 frames per second). The positioning information gained by two cameras is also used as the feedback for the 3D navigation closed-loop control.

3.2.2 Magnetic Field

A local body Cartesian coordinate system (u, v, w) of the swimmers linked to the magnetic field is defined. The magnetic field has a constant magnitude. The flux density expressed in the (u, v, w) coordinate system \mathbf{B}_{uvw} can therefore be calculated by

$$\mathbf{B}_{uvw} = \begin{bmatrix} B_u \\ B_v \\ B_w \end{bmatrix} = B_0 \cdot \begin{bmatrix} \cos(\theta(t)) \\ \sin(\theta(t)) \\ 0 \end{bmatrix}, \quad (43)$$

where θ is the magnetization orientation of the magnetic field.

When the robot is rotating at sufficient speed, its rotational axis naturally orients itself with w . This effectively allows control of the robot's orientation. The reference frame u, v, w is rotated at an angle α_x around the x -axis and at an angle α_y around the y -axis. The corresponding rotation matrix is

$$\begin{aligned} \mathbf{R}(\alpha_x, \alpha_y) &= \mathbf{R}_x(\alpha_x) \cdot \mathbf{R}_y(\alpha_y) \\ &= \begin{bmatrix} 1 & 0 & 0 \\ 0 & \cos(\alpha_x) & -\sin(\alpha_x) \\ 0 & \sin(\alpha_x) & \cos(\alpha_x) \end{bmatrix} \cdot \begin{bmatrix} \cos(\alpha_y) & 0 & \sin(\alpha_y) \\ 0 & 1 & 0 \\ -\sin(\alpha_y) & 0 & \cos(\alpha_y) \end{bmatrix}. \end{aligned} \quad (44)$$

The magnetic field expressed in the x, y, z reference frame is

$$\mathbf{B}_{xyz} = \mathbf{R}(\alpha_x, \alpha_y) \cdot \mathbf{B}_{uvw}. \quad (45)$$

3.2.3 Inverse Magnetics Calculation

To making the magnetization of the magnet along the swimmer's radial axis, a cylindrical Nd-FeB magnet was inserted into the chamber inside the swimmer. The swimmer rotates itself to align the self-magnetization axis with the external magnetic field when a rotating external magnetic field is applied. Because of this rotation motion, the spiral-type fins can produce a thrust that propels the

swimmer to swim forward.

A right-handed coordinate system is used to define the global inertial frame of the magnetic field XYZ , and the origin of this frame is located at the center of the manipulator workspace. To simplify the calculations of forward kinematics and inverse magnetics as shown in Fig. 20(c), a local body frame of the swimmer UVW is defined; the origin of this local body frame is at the center of the swimmer, and the W -axis is perpendicular to the radial direction of the swimmer.

Because the purpose of this study is mainly focusing on the in vitro studies, and the implementations of helical robots in 3D environments using ultrasound or X-ray imaging as feedback sensors may provide low-resolution state feedback. Therefore, only the swimmer's 3D position gained by Basler cameras is considered feedback states, and the magnetization orientation swimmer is not measured. The swimmer can follow the magnetic input and track the predefined path from the Experimental observations when the magnetic rotation frequency is not equal to or above the swimmer's step-out frequency. Moreover, in this paper, we assume that the swimmer rotation axis can align with the W axis, and the lag between magnetic orientation and the applied magnetic field is small. While the two axes of the swimmer and magnetic field have small misalignments and the lag angle is unknown, the swimmer's orientation is not necessary for the swimmer controlling, which is an advantage of this solution.

The current that applies to each electromagnet (EM) to produce the desired flux density is computed using inverse magnetics equations. The total flux density at a specific position is the sum of the six electromagnetic coils' flux densities. The current vector \mathbf{I} of six EM coils is

$$\mathbf{I} = \begin{bmatrix} I_1 & I_2 & I_3 & I_4 & I_5 & I_6 \end{bmatrix}^\top. \quad (46)$$

The flux density is

$$\mathbf{B}_{xyz}(\mathbf{P}) = \begin{bmatrix} \tilde{\mathbf{B}}_x(\mathbf{P}) \\ \tilde{\mathbf{B}}_y(\mathbf{P}) \\ \tilde{\mathbf{B}}_z(\mathbf{P}) \end{bmatrix} \cdot \mathbf{I} = \mathbf{A}_B(\mathbf{P}) \cdot \mathbf{I}, \quad (47)$$

where $\mathbf{B}_{xyz}(\mathbf{P})$ is the total flux density at the position \mathbf{P} .

$$\tilde{\mathbf{B}}_x(\mathbf{P}) = \begin{bmatrix} \tilde{B}_{1x}(\mathbf{P}) & \tilde{B}_{2x}(\mathbf{P}) & \tilde{B}_{3x}(\mathbf{P}) & \tilde{B}_{4x}(\mathbf{P}) & \tilde{B}_{5x}(\mathbf{P}) & \tilde{B}_{6x}(\mathbf{P}) \end{bmatrix}, \quad (48)$$

$$\tilde{\mathbf{B}}_y(\mathbf{P}) = \begin{bmatrix} \tilde{B}_{1y}(\mathbf{P}) & \tilde{B}_{2y}(\mathbf{P}) & \tilde{B}_{3y}(\mathbf{P}) & \tilde{B}_{4y}(\mathbf{P}) & \tilde{B}_{5y}(\mathbf{P}) & \tilde{B}_{6y}(\mathbf{P}) \end{bmatrix}, \quad (49)$$

$$\text{and } \tilde{\mathbf{B}}_z(\mathbf{P}) = \begin{bmatrix} \tilde{B}_{1z}(\mathbf{P}) & \tilde{B}_{2z}(\mathbf{P}) & \tilde{B}_{3z}(\mathbf{P}) & \tilde{B}_{4z}(\mathbf{P}) & \tilde{B}_{5z}(\mathbf{P}) & \tilde{B}_{6z}(\mathbf{P}) \end{bmatrix}, \quad (50)$$

where $\tilde{B}_{ia}(\mathbf{P})$ is the flux density per unit of current (T/A) produced by the electromagnet i along the a -axis (e.g. a is x , y , or z). The coefficients of $\tilde{B}_{ia}(\mathbf{P})$ are derived from the Biot-Savart law in [82].

The gradient force $\mathbf{F}_{xyz}(\mathbf{P})$ is calculated with

$$\mathbf{F}_{xyz}(\mathbf{P}) = \begin{bmatrix} F_x(\mathbf{P}) \\ F_y(\mathbf{P}) \\ F_z(\mathbf{P}) \end{bmatrix} = \nabla(\mathbf{m} \cdot \mathbf{B}_{xyz}(\mathbf{P})), \quad (51)$$

where $F_a(\mathbf{P})$ is the generated gradient force at position \mathbf{P} along a -axis, and \mathbf{m} is the swimmer's magnetization vector. m_a is the magnetization along a -axis. thus, the equation (51) can be rewritten as

$$\mathbf{F}_{xyz}(\mathbf{P}) = \begin{bmatrix} m_x \frac{\partial \tilde{\mathbf{B}}_x(\mathbf{P})}{\partial x} + m_y \frac{\partial \tilde{\mathbf{B}}_y(\mathbf{P})}{\partial x} + m_z \frac{\partial \tilde{\mathbf{B}}_z(\mathbf{P})}{\partial x} \\ m_x \frac{\partial \tilde{\mathbf{B}}_x(\mathbf{P})}{\partial y} + m_y \frac{\partial \tilde{\mathbf{B}}_y(\mathbf{P})}{\partial y} + m_z \frac{\partial \tilde{\mathbf{B}}_z(\mathbf{P})}{\partial y} \\ m_x \frac{\partial \tilde{\mathbf{B}}_x(\mathbf{P})}{\partial z} + m_y \frac{\partial \tilde{\mathbf{B}}_y(\mathbf{P})}{\partial z} + m_z \frac{\partial \tilde{\mathbf{B}}_z(\mathbf{P})}{\partial z} \end{bmatrix} \cdot \mathbf{I},$$

$$\mathbf{F}_{xyz}(\mathbf{P}) = \mathbf{A}_F(\mathbf{P}) \cdot \mathbf{I}. \quad (52)$$

Equation (47) can be inverted to calculate the needed current to produce the desired amount of the flux density applied to the swimmer. The matrix $\mathbf{A}_B(\mathbf{P}) \in \mathbb{R}^{3 \times 6}$ in (47) is defined as the actuation matrix of flux density. The matrix $\mathbf{A}_F(\mathbf{P}) \in \mathbb{R}^{3 \times 6}$ in (52) is defined as the actuation matrix of the gradient force. According to the above calculations, the magnetic system is underdetermined, and has an infinite number of solutions. Both actuation matrices have linearly independent rows. Thus, the right Moore-Penrose pseudoinverse is performed.

$$\mathbf{A}^+ = \mathbf{A}^* (\mathbf{A} \cdot \mathbf{A}^*)^{-1}, \quad (53)$$

where \mathbf{A} presents the actuation matrix. \mathbf{A}^+ and \mathbf{A}^* are the inverse and conjugate transpose of the actuation matrix. The needed current can be calculated by inversed $\mathbf{A}_B(\mathbf{P})$ of (47) in the form of (53).

By using $P_L = R \cdot \|\mathbf{I}\|^2$ (R is the electric resistance of the EMs, $\|\mathbf{I}\|$ is the Euclidean norm of the current vector), the power P_L lost in the system via Joule heating can be computed, which is proportional to $\|\mathbf{I}\|^2$. The solution computed with Moore-Penrose pseudo inverse minimizes the Euclidean norm of the current vector. The Moore-Penrose pseudo inverse returns the solution that minimizes the Euclidean norm of the current vector and therefore minimizes the power lost via Joule heating [83], which slows down EM coils overheated.

3.2.4 Gradient Force Compensation

As mentioned in one of our publications [77], we only control the flux density using the least-squares solution of (47). This solution returns a non-zero gradient in most cases, and the gradient force can be neglected. In [81], the concatenated actuation matrix (54) is chose to reduce the effect of the undesired gradient force

$$\mathbf{A}_{BF}(\mathbf{P}) = \begin{bmatrix} \tilde{\mathbf{B}}_x(\mathbf{P}) \\ \tilde{\mathbf{B}}_y(\mathbf{P}) \\ \tilde{\mathbf{B}}_z(\mathbf{P}) \\ m_x \frac{\partial \tilde{\mathbf{B}}_x(\mathbf{P})}{\partial x} + m_y \frac{\partial \tilde{\mathbf{B}}_y(\mathbf{P})}{\partial x} + m_z \frac{\partial \tilde{\mathbf{B}}_z(\mathbf{P})}{\partial x} \\ m_x \frac{\partial \tilde{\mathbf{B}}_x(\mathbf{P})}{\partial y} + m_y \frac{\partial \tilde{\mathbf{B}}_y(\mathbf{P})}{\partial y} + m_z \frac{\partial \tilde{\mathbf{B}}_z(\mathbf{P})}{\partial y} \\ m_x \frac{\partial \tilde{\mathbf{B}}_x(\mathbf{P})}{\partial z} + m_y \frac{\partial \tilde{\mathbf{B}}_y(\mathbf{P})}{\partial z} + m_z \frac{\partial \tilde{\mathbf{B}}_z(\mathbf{P})}{\partial z} \end{bmatrix}, \quad (54)$$

where m_a is the magnetization vector along a -axis. The flux density and force can be calculated by

$$\begin{bmatrix} \mathbf{B}_{xyz}(\mathbf{P}) \\ \mathbf{F}_{xyz}(\mathbf{P}) \end{bmatrix} = \mathbf{A}_{BF}(\mathbf{P}) \cdot \mathbf{I}. \quad (55)$$

One access to minimize the undesired gradient force produced by the desired current is to set the gradient forces term on the left of (55) equal to zero. Because the actuation matrix $\mathbf{A}_{BF}(\mathbf{P})$

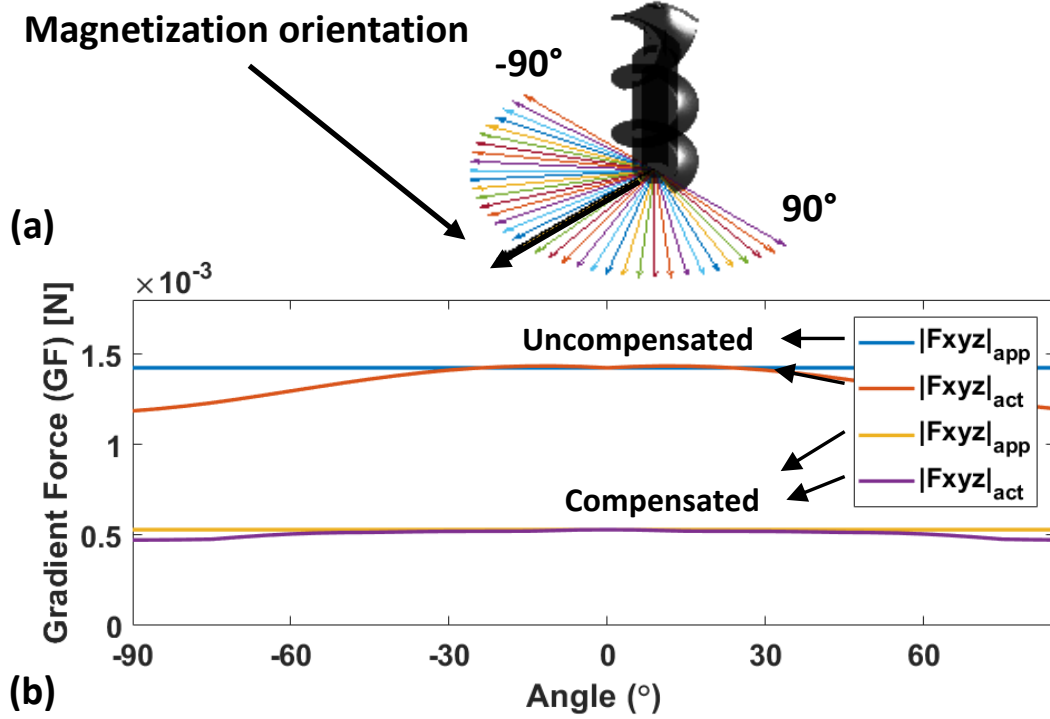


Figure 21: The Numerical study results of the relationship of the angle between actual and approximated magnetization of swimmer in the simulated workspace. The “app” stands “approximated” and “act” stands “actual.”

is ill-conditioned, it can saturate the current input for the power supplies and cause \mathbf{I} to oscillate rapidly, furthermore trigger the safety mode of the power supplies. Tikhonov regularization was implemented to compensate for this problem. If there are zero eigenvalues, the matrix is impossible to invert. While eigenvalues approach zero, the matrix tends toward rank-deficiency, and inversion becomes less stable, described in [84]. One advantage of the Tikhonov regularization is that it suppresses small eigenvalues’ influence in computing the inverse, filtering out the undesired components. The pseudoinverse (53) in the form of Tikhonov regularization can be rewritten as

$$\mathbf{A}_{\mathbf{BF}}^+(\mathbf{P}) = \mathbf{A}_{\mathbf{BF}}^*(\mathbf{P}) (\mathbf{A}_{\mathbf{BF}}(\mathbf{P}) \cdot \mathbf{A}_{\mathbf{BF}}^*(\mathbf{P}) + \Gamma \cdot \Gamma^*)^{-1},$$

where $\Gamma = \alpha \mathbb{I}$, α is the scalar of the regularization, and \mathbb{I} is a identity matrix. For our case, $\mathbb{I} \in \mathbb{R}^{6 \times 6}$ and $\alpha = 10^{-7}$ was selected by trial and error approach, to guarantee the $\mathbf{A}_{\mathbf{BF}} \cdot \mathbf{A}_{\mathbf{BF}}^*$ and $\Gamma \Gamma^*$ have the same order of magnitude. The magnitude of α is much smaller comparing others because the computations are in meters (10³ millimeter) and tesla (10³ millitesla).

The swimmer's magnetization vector was approximated as a vector perpendicular to the heading of the control signal. We have performed a numerical study on gradient force to analyze the effect of falsing approximating the swimmer magnetization orientation. The vector of the desired flux density and swimmer magnetization were set to match the black arrow in Fig. 21 (a) to simplify the numerical analysis in a 3D workspace. We only consider the cases when the magnetic field's rotational frequency is below the step-out frequency, which means the angle difference between the swimmer's magnetization and the external magnetic field is less than 90° and the angle range is $[-90^\circ, 90^\circ]$. The coil currents were computed once using the approximated magnetization vector, while $\mathbf{A}_F(\mathbf{P})$ was calculated over the full $[-90^\circ, 90^\circ]$ range. This study simulated a 2 mT magnetic field and computed a total of 12.5×10^4 different locations in a 0.15 m cube 3D workspace. As the results are shown in Fig. 21 (b), the uncompensated gradient force magnitude difference between approximated and actual is about 8%, and the compensated gradient force magnitude difference between approximated and actual is approximately 5%.

We implemented the PI controller from our previous work [77, 81] to experimentally demonstrate the proposed method. The approximated gradient force $\mathbf{F}_{xyz}(\mathbf{P})$ was computed along the 3D path-following trajectory. The circle trajectories in the experiments have three radii magnitudes (0.02 m, 0.04 m, and 0.06 m) and five z -axis magnitudes (0 m, ± 0.02 m, and ± 0.04 m). We conducted 10 trials for each of these 15 cases, and assumed the magnetization orientation of the swimmer is aligned with the external magnetic field. In Fig. 22, the uncompensated force is plotted with five z -axis magnitudes and three radii (upper layer of each subplot). The magnitude of the compensated force is presented in the lower layer of each subplot. We can conclude that the uncompensated force is symmetric about the z -axis from the results. The mass of the swimmer is 12.4 mg as shown in Fig 20 (c), and the weight is 1.22×10^{-4} N, so the magnitude of the uncompensated force is from 1.2 to 2.6 times the gravity force on the swimmer. Moreover, it increases when the circle trajectories' radii increase because larger circle trajectories are closer to the EM. With the implementation of Tikhonov regularization, the virtual gradient force applied on the swimmer along the path-following trajectories varies from 0.5 to 0.9 times the gravitational force on the swimmer.

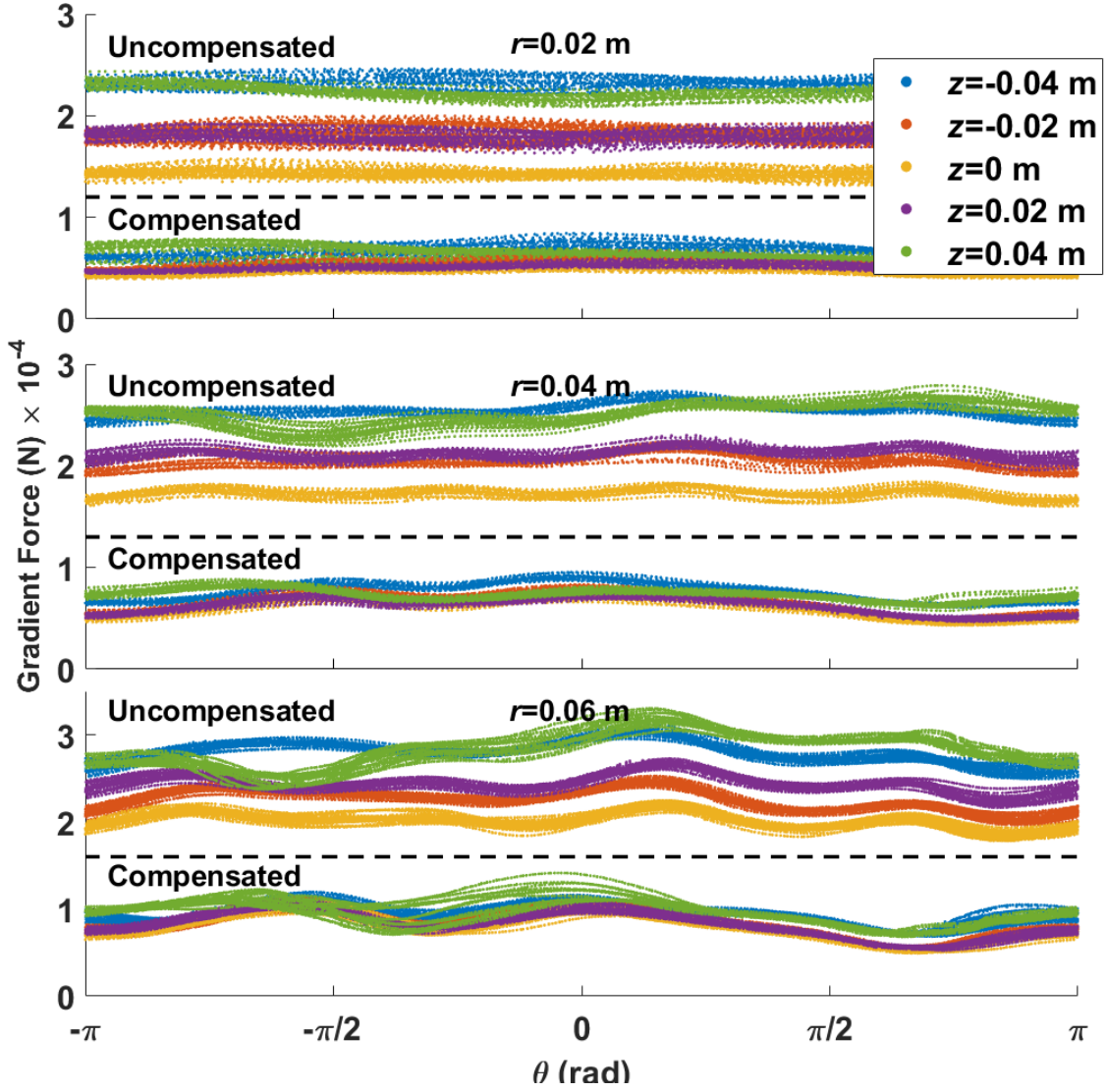


Figure 22: Experimental results of the Gradient force along circular paths.

In practice, perhaps due to poor estimations of the dipole orientation, this compensation had a modest impact on reducing the average tracking error by 28% of the uncompensated case for $z = 0.04$ m and reducing the error's standard deviation by 41%. While this compensation was computationally efficient to implement, the path following performance was only modestly improved, so the rest of the experiments in this dissertation do not use gradient compensation.

3.3 Preliminary Study on Pure Spiral-type Swimmer

An aforementioned magnetic manipulator and related work, in this section, we discuss the preliminary studies on the design optimization on a pure spiral-type swimmer and 3D navigation with a

closed-loop PI controller. The experimental study results on the design optimization and controller comparison are presented.

3.3.1 Closed-loop PI Controller

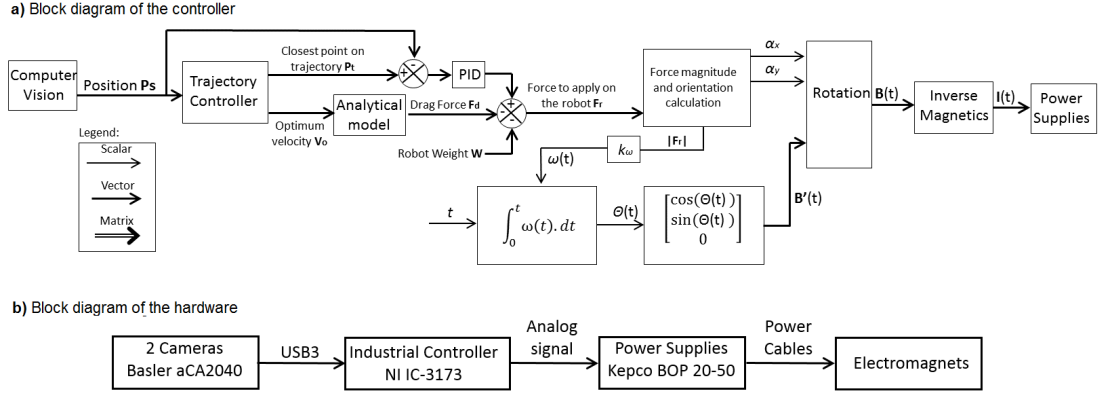


Figure 23: Sytem control and signal flow diagrams.

Force produced by the rotation motion drives the swimmer. The magnitude of the force vector is controlled by changing the rotational speed of the swimmer. The orientation of the force vector determines the direction of the swimmer. The algorithm first must compute the force vector to be applied to the swimmer. The force vector contains three components: the gravity compensation, the drag compensation (the drag along the trajectory centerline), and keeping the robot following the trajectory centerline.

The algorithm first acquires the robot's position by two cameras set on the right side and top (see Fig. 20). The closest point on the desired trajectory, \mathbf{P} , is found via a greedy search. The difference between \mathbf{P} and the robot position is used as the control reference. The outputs corresponding to the force component need to keep the robot following the trajectory centerline.

The optimum velocity vector \mathbf{V} at point \mathbf{P} must then be calculated. Its direction is tangent to the trajectory centerline, and its magnitude is defined in the matrix \mathbf{T} for the feed-forward loop. A simplified fluidic mechanic model presented as

$$\mathbf{F}_d = -C_d \cdot \rho \cdot \mathbf{V} \cdot S \quad (56)$$

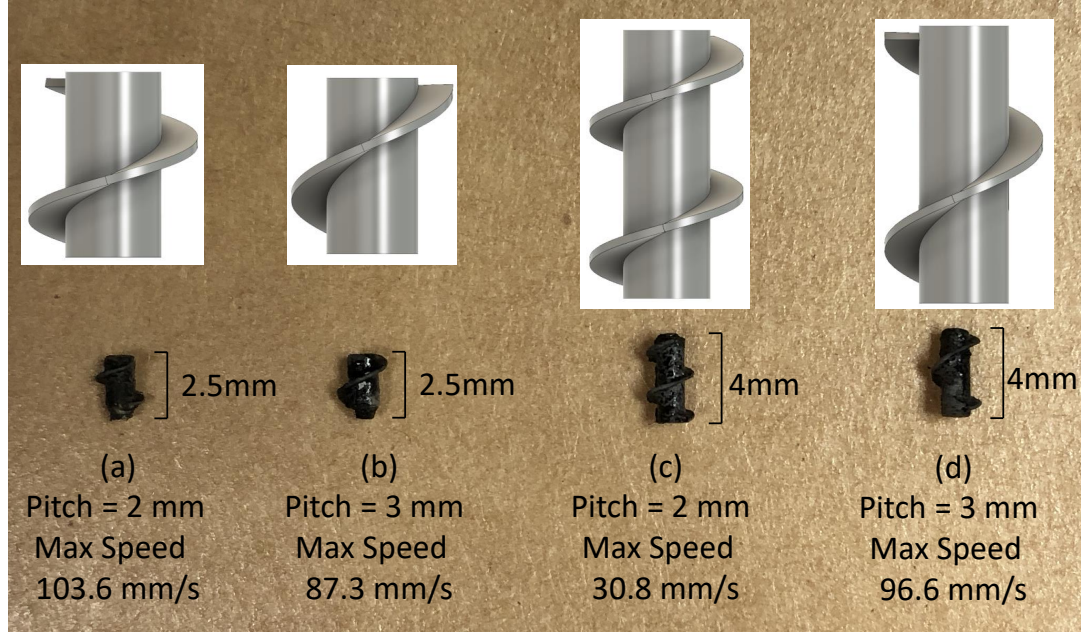


Figure 24: Different robot designs experimentally tested.

is used to compute the drag force \mathbf{F}_d , corresponding to the velocity vector. In this equation, where C_d is the drag coefficient, ρ is the density of the fluid, \mathbf{V} is the velocity vector, and S is the cross-section area.

In this study, the propulsion force \mathbf{F}_r produced by a rotating robot was assumed to be aligned with its rotational axis. The orientation of the swimmer is therefore set to the force vector \mathbf{F}_r . The rotational speed ω is calculated from the magnitude of the force as

$$\omega = \frac{|\mathbf{F}_r|}{k_t}, \quad (57)$$

where k_t is the thrust coefficient. In this study, the drag coefficient C_d , mass of the robot m , thrust coefficient k_t were all approximated and fine tuned by trail and error approach. And the control diagram is shown as Fig. 23.

3.3.2 Swimmer Design and Fabrication

The milli-scale swimmers with a spiral shape shown as Fig. 24) have a diameter of 2.5 mm. They were manufactured by a Projet 3510 HD high-resolution 3D printer. Four different designs

were built and tested (see Fig. 24).

A hole is designed in the center of the swimmer to receive a cylindrical permanent magnet. The magnets were the same for all tested robots. They are all N50 NdFeB, have a diameter of 0.75 mm, and a length of 1 mm. The radially magnetized characteristic allows it to produce a torque along the revolution axis of the swimmer.

3.3.3 Experimental Optimization on Swimmer Design

All different robot designs mentioned in the previous subsection were tested experimentally.

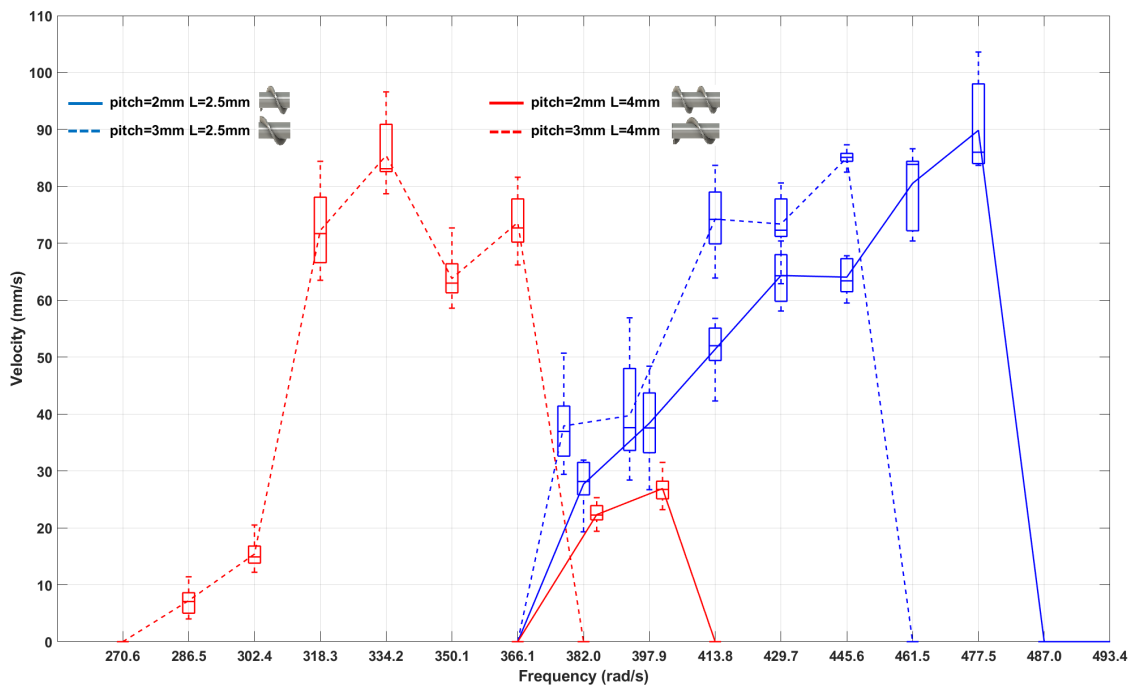


Figure 25: Maximum linear velocity vs Magnetic field rotational frequency of four robot robots. Each data point represents 10 trials.

Two different lengths (2.5 mm and 4 mm) and two different pitches (2 and 3 mm) were tested and compared. The velocity of each swimmer was calculated by measuring the time swimmers took to go through the 20 mm long tube. The velocity results of all designs are presented in Fig. 25. Each rotational speed contains ten trials.

From experimental results, the fastest swimmer is the one with a pitch of 2 mm and a length of 2.5 mm as shown as Fig. 24 (a). This swimmer climbed at an average speed of 90 mm/s with a maximum recorded velocity of 103.6 mm/s. The variation in velocity is explained by the fact that

the controller must compensate for uncertainties to keep the swimmer on the centerline by slightly changing the robot's orientation. The uncertainties are not the same for each loop achieved.

The maximum torque that the manipulator can apply was the same for each test. The maximum applied torque is

$$\Gamma = \mathbf{m} \cdot \mathbf{B}. \quad (58)$$

The angle between the applied magnetic field \mathbf{B} and the magnetization \mathbf{m} of the swimmer is called internal angle (α_i), similar to the terminology used for synchronous electric motors. The maximum torque is reached when α_i reaches $\pi/2$ rad. If this angle is exceeded, the torque applied decreases. The robot's angular velocity also decreases and is no longer equal to the rotational speed of the applied magnetic field. Under these conditions and according to (58), the average torque applied to the robot is considered equal to zero. The robot, therefore, stops rotating. The frequency produces an internal angle equal to $\pi/2$ is called the step-out frequency.

As shown as the experimental curves, the step-out frequency is decreased when the robot length increases, and the pitch increased, which is explained by the fact that, for a given rotational speed, the friction torque increases with the length of the swimmer, and more contact surface area with the liquid. The torque also increases if the pitch is increased as the attack angle of the screw thread increases.

All robots have a diameter of 2.5 mm, and their cross-section is, therefore, the same. There is a maximum amount of liquid for a given rotational speed that can go through this surface area. It is equal to $S \cdot P \cdot \omega / (2\pi)$ where S is the cross-section area of helix, P are the pitch, and ω is the rotational speed. It can be seen in Fig. 25 that the robot with a pitch of 2 mm and a length of 4 mm performs poorly. This can be explained by the fact that the increased length only increased the operation frequency range and step-out frequency. However, this small increase does not compensate for the added weight. Also, the friction torque produced for a given rotational speed is increased, decreasing the step-out frequency.

3.4 3D Navigation with PI Controller

In this section, the experimental results of 3D navigation with a PI controller are presented. And an orientation controller is proposed to improve the path-following performance.

3.4.1 Preliminary 3D Navigation Study with PI Controller

The PI controller discussed in Section 3.3.1 and the swimmer with a pitch of 2 mm and a length of 2.5 mm shown as Fig. 24 were tested experimentally. The desired trajectory goes straight up through a tube. It exits the tube from the top and goes to the right side of the workspace. The trajectory then makes several turns to bring the robot to the bottom of the workspace slowly. And the swimmer follows the desired trajectory until halted. A 3D schematic of the desired course is provided in Fig. 26. This figure also shows the experimental results of the swimmer.

A significant error between the desired trajectory and the swimmer trajectory happened when the trajectory is tortuous. However, the control is precise and repeatable for each loop performed. The orange curve in Fig. 26 corresponds to the path followed by the robot while accomplishing the trajectory three times in a row. The trails are almost superposed. And the path-following is accurate on the portion that the swimmer goes up into the tube. The swimmer can go through the tube without touching the walls. However, the average path-following accuracy is about 10 mm.

3.4.2 Orientation Controller

The path-following controller in this section is the same PI controller presented in Section 3.3.1. After each robot position measurement, the closest waypoint to the robot, $\mathbf{P}[i]$, was identified. The path controller determines $\mathbf{u}(t)$, the orientation of the magnetic field rotation axis. Although the swimmer can follow the desired trajectory by the proposed closed-loop PI controller in the preliminary study, the average path-following error is huge. The maximum is around 10 mm. A new orientation controller is proposed to compensate for the error and smooth the swimmer trajectory to improve the path-following performance with the proposed closed-loop PI controller.

Two components are used to calculate $\mathbf{u}(t)$: the path tracking error ($\mathbf{P}[i] - \mathbf{x}(t)$) and the (discretized) tangent to the path. There are two tuning parameters: $\beta \in (0, \infty)$ to control the relative

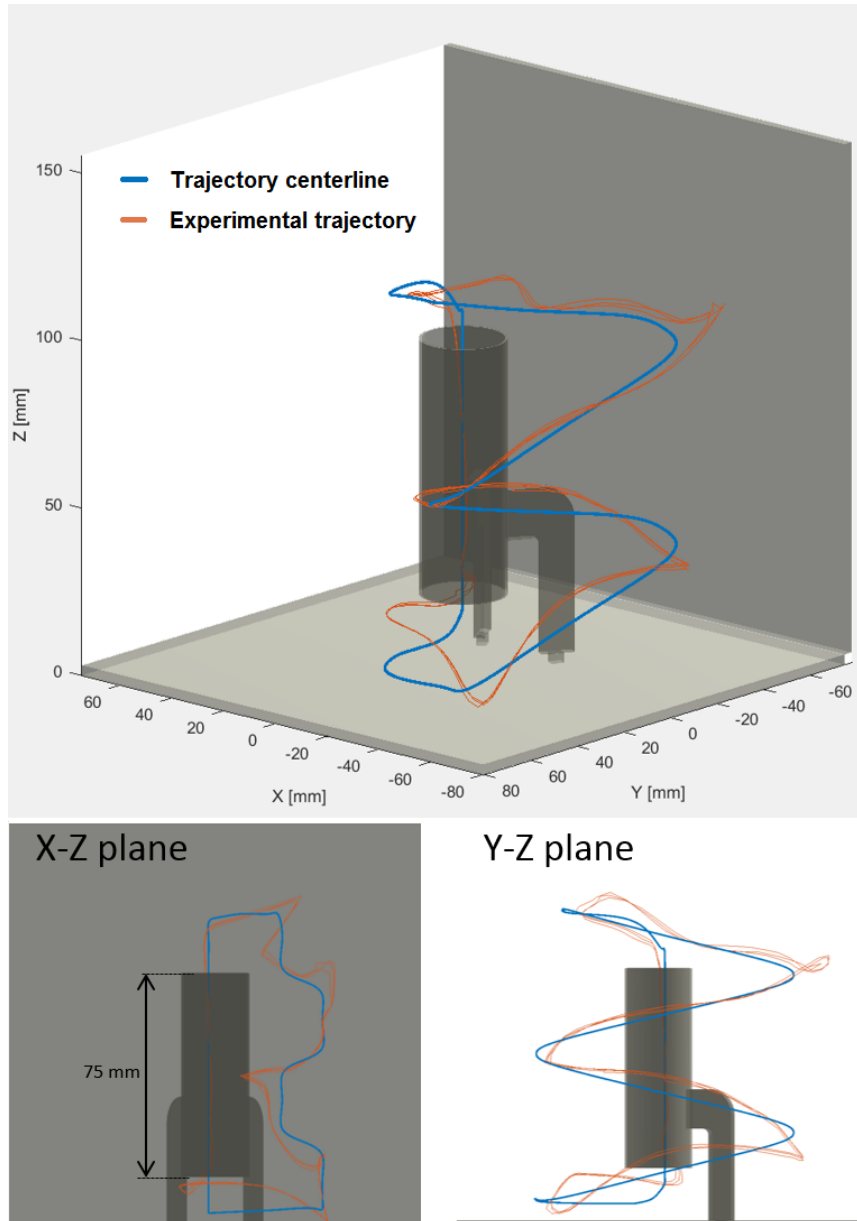


Figure 26: Experimental results of path-following following experiments.

importance of path error and the path tangent, and $\gamma \in \mathbb{Z}^+$ which determines the distance along the path to compute the tangent. Small values of β attempt to track a waypoint but do not progress along the path well, while large β values result in paths that diverge from the waypoints (see Fig. 27). Because the waypoints are spaced every 0.5 mm, a γ of 1 set a lookahead of 0.5 mm for the

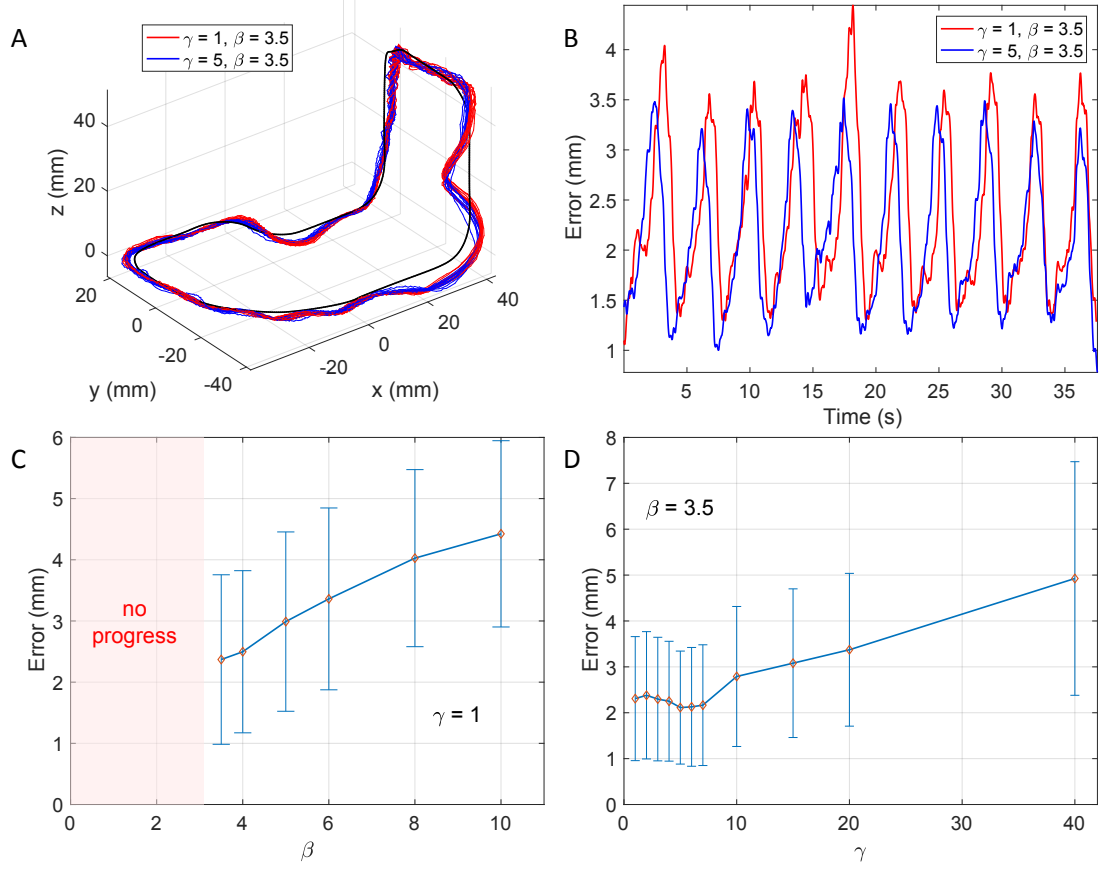


Figure 27: Path-following results by a helical swimmer. (A) 3D path-following results of two sets parameter values. (B) Path-following error. (C) and (D) show parameter studies on γ and β . Each data point represents 10 laps around the path.

tangent calculation

$$\mathbf{f}(t) = (\mathbf{P}[i] - \mathbf{x}(t)) + \beta \left(\frac{\mathbf{P}[i + \gamma] - \mathbf{P}(i)}{\|\mathbf{P}[i + \gamma] - \mathbf{P}[i]\|_2} \right), \quad (59)$$

$$\mathbf{u}(t) = \frac{\mathbf{f}(t)}{\|\mathbf{f}(t)\|_2}, \quad (60)$$

$$\text{and } \omega(t) = 160. \quad (61)$$

The sign of $\omega(t)$ is positive for right-hand screws and negative for left-hand screws. The magnetic axis direction $\mathbf{u}(t)$ must then be converted to a pair of angles

$$[\alpha_x(t), \alpha_y(t)] = [-\arctan2(\mathbf{u}_y(t), \mathbf{u}_z(t)), \sin^{-1}(\mathbf{u}_x(t))]. \quad (62)$$

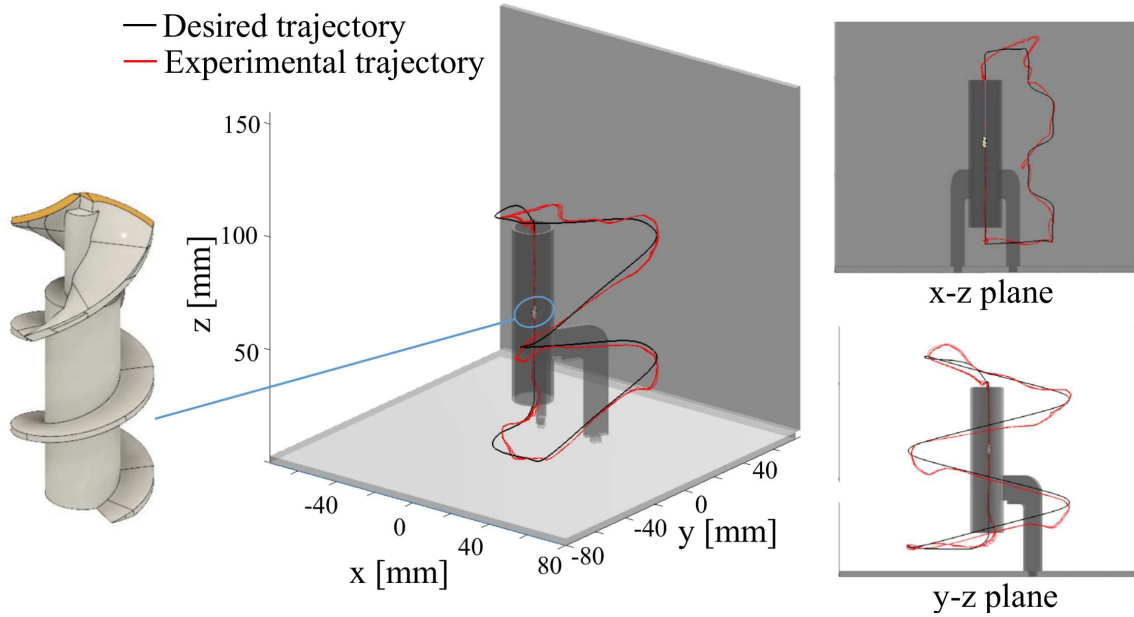


Figure 28: Plot of the path followed by the millimeter-scale swimmer during navigation through a tube. On this figure, the swimmer completes the trajectory four times.

Here $\arctan2(y, z)$ calculates the arctangent of y/z .

3.4.3 3D Navigation Study with PI Controller and Orientation Controller

The navigation experiment was performed using a swimmer designed for blood clot removal. The design parameters will be discussed in Section 3.6.3. As shown in Fig. 28, the path is followed with an average error of 2.3 mm, and a standard deviation of 1.8 mm. The path is precise, with a between-iteration mistake of 0.4 mm, and a standard deviation of 0.3 mm. Although the swimmer design is slightly different, the spiral tip did not significantly improve the path-following performance but the orientation controller. As the experimental results showed, the orientation control significantly improved the path-following performance.

3.5 3D Navigation with Adaptive Control

This section will discuss the design parameter optimization of the swimmer that appeared at the end of the previous section. The closed-loop PI controller and an orientation controller should be implemented to complete a high accuracy 3D navigation. Additionally, for the PI controller

Table 1: The Spiral-type Swimmer Designs

Schematic					
Details	1.0 Swimmer Single Helix Pitch: 1 mm	1.5 Swimmer Single Helix Pitch: 1.5 mm	2.0 Swimmer Single Helix Pitch: 2 mm	2.5 Swimmer Single Helix Pitch: 2.5 mm	3.0 Swimmer Single Helix Pitch: 3 mm
Std mean	7.1 mm	11.4 mm	7.4 mm	14.5 mm	15.2 mm
Std	3.3 mm	3.7 mm	2.7 mm	1.4 mm	1.5 mm

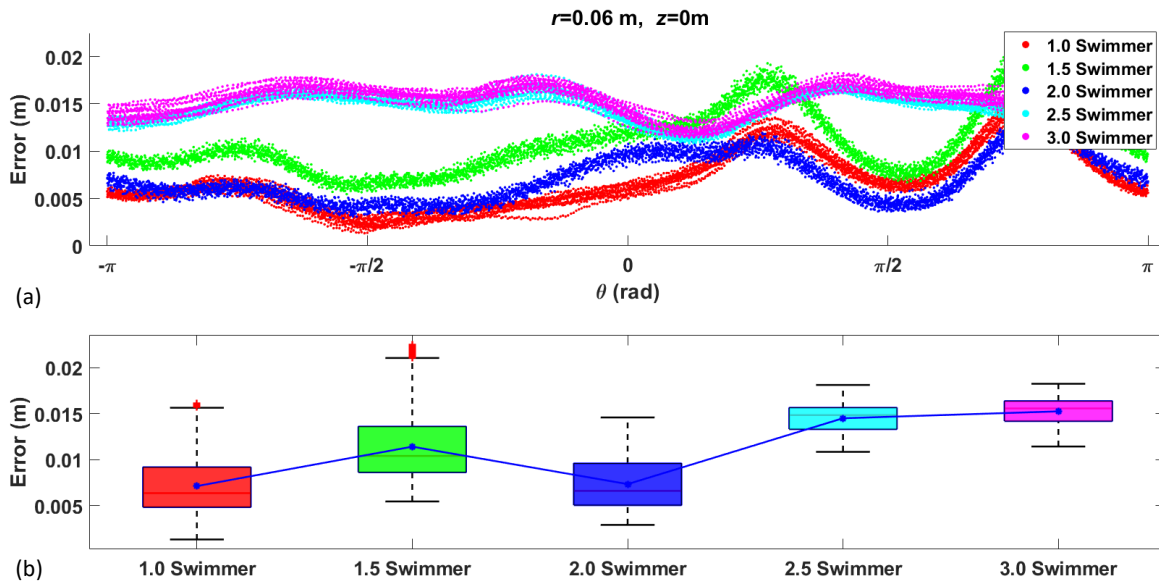


Figure 29: The PI controller Path-following results. (a) The path-following error. (b) The average error for each swimmer. Each marker represents 15 circular laps.

parameters, some important parameters are approximated and traded off by trial and error approach. This section proposed an adaptive control to achieve 3D navigation without approximated physical parameters of the swimmer to avoid this problem.

3.5.1 Experimental Setup

The lab-built magnetic robotic system presented in Section 3.2.1 was employed for the following studies. We decided to use current-mode power supplies to power the whole system to take advantage of the magnetic field's magnitude, which is proportional to the current and the magnetic

field has the same frequency as the current. The experimental results are shown in Fig. 30 (a) demonstrated that the band-pass of our magnetic system is about 100 Hz, where the output drops by -3dB. Fig 30 (c) indicates the whole system hardware diagram.

In all the subsequent experimental studies sections, the swimmer was driven in a water-filled workspace. Compared to other nano or micro helical robot studies, which focus on low Reynolds number ($Re \leq 10^{-3}$) environment, our millimeter-scale spiral-type swimmer is sketched to move at relatively high Re environment (e.g., for our cases, $Re_{\text{water}} \approx 727$). All swimmer designs are presented in Table 24 and 3D-printed by a ProJet 3510 HD Printer with a length of 6 mm and diameter of 2.5 mm.

3.5.2 Optimization Studies on Helical Tip Design

Table 2: Controller Comparison

Pitch	2 mm		3 mm	
Controller	PI	MRAC	PI	MRAC
Mean (mm)	7.4	3.2	15.2	3.8
Std (mm)	2.7	1.5	1.5	1.8

This section presents the new swimmer design compare to the design shown in Section 3.3.3. The new design was added a helical tip, which is used for the blood clot removal studies in later sections. There are five thread-pitch values experimentally studied to explore how the new design affects swimming stability. The word “stability” is defined as and evaluated by the mean and standard deviation (std) of path-following error in this and later section, which is inversely proportional to the mean path-following error. The pitches of swimmer designs in Table 24 are 1 mm, 1.5 mm, 2 mm, 2.5 mm, 3 mm. The latest design has a helix tip comparing to the pure spiral-type body presented in [74, 75]. The latest designs are intended for potential clinical applications, blood clot removal.

At the beginning all swimmers were controlled by a PI controller presented in Section 3.3.1 rotating at 68 Hz, and followed a desired circle trajectory with z -axis = 0, radius = 60 mm. The pitches of the designs shown in Table 1 vary from 1 mm to 3 mm with 0.5 mm intervals. There

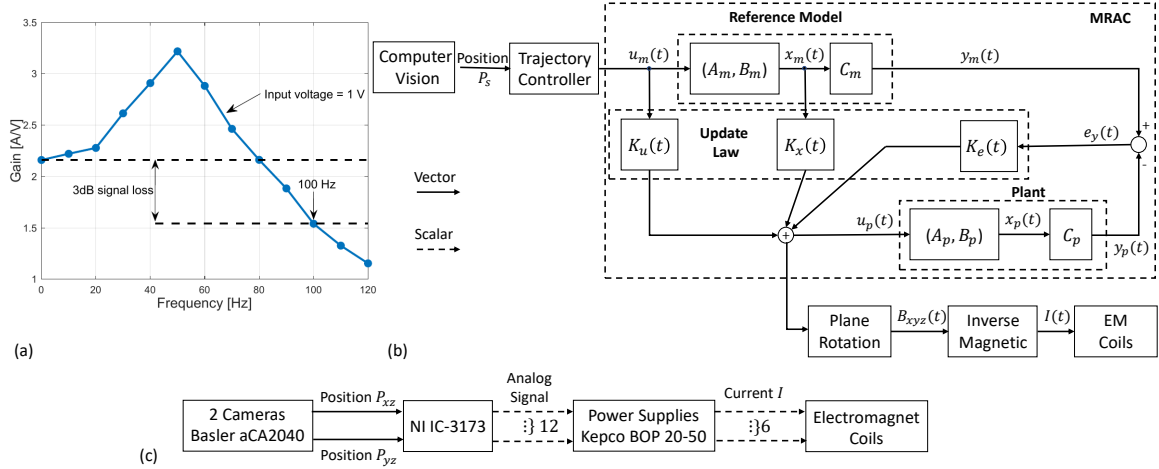


Figure 30: System diagrams: (a) The band-pass frequency of one coil. (b) and (c) are control and hardware diagrams.

is a total of 15 trials conducted for each design. The path-following tracking error is plotted as a function of angular progress around the circle is shown in Fig. 29(a). From results of fig. 29(b), the 2.0 Swimmer whose thread pitch is 2 mm, had the best stability (mean error = 7.4 mm, std = 2.7 mm), and the 3.0 Swimmer whose thread pitch is 3 mm, has the worst stability (mean error = 15.4 mm, std = 1.5 mm).

3.5.3 Model Reference Adaptive Control(MRAC)

In our previous work [77,81], we used a PI controller to guide the swimmer in a 3D environment. To improve the mean error and standard deviation of path-following, we implemented a controller used a feed-forward component to counterbalance the acceleration produced by gravity and drag. Moreover, all the swimmer mass values, thrust coefficient, and drag coefficients were hand-tuned by a trial-and-error approach to control the swimmer following the trajectory in 3D.

In contradiction, the direct MRAC is used to adjust an unknown time-variant or time-invariant plant in real-time and regulate the plant to the desired system dynamics. The preferred system dynamics is called the reference system or model. Because our system is a high nonlinear time-variant system because of the dynamics and disturbance, MRAC can address the robustness and model uncertainties caused by nonlinearity without approximating the dynamic or kinematic parameters. The Demonstrations and analysis of a nonlinear system implemented direct MRAC are presented

in [85]. The simulated and experimental results are shown in [86, 87], which proved that an MRAC controller could afford a faster convergence transient and tracking performance than a PI controller. The adaptive on-line adjustment mechanism of MRAC can be derived from the laws developed in [88] or using a candidate Lyapunov function [89]. The comprehensive MRAC mathematical model is shown as follows, and the plant is defined as

$$\dot{x}_p(t) = A_p x_p(t) + B_p u_p(t) \quad (63)$$

$$\text{and } y_p(t) = C_p x_p(t), \quad (64)$$

where A_p, B_p, C_p are the matrix in state-space form, and $x_p(t), y_p(t), u_p(t)$ are the states, output and input of the plant in state-space form. The reference model is defined as

$$\dot{x}_m(t) = A_m x_m(t) + B_m u_m(t) \quad (65)$$

$$\text{and } y_m(t) = C_m x_m(t), \quad (66)$$

where A_m, B_m, C_m are the state-space matrix of the reference model. A_m is a Hurwitz matrix, which means the spectrum of A_m is composed of eigenvalues with negative real parts. $x_m(t), y_m(t)$ are the states, output of the reference model in the state-space form, and $u_m(t)$ is the trajectory input.

In this paper, the MRAC algorithm is derived according to the Command Generator Tracker (CGT) shown in [85]. The derivation and stability examination of this controller is given and demonstrated in [85]. The control diagram is shown as Fig. 30 (b).

The equations from (67) to (70) define the MRAC controller. $r(t)$ is the input of the on-line adaptive adjustment mechanisms

$$r(t) = \begin{bmatrix} e_y(t) \\ x_m(t) \\ u_m(t) \end{bmatrix}, \quad (67)$$

where $e_y(t)$ is defined as $y_m(t) - y_p(t)$. $K(t)$ is the summation of the adaptive gains $K_a(t)$ and the

nominal gains $K_n(t)$ shown as (68). It can also be represented by gains of states in $r(t)$ as (69).

$$K(t) = K_a(t) + K_n(t) \quad \text{or equivalently,} \quad (68)$$

$$\text{and } K(t) = \begin{bmatrix} K_e(t), K_x(t), K_u(t) \end{bmatrix}. \quad (69)$$

Consequently, the system input is the state feedback on $r(t)$ shown as

$$u_p(t) = K(t)r(t). \quad (70)$$

And the on-line adaptive adjustment mechanisms of $K(t)$ are

$$\dot{K}_a(t) = (y_m(t) - y_p(t)) r^T(t) \Upsilon, \quad \Upsilon > 0 \quad (71)$$

$$\text{and } K_n(t) = (y_m(t) - y_p(t)) r^T(t) \tilde{\Upsilon}, \quad \tilde{\Upsilon} > 0. \quad (72)$$

The Υ and $\tilde{\Upsilon}$ in the above equations should be positive definite and positive semidefinite coefficient matrices. In our studies, $\Upsilon = \tilde{\Upsilon} = 10\mathbb{I}_3$. Because the dynamics of our system exhibits similar characteristics as a second-order system, a second-order system was picked as the reference model for all degrees of freedom. And the A_m and B_m of the reference model are defined as

$$A_m = \begin{bmatrix} 0 & \mathbb{I}_3 \\ -\omega_n^2 \mathbb{I}_3 & -2\omega_n \zeta \mathbb{I}_3 \end{bmatrix} \quad (73)$$

$$\text{and } B_m = \begin{bmatrix} 0 & \omega_n^2 \mathbb{I}_3 \end{bmatrix}^T, \quad (74)$$

where \mathbb{I}_n is the identity matrix of size n . The state of the reference model x_m is

$$x_m = \begin{bmatrix} X_m & Y_m & Z_m & \dot{X}_m & \dot{Y}_m & \dot{Z}_m \end{bmatrix}^T, \quad (75)$$

where X_m , Y_m , and Z_m are displacements along each axis, and respectively, \dot{X}_m , \dot{Y}_m , and \dot{Z}_m are the velocities. The plant and the reference model have the same states. The top and right-side

cameras can gain position information. The velocity can be approximated by the amount of change in the position measurements times the frame rate. We set the damping ratio of the reference model $\zeta = 1$ to make the reference critically damped and set the natural frequency $\omega_n = 5$ rad/s, which can yield a 90% rise time of about 0.8 sec. The chosen parameters $(\Upsilon, \bar{\Upsilon}, \zeta, \omega_n)$ were tuned through a trial-and-error approach to minimize the mean tracking error.

3.5.4 Controller Comparison

In the previous subsection 3.5.2, the best and worse swimmers among all presented works were Swimmer 2.0 and Swimmer 3.0, respectively. This section experimentally compared path-following performance using the PI controller and MRAC on both the best and the worst swimmers. The rotation frequency for all experiments is set as a constant value 68 Hz. The predefined circle trajectory has a radius of 60 mm and placed in the $x - y$ plane, where $z = 0$ m. Fifteen trials were conducted for each combination of swimmer and controller.

The path-following results of MRAC shown in Fig 31(a) and (c) are the results with the pre-trained adaption matrix to save the on-line adaption and convergence process time. The error is the Euclidean distance between the current swimmer position and the desired path's closest point.

The path-following controller comparison results of 2 mm pitch swimmer is shown in Fig. 31(a). Because the 2.0 Swimmer was more stable than the other swimmers, both controllers' tracking curves were mostly overlapped. But the results of MRAC are concentrated in a low band comparing to the oscillation of the PI controller. Table 2 shows the mean and standard deviation of the position error of the PI controller and MRAC. Compared to the results of 2.0 Swimmer using the PI controller, the MRAC significantly reduced the mean error by 56.75 % and the std by 44.44 %.

The path-following error results of the 3.0 swimmer are shown in Fig. 31(c). The numerical results of mean \pm std for the PI controller and MRAC are shown in Table 2.

From Table 2, we can conclude that the MRAC significantly improved the tracking performance, even using the 3.0 Swimmer comparing to the PI controller, and the MRAC reduced the mean error by 75.0 %. The path-following performance of both swimmers using MRAC is within 6 mm, which is one body length of the swimmer, considering the mean error \pm std. A box and whisker plot

comparison of these controllers are shown in Fig. 31(b), which can more intuitively shows the performance gap between two controllers. The on-line adaption and convergence process of 3.0 swimmer is shown as Fig. 31(d). The mean error decreased from 10 mm to 5 mm within 100 sec, which is a fairly good accomplishment.

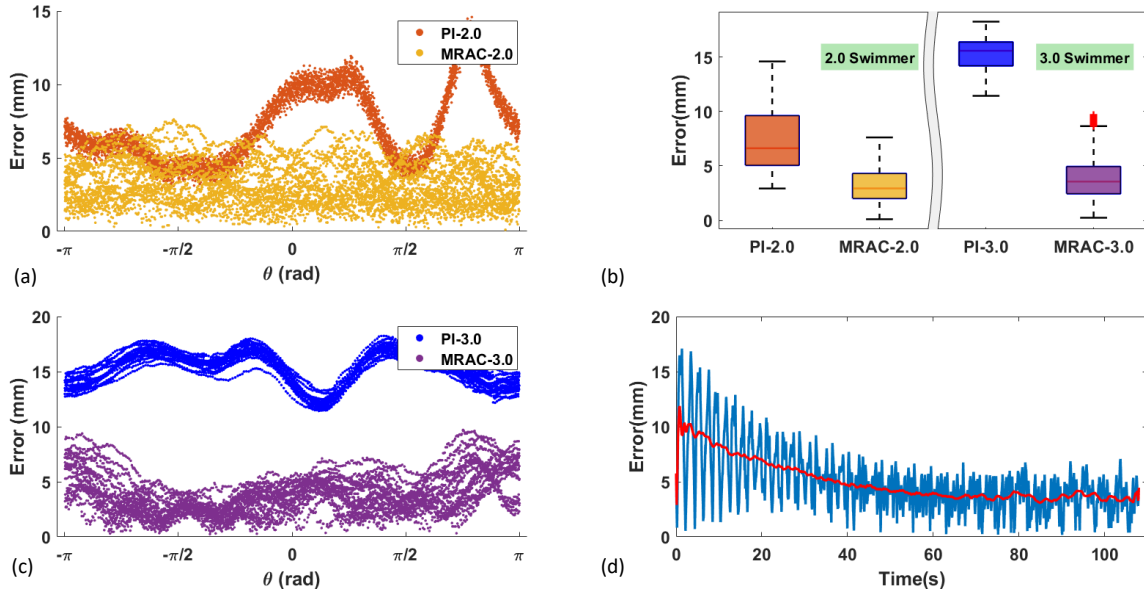


Figure 31: The experimental results of the comparison between PI controller and MRAC. The desired trajectory is a circle with z -axis = 0 mm, radius = 60 mm.

3.5.5 Path-Following Using MRAC

The 2.0 Swimmer and MRAC combination was used to follow a desired helical path to further investigate the MRAC's performance. The swimmer took off from the tank located at the left bottom corner, shown in Fig. 32(a). The swimmer then went through three pairs of 8 mm holes on the transparent acrylic board with three layers of heights. The path-following trajectory of the robot is presented in Fig. 32(a), and it contains ten trials. The mean error of this path-following trajectory is 4.2 ± 4 mm.

The swimmer is a non-holonomic robot, because the controllable degree of freedom is not equal to total degrees of freedom. When the goal location is assigned, the swimmer can only go forward or backward then make a turn to reach the goal location. If we consider a special case, such as in a narrow channel, it's better to retrieve the swimmer if it can back up. Thus, a forward & backward

motion is a big help for this special scenario. There is one additional set of MRAC control structure implemented in the program to achieve the backward path-following. The swimmer and applied input's body frame were flipped 180° during the backward movement. The forward and backward adaption matrix of MRAC can be switched, respectively. The forward motion orientation is defined as the helix tip leading shown in Fig. 32(c), and the backward motion orientation is defined as the tail leading shown in Fig. 32(d). As trajectories shown in Fig. 32(b), the swimmer started from Point A then moved forward to Point B. Then, the swimmer moved backward from Point B to Point A with body frame and direction flipped. The swimmer's forward motion trajectory is plotted in blue, and the backward motion trajectory is plotted in red. The experiment results shown in Fig. 32(b) contains ten trials. The mean error \pm std of the forward motion is 2.7 ± 1.6 mm, and the mean error \pm std of the backward movement is 3.5 ± 2.0 mm.

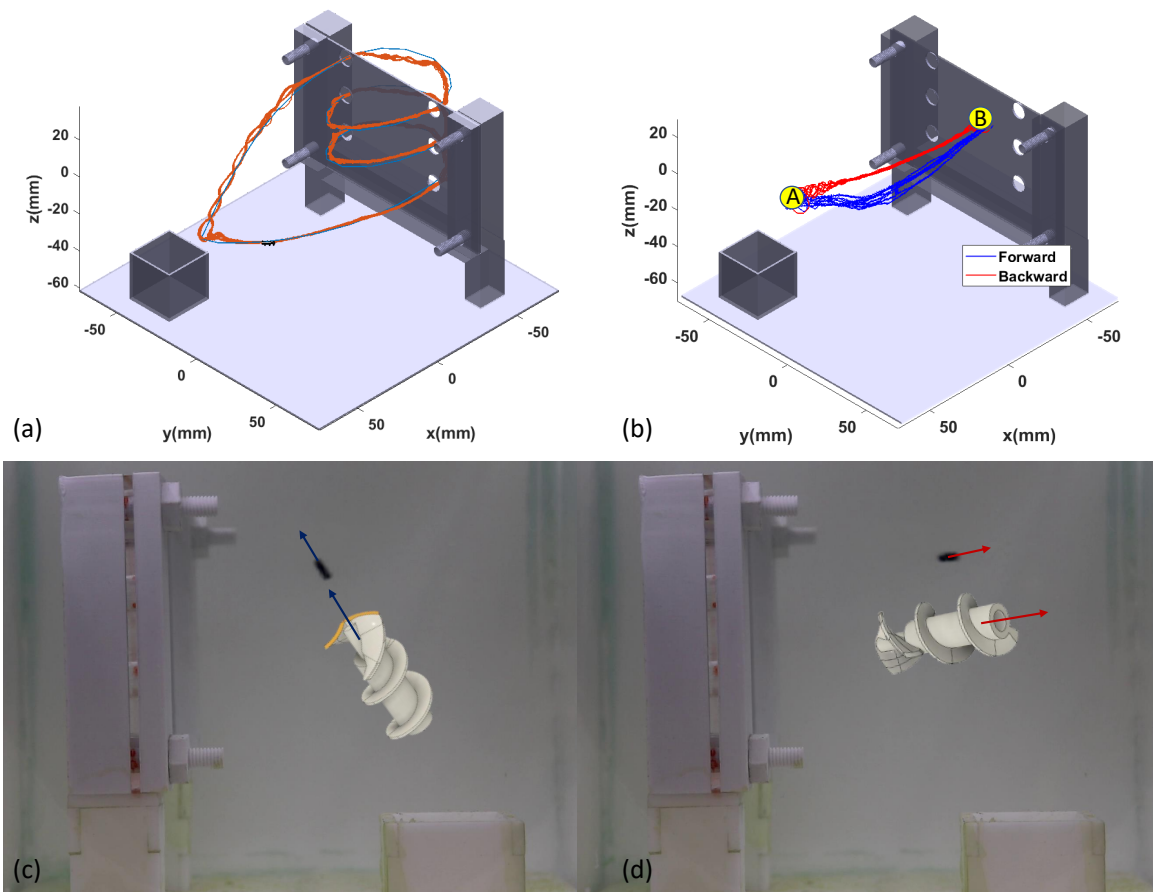


Figure 32: Experimental results of two motion studies using MRAC controller. Both experiments include 10 trails.

3.6 In Vitro Clinical Application Studies

3.6.1 Motivation of Blood Clot Removal Studies

The blood clotting is also called coagulation, which stops blood leakage after a vein or artery is damaged and forms a blood clot. The biological progress of coagulation is desirable, but if the blood clot is excessively coagulated inside a blood vessel, it may cause a health crisis. According to the reports in [90–95], one to two persons per thousand is negatively affected by a venous thrombosis every year. Moreover, around 18 persons per thousand may die because of the arterial thromboembolism [96]. Thromboembolism is usually treated by thrombolytic medications to dissolve the clot or using a catheter-related thrombolytic therapy [97–100]. Although they are common treatment approaches, both have some drawbacks. Thrombolytic medications could cause a life-threatening because of the pharmacological mechanism prevents the coagulation. This phenomenon was reported in [101, 102]. Catheter-based therapies use a long catheter inserted through arteries or veins, then guided by advanced imaging devices. As [103, 104] reported, while the catheter is guided to the target position, the body or the edge of the catheter may rub against the arteries' inner wall, which may detach arterial plaques. The detached plaques could travel within the bloodstream as the surgery and produce a blockage somewhere else, which may cause other unpredictable threatening or fatal consequences.

Miniature magnetic agents, such as the magnetic robot discussed in this section, are alternative solutions to these problems. These agents could be guided with external input sources and move along or against the bloodstream. Because of the complexity of actuation and control theory, the concept of blood clot removal using magnetic agents is still in the preliminary stage. As discussed in the previous section, researchers and scientists have evaluated it and studied it for decades. Moreover, more and more scientists started to investigate the feasibility of removing blood clots with such agents. As reported in [64, 105–112], the magnetic swimmer can produce thrust by rotating the helical shape fin and rub the clots with the screw-type or abrasive tip [113–116]. A helical swimmer with a diameter of 0.3 mm and a length of 4 mm can achieve a blood clot remove rate at 0.614 mm³/s [115]. The swimmer's position was regulated and detected in 1D by using an ultrasound scanner. And a model of rubbing on blood clots was proposed on [117]. For the 3D control studies,

an open-loop control study was performed by Sunky et al. to navigate the swimmer inside an artificial 3D vasculature and remove thrombi models [118]. The studies of helical magnetic swimmers closed-loop control inside a high viscosity fluidic environment were recently published [119–121].

3.6.2 Blood Clot Removal In Vitro Study

To prepare the in vitro study environment of blood clot removal, we used a SYLGARD™ 184 PDMS (Poly-dimethyl siloxane) elastomer to form a suitable channel for the thrombosis. PDMS has been used in many biological or clinical studies, and many researchers have used PDMS to model blood vessel [122]. As the manufacturer suggested, the elastomer resin is the mixture of 10 parts resin to 1 part curing agent and keeps mixing for 20 minutes. The mixture was put into a vacuum pump to get rid of the small air bubble. Finally, the elastomer resin was cured in a Petri dish with a diameter of 100 mm for 24 hours at room temperature. Three aluminum rods with a diameter of 3 mm were used as a support to form the channels. After the PDMS mode is cured, the model was cut, and the rods were removed. And the three channels allow us to allow performing three blood clot removal tests simultaneously. These PDMS channels were used to perform the blood clot removal tests reported in Section 3.6.3. A glass tube having an internal diameter of 3mm was used in the combined navigation and blood clot removal experiment in Section 3.6.4.

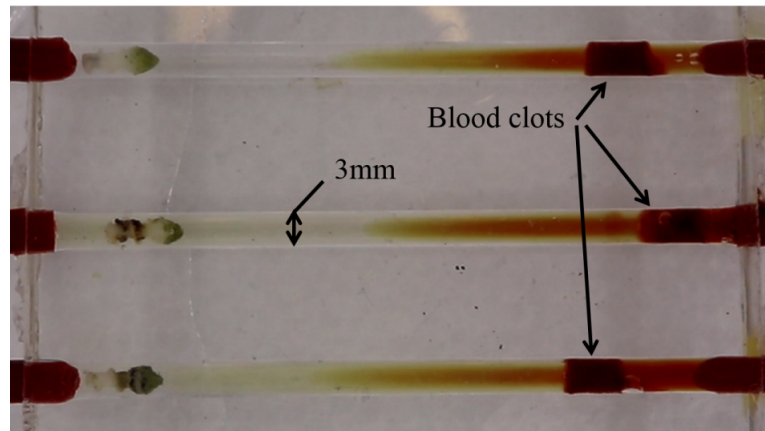


Figure 33: Picture of three swimmers inside PDMS channels.

Experimental protocol All blood clot removal experiments followed this protocol. The blood was taken from a healthy volunteer using a sterile lancet and dispensed onto a clean Petri dish.

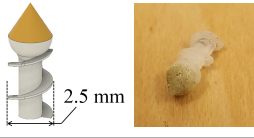
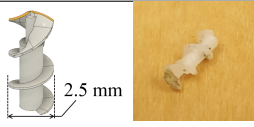
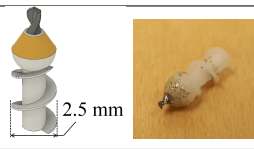
Fifty μL of blood was then pipetted into each channel while careful to avoid air bubbles, which generally takes five minutes. The blood formed an approximately 5 mm long cylindrical column. The clots were located about 10 mm away from the end of the inserted side of the channel. The magnetic manipulator was pre-heated to 37°C with the heater at the bottom of the workspace; then, the artificial blood clots were placed. The blood was left to solidify at this temperature for one hour. Until there are five minutes left in the timer, the channels were taken out of the manipulator and were filled with phosphate-buffered saline (PBS) to match the blood's pH value. The PDMS channels were then placed back into the magnetic manipulator and started the experiments when the timer alarm. After the experiments, all Petri dishes and PDMS models in contact with human blood were soaked and washed in 10% bleach to prevent contamination. Other materials were disposed of in a biohazard or sharps disposal box.

A Canon EOS RebelSL2 camera was used to record the whole removal process. The time t of blood clot removal taken by the swimmers was measured using a stopwatch. After the clots were completely removed, the removal rate was the ratio of clot volume and time t . If the clot was not completely removed, the removal rate was calculated by the recorded video, respectively.

3.6.3 In Vitro Study Results

Blood clot removal tests were performed at 45 Hz for four different swimmer designs following the experimental protocol described in the previous section. Table 3 summarizes the results of four designs. Designs A and C exhibited relatively low removal rates, which are $0.3 \text{ mm}^3/\text{min}$, and $1.76 \text{ mm}^3/\text{min}$, respectively. The swimmer C can quickly penetrate the clot with the drill bit, but progress significantly slowed down once the diamond powder-coated surface reached the clot. As Table 3 shows, design B and D showed higher removal rates. The low removal rate of designs A and C is that their tips have a large contact surface area, which reduces the pressure applied to the clot and increases the resistance that slows down the swimmer. Designs B and D have a smaller design tip that applies a larger and shaper pressure on the clot, which applies greater mechanical stress on the blood clot. The shape of the helical tip coated with diamond powder can rub the clot down from the fibrin network, which results in higher removal rates. The sharp edges can stick into the clot,

Table 3: Comparison between the removal rate of different swimmer designs at 45 Hz. A single test was performed for each design. Design B has the highest removal rate.
 Legend: ■ = diamond powder, ■ = acrylate, ■ = drill bit.

Swimmer Design	Removal rate in mm ³ /min	Remarks
A: 	0.3	Experiment was stopped after 14 min due to slow progress. Incomplete clot removal.
B: 	12.3	A blood clot with volume of 50 mm ³ completely removed.
C: 	1.76	Experiment was stopped after 14 min due to slow progress. Incomplete clot removal.
D: 	10.3	Experiment was stopped after 4 min because swimmer became stuck in the clot and stopped rotating.

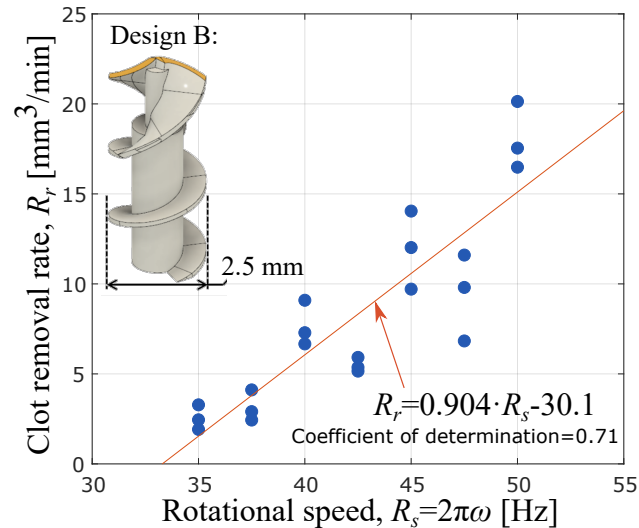


Figure 34: model fit of blood clot removal rate vs rotation frequency.

while the smooth tip can not achieve a high removal rate. So it's a trade-off on the tool design. The removal rate of Design B at 45 Hz was 12.3 mm³/s comparing to the thrombolytic medication, streptokinase, which has a removing rate at 0.17 mm³/s [117]. Design D became stuck in the blood clot and stopped rotating when approximately 20% of the clot was left.

The blood clot removal rate is proportional to the rotation frequency as long as it is below the step-out frequency about 55 Hz. The relationship between R_r and R_s is approximately linear and can be approximated by $R_r = 0.904 \cdot R_s - 30.1$ with a coefficient of determination $R^2=0.76$ shown as Fig. 34. The maximum removal rate (20.13 mm³/min) was observed at 50 Hz. The measured values of removal rate present some inconsistency, shown in the relatively low R^2 value. Because the experiments were performed over three weeks, the blood was volunteered by a single volunteer, which is not sufficient from a stochastic view. The measurements were performed at rotational speeds lower than 55 Hz and, therefore, the swimmer did not step out of magnetic field synchronization during the experiments.

3.6.4 Combined 3D Navigation and Blood Clot Removal

As demonstrated in Section 3.4.3, the type of swimmer B can perform 3D navigation and abrade blood clots efficiently shown in Section 3.6.3. In this section, we would like to combine both 3D navigation and blood clot removal as a single experiment. A 3 mm tube was attached perpendicular to a 15 mm tube using epoxy resin. Both tubes are transparent, which allows the visual feedback of the swimmer's position with the Basler cameras. A 15 mm tube is vertically supported by two plastics holder at the center of the workspace. A blood clot was made inside the 3 mm tube following the protocol detailed in Section 3.6.2. The workspace was filled with PBS solution and heated to 37°C. A cylindrical case (diameter $D = 15$ mm and height $H = 15$ mm) was designed at the bottom of the workspace. It was used to prevent the swimmer from moving in the workspace between tests and ensured the same start location. The swimmer was programmed to exit the case firstly, then enter the 15 mm tube from the bottom, and swim upward. It then made a sharp turn to enter the 3 mm tube. The orientation controller described in Section 3.4.2 was used, and the parameters are $\gamma = 1$ and $\beta = 4$. These values were tuned with a trial and error approach to enable a smooth entry inside the 3 mm tube. When the swimmer contacted the blood clot, the system was switched to the open-loop blood clot removal mode, and the magnetic field was set to 45 Hz. The total time of blood clot removal was 161 s. Snapshots from the video of the experiment are presented in Fig. 35. This test experimentally demonstrates that a magnetic swimmer can perform

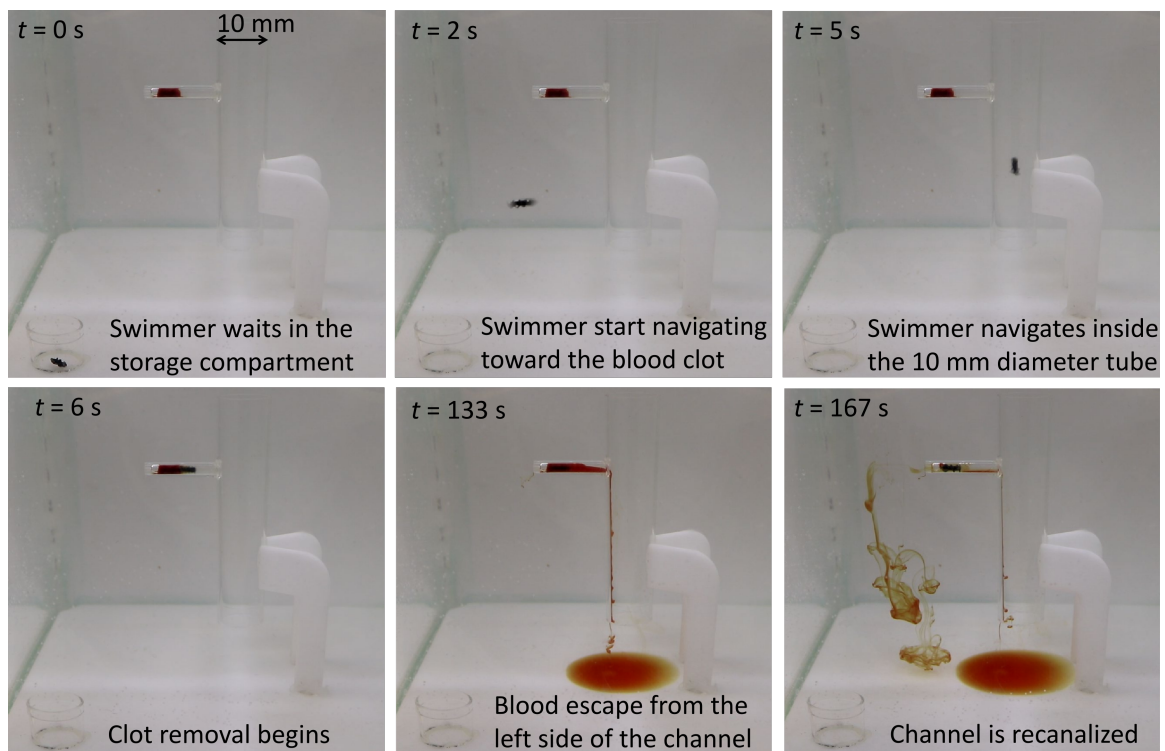


Figure 35: Snapshots from the video the combined 3D closed-loop path following and blood clot removal experiment.

both the functionalities of 3D navigation and blood clot removal for the first time.

4 ULTRASOUND GUIDANCE STUDIES

4.1 Introduction

As mentioned in Section. 3.6.1, a blood clot may be life-threatening if the blood clot blocks a blood vessel. A life-threatening blood clot is usually formed in a vein or artery to stop blood leakage when a bleeding point occurs. However, the blood clot may detach and flow to deep-seated regions along with the bloodstream and cause a health crisis. In general, there are two treatment approaches, thrombolytic medications, and catheter-related thrombolytic therapy. Still, negative side effects come with these two methods, and medical precautions and comprehensive tests are necessary to avoid or compensate for the negative side effect. As demonstrated in [123], the side effect of thrombolytic medications can be compensated through drug delivery using micro-robot or deceives controlled with the external input sources. As we have discussed so far, the magnetic robot is one of the most guaranteed clinical studies agents.

There is also some famous external magnetic system generally used for academic studies such as a Helmholtz coil. In [124], Vonthron, Manuel group has proposed and demonstrated the preliminary experimental studies on the potential of integrating the MRI scanner with a micro-robotic navigation system. The pioneer results prove the clinical values of the magnetic robot and the validation that the MRI can be the external magnetic source. Moreover, the MRI can also provide imaging feedback for closed-loop control. Most research groups use the visual system for the feedback sensor used in the closed-loop studies of the magnetic robot system. And we have used two Basler cameras in our previous control studies to capture the positioning information of the magnetic swimmer. Because the blood clot is formed in the vein, artery, or deep-seated region of the human body, the visual feedback can not be the option to provide the magnetic robots' location information. Thus, other feedback sources should be considered for the clinical application in vitro study instead of the cameras. As mentioned above, the MRI is one of the guaranteed image processing for diagnosis and can also provide an external input source. Still, for academic studies and lab works, the ultrasound is a better replacement comparing to the radiation exposure caused by X-ray. As the Islam S. M. Khalil et al. has demonstrated in [115], they have proposed and analyzed the experimental studies

on blood clot rubbing using ultrasound as positioning information feedback for the closed-loop control of the magnetic robot. This chapter will then focus on the feasibility studies on combining an ultrasound as a feedback sensor instead of the camera in our magnetic system. Comparing with results and experimental setups shown in [115], the workspace of our system is much bigger. And our studies focus on 3D navigation, so our 2D ultrasound transducer can not be seated at a single position on the workspace. To solve this problem, we would like to employ a UR3 robot arm to carry the ultrasound probe to move, track, and provide the positioning information of our magnetic swimmer.

In this section, we would like to discuss three aspects to integrate ultrasound into our system to provide the positioning feedback for the closed-loop control. In the first subsection, we would like to review the kinematics concepts of the robot arm for tracking and impedance control to keep a constant contact force and guarantee a high-quality ultrasound image for the control system. The approaches for improving the quality of ultrasound images of our magnetic swimmer and detection algorithms were then presented. Finally, the experimental studies are presented, and the results are analyzed in the last subsection.

4.2 Robot Arm Control

4.2.1 Kinematics of UR3

A single robot pose can be described in robotics studies and presented in two formats, joint space and cartesian space. For a robot arm, the joint angular position and tool center point(TCP) orientation and position can mutually be transformed by the forward and inverse kinematics calculation. The robot arm can be thought of as a link chain of various joints such as revolute and prismatic joints. Each joint has a single-degree-of-freedom. So the objective of forward kinematic is to determine the cumulative effect of the entire link chain, from the base to TCP. For the universal robot shown as Fig. 36 presented in [125], the UR robot has six links numbered from 1 to 6 starting from the base. Here we define a homogeneous matrix A_i , which can transform a point p_j from frame j to frame i as

$$p_j = A_i^j(p_i), \quad (76)$$

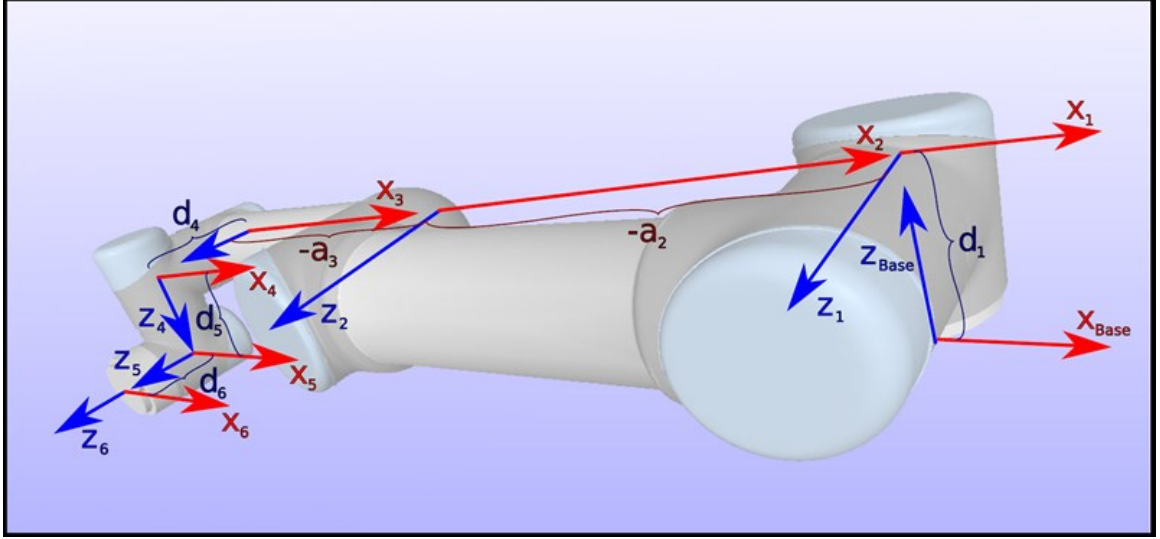


Figure 36: The joint frames of UR robot.

where i indicates the target frame and j is the current frame. In general the homogeneous matrix A_i^j has the form as

$$A_i^j = \begin{bmatrix} R_i^j & d_i^j \\ 0 & 1 \end{bmatrix}, \quad (77)$$

where the position and orientation of frame j with respect frame i is denoted by a 3×1 vector d_i^j and a 3×3 rotation matrix R_i^j . Conventionally, a transformation matrix T_i^j is denoted as

$$T_i^j = A_{i+1} A_{i+2} \cdots A_{j-1} A_j = \begin{bmatrix} R_i^j & d_i^j \\ 0 & 1 \end{bmatrix}. \quad (78)$$

For the universal robot and the frames is defined as Fig. 36, the transformation matrix T_{Base}^6 is

$$T_{Base}^6 = T_{Base}^1 \cdot T_1^2 \cdot T_2^3 \cdot T_3^4 \cdot T_4^5 \cdot T_5^6. \quad (79)$$

The rotation matrix R_i^j is denoted as the orientation of frame j respect to frame i , and it is given by

$$R_i^j = R_i^{i+1} \cdots R_{j-1}^j. \quad (80)$$

And the vectors d_i^j is recursively computed by

$$d_i^j = d_i^{j-1} + R_i^{j-1} d_{j-1}^i, \quad (81)$$

this equation will be used in later description of Jacobian matrix.

In the robotics application, the most commonly used convention for selecting the reference frame is the Denavit-Hartenberg or, in brief, called the DH matrix. In this convention, the homogeneous transformation matrix A_i^j is presented as a product of four "basic" transformations

$$A_i^j = Trans_{z_{n-1}}(d_n) \cdot Rot_{z_{n-1}}(\theta_n) \cdot Trans_{x_n}(a_n) \cdot Rot_{x_n}(\alpha_n),$$

$$Trans_{z_{n-1}}(d_n) = \begin{bmatrix} 1 & 0 & 0 & 0 \\ 0 & 1 & 0 & 0 \\ 0 & 0 & 1 & d_n \\ 0 & 0 & 0 & 1 \end{bmatrix},$$

$$Rot_{z_{n-1}}(\theta_n) = \begin{bmatrix} \cos \theta_n & -\sin \theta_n & 0 & 0 \\ \sin \theta_n & \cos \theta_n & 0 & 0 \\ 0 & 0 & 1 & 0 \\ 0 & 0 & 0 & 1 \end{bmatrix}, \quad (82)$$

$$Trans_{x_n}(a_n) = \begin{bmatrix} 1 & 0 & 0 & 0 \\ 0 & 1 & 0 & 0 \\ 0 & 0 & 1 & d_n \\ 0 & 0 & 0 & 1 \end{bmatrix},$$

$$Rot_{x_n}(\alpha_n) = \begin{bmatrix} 1 & 0 & 0 & 0 \\ 0 & \cos \alpha_n & -\sin \alpha_n & 0 \\ 0 & \sin \alpha_n & \cos \alpha_n & 0 \\ 0 & 0 & 0 & 1 \end{bmatrix},$$

where d_n is the translation displacement along z -axis of frame $n-1$, θ_n is the rotation angle about z -axis of frame $n-1$, a_n is the translation displacement along x -axis of frame n , and α_n is the rotation

Table 4: UR3 DH Parameters

UR3							
Kinematics	θ [rad]	a [m]	d [m]	α [rad]	Dynamics	Mass [kg]	Center of Mass [m]
Joint 1	0	0	0.1519	$\pi/2$	Link 1	2	[0, -0.02, 0]
Joint 2	0	-0.24365	0	0	Link 2	3.42	[0.13, 0, 0.1157]
Joint 3	0	-0.21352	0	0	Link 3	1.26	[0.05, 0, 0.0238]
Joint 4	0	0	0.11235	$\pi/2$	Link 4	0.8	[0, 0, 0.01]
Joint 5	0	0	0.08535	$-\pi/2$	Link 5	0.8	[0, 0, 0.01]
Joint 6	0	0	0.0819	0	Link 6	0.35	[0, 0, -0.02]

angle about x -axis of frame n . Thus, we can use 4.2.1 to compute the position and orientation of the TCP. The DH parameter table of UR3 can be found through the URL link [125], which is shown as Table. 4. If the desired TCP position and orientation are given, each joint position can be calculated using inverse kinematics. Unlike forward kinematics, inverse kinematics is usually much more difficult and may or may not have a solution for a certain position and orientation, which is called the singularity. Even there is a solution for the inverse kinematics, it may or may not be unique. Generally, the inverse kinematics can be solved by Kinematic decoupling and geometric approach, which we will not discuss further for these two approaches.

We have seen the forward kinematics equation for the transformation between Cartesian space and the joint space. Suppose we want to find the relationship between velocity, force, torque between joints. In that case, the Jacobian matrix builds the linkages of all, which is also one of the most important quantities to analyze and control the robot motion. The Jacobian can be thought as a vector version of the ordinary derivative of a scalar function. Because the Jacobian presents the velocity relationship between joints, so it is defined as

$$\begin{bmatrix} v_{Base}^n \\ \omega_{Base}^n \end{bmatrix} = J_{Base}^n \dot{q}, \quad (83)$$

where v_{Base}^n and ω_{Base}^n are the linear, and angular velocity of frame n respect to Base, J_{Base}^n is the Jacobian matrix of frame n respect to Base, and \dot{q} is the vector of joint velocity. And the J_{Base}^n is given by

$$J_{Base}^n = \begin{bmatrix} J_v \\ J_\omega \end{bmatrix}. \quad (84)$$

The Jacobian matrix of a robot arm lik manipulator has the form

$$J = \begin{bmatrix} J_1 & J_2 & \dots & J_n \end{bmatrix}. \quad (85)$$

If the joint i is revolute, the i -th column of J is given by

$$J_i = \begin{bmatrix} z_{i-1} \times (o_n - o_{i-1}) \\ z_{i-1} \end{bmatrix}, \quad (86)$$

if it is a prismatic joint, the J_i is given by

$$J_i = \begin{bmatrix} z_{i-1} \\ 0 \end{bmatrix}, \quad (87)$$

where z_{i-1} is the unit vector of frame $i - 1$ expressed in the orientation of the base frame, which can be computed by

$$z_j = R_0^j K, \quad (88)$$

where $K = z_0 = [0, 0, 1]$. And the conversion between torque τ and force F by using the Jacobian matrix are

$$\tau = J^T F \quad (89)$$

$$\text{and } F = (J^T)^{-1} \tau. \quad (90)$$

In our studies, the UR3 is programmed in Robotics Operation System (ROS) with Python and C++.

The Universal robot provides the UR robot driver, So all the dynamics and kinematics calculation was included.

4.2.2 Hybrid Control

Ultrasound is extensively used in medical diagnosis as a non-invasive tool. We plan to use the ultrasound as a replacement for the camera to provide the positioning information of the magnetic swimmer for the closed-loop control and carried by UR3 robot arm. Generally, the ultrasound probe is held and angled by an ultrasonographer to capture ultrasound images, but the contact force and heading orientation are implicit. A hand-controlled design was proposed in [126] to quantify the force and orientation, and an instrumentation strategy for freehand imaging was demonstrated in [127]. For our case, the UR3 would be the operator.

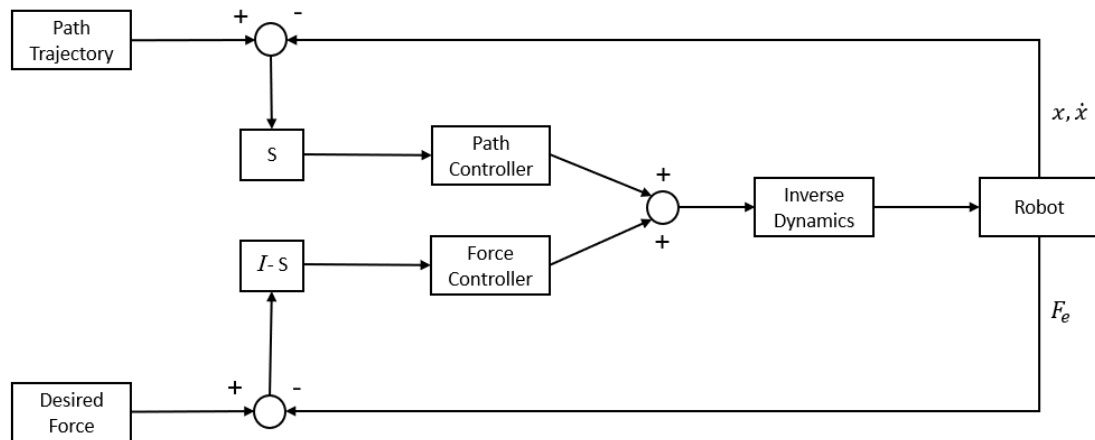


Figure 37: Hybrid control architecture.

The impedance control and compliance motion of the robot arm should be discussed. The compliance motion refers to the task of the robot arm's end effector is continuously contacting an environmental surface or object. The trajectory of the end-effector is modified by the occurring contact force, such as the task of pegging, opening a door, painting, etc. The compliance motion can be categorized as active compliance and soft compliance. As described in [128], for the active compliance, the control system is programmed to react to the contact force with the force sensor feedback, or the contact force can modify the trajectory of the end effector because of passive compliance. And it can also be further categorized by the stiffness of the contact surface or object. In

this sector, we are mainly focusing on active compliance motion. Many force control algorithms have been proposed for the robotics manipulators, and most of these approaches can be concluded as impedance control and hybrid control. The impedance control is more as an approach for the force control. For the robot arm, the impedance control does not directly control the force or tracking a force trajectory. It regulates the force by adjusting the relationship between velocity and force, or position and force. However, hybrid control is a position/force control scheme, which designed the control law for both position and force. With the concept of hybrid control, the parallel approach control law was proposed in [129], and adaptive approach was presented in [130], on-line learning and neural network learning control algorithm was demonstrated in [131, 132]. There is another common control structure called Inner/outer loop control that was introduced in [133]. The control law for the inner loop is nonlinear feedback linearization or inverse dynamics control as presented in [134], and the outer loop is an additional control law to achieve the objective of tracking, disturbance rejection, and robustness. Our study utilized a similar approach as [133], and the control architecture is shown in Fig. 37. As shown in Fig. 37, the x and \dot{x} are the robot positioning and velocity states, F_e is the force feedback measured by the force sensor. In our case, the ROBOTIQ force-torque sensor FT300 amounted to the end effector of UR3. The path and force controller was implemented by the PI and PD controller to simplify the control law for feasibility studies. The S is the selection matrix defined as a diagonal matrix, corresponding to the degree of freedom of the end effector in the compliance frame and position control. I is an identity matrix, and $I - S$ is to select the degree of freedom for force control. The force is mainly along the z -axis in our studies, and the end effector motion is mainly along x and y -axis. So, the selection S is defined as

$$S = \begin{bmatrix} 1 & 0 & 0 \\ 0 & 1 & 0 \\ 0 & 0 & 0 \end{bmatrix}. \quad (91)$$

4.2.3 Preliminary Results of Hybrid Control

The preliminary studies on hybrid control were performed with ROS and MATLAB to verify the communication between ROS and MATLAB, and the probe was moving against a hard copy book.

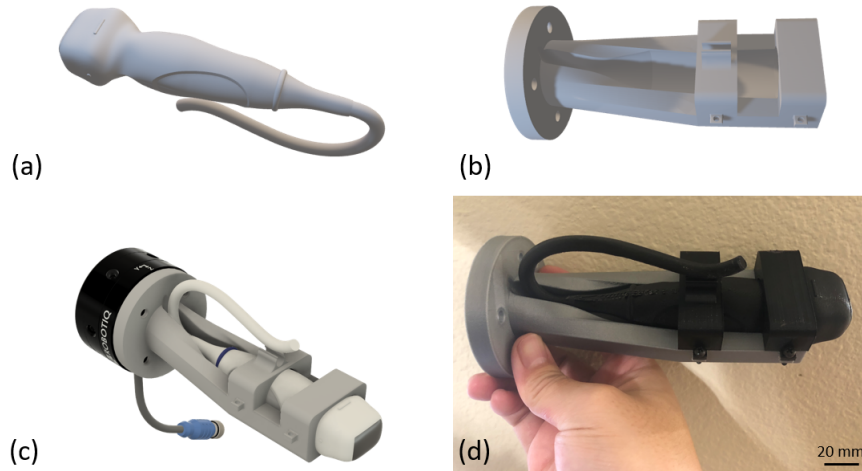


Figure 38: Schematics of ultrasound prob holder and fake model.

There were two computers connected with Ethernet cable through a router. The ROS and MATLAB setup and programming scripts can be found in [135]. The ROS works under Linux system, and serve as the ROS master, the MATLAB and ROS communicated with each other through IP address. For the ROS side, the force vector's messages, end effector position information, and other control flags were published through publishers and subscribed by the MATLAB side. The functions such as pose initialization, docking (approach to the target at 3 mm/sec until the contact happened) were programmed in ROS. The trajectories of the end effect while executing such functions can be monitored from the MATLAB side. The desired circle trajectory was predefined in MATLAB. After the control input was computed based on the hybrid control law discussed above, the end effector's current position, and the leading point, the control input was sent back to the ROS side. Finally, the arm was driven by the Universal Robot driver according to the control input. For the safety consideration, the preliminary studies were performed with the fake probe. The fake probe is 3D modeled as the real ultrasound probe shown as Fig. 38 (a), and the probe holder is shown as Fig. 38 (b). The schematic of the assembled holder, probe, and FT300 is presented as Fig. 38 (c). Finally, the 3D printed fake probe and holder is shown as Fig. 38 (d) and attached to the end effector of UR3. The results of preliminary studies are presented in Fig. 39. As shown in Fig. 39 (a), the desired trajectory was defined as a circle, the trajectory of the end effector was code in color by time. The ramp pattern between predefined circle trajectory and colored circle trajectory of the end effector is

the trajectory of adaptive process of docking. The adapted predefined circle trajectory is overlapped by the color tracking trajectory of the end effector. The contact force between the fake probe and hard surface is shown in Fig. 39 (b), the desired force set as -5 N . The big dip at the beginning is the first contact of the docking process. During the tracking process, the force is shown as the middle part, and the contact force of idle status is the following. Because of the friction and noise in force data, the force trend is smoothed and shown as the red line around $-5 \pm 1.5\text{ N}$ and the final force of idle statue is -5.6 N . The bump in the inactive status is artificially caused to demonstrate that the force control can be affected by an unstable base of the robot or target.

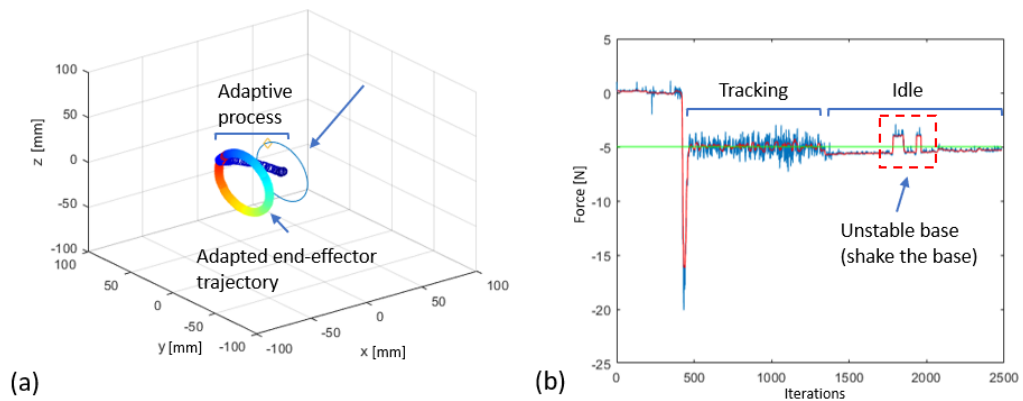


Figure 39: Preliminary results of hybrid control: (a) shows the docking and tracking process, (b) presents the force recorded during the tracking.

4.3 Ultrasound Image Detection

Besides the control algorithm and robot arm, the most important component is the imaging processing for swimmer detection. In this section, we would like to discuss several challenges, such as dynamic background, denoising, and moving object detection. The proposed method works for real-time ultrasound detection, which has a strict requirement on the processing speed. In this section, we only discuss the conventional imaging processing and object detection using the OpenCV library rather than other advanced techniques like the concept of deep learning, machine learning, or other popular neural networks such as Resnet50, YOLO, etc. The OpenCV is an open-source computer vision API, which includes more than 2500 functions and algorithms from the classics to the most recent state-of-art. And this library is suitable for Python, C++, Java, and other programming

languages. The proposed imaging process is mainly programmed in Python and includes threshold image, color conversion, logistic operation, and morphological transformation.

4.3.1 Ultrasound Programming

Our ultrasound detection study used the Verasonics 32 LE ultrasound system with a 64-element phased array transducer. The system is majorly designed as a flexible programmable tool for transmitting, receiving, and processing studies programmed by MATLAB. The system hardware structure will not be presented in this section, but the MATLAB program will be reviewed. The program of Verasonics is called a sequence program, and we assume the reader is familiar with MATLAB. The MATLAB is installed on the Verasoncis host computer, and the host computer is connected to the Vantage Unit(Ultrasound hardware) via PCI express cable. The ultrasound imaging process is programmed in event sequence as follows: (i) Transmit an unfocused burst of ultrasound and emit a plane wave that propagates over the transducer's field of view. (ii) Acquire the RF receive data for all receive channels from the transmit event. (iii) Transfer these data to the host computer. (iv) Stop sequence and return control to Matlab. The program consists of a defining system parameter, attributes, and sequence of hardware and software events. All parameters are defined in a setup script with MATLAB structures. The setup script is then run and saved as a .mat file. To run the program, the user should direct to the vantage directory and run the command "activate" in MATLAB to active the vantage system, then type VSX (Verasonics Script eXecution) to run the desired program with the name of the .mat file. VSX then parses the predefined MATLAB structures, adds any missing attributes needed to program the system, loads the sequence into the software and hardware sequencers, and tells the sequencers to run.

```
1 clear all
2 P.iter = 1;
3 P.startDepth = 5;
4 P.endDepth = 160; % Acquisition depth in wavelengths
5 P.record = 0;
6 % Define system parameters.
7 Resource.Parameters.speedOfSound = 1540;
8 Resource.Parameters.speedCorrectionFactor = 1.0;
```

```

9 Resource.Parameters.verbose = 2;
10 Resource.Parameters.initializeOnly = 0;
11 Resource.Parameters.simulateMode = 0;
12 % Resource.Parameters.simulateMode = 1 forces simulate mode, even if hardware
    is present.
13 % Resource.Parameters.simulateMode = 2 stops sequence and processes RcvData
    continuously.
14 Resource.System.SoftwareVersion = [4 0 0]; % Minimum software release for this
    script.
15 Resource.System.UTA = '260-MUX'; % This script requires the 260-MUX UTA.
16 % Specify Resources.
17 Resource.RcvBuffer(1).datatype = 'int16';
18 Resource.RcvBuffer(1).rowsPerFrame = 2*4096; % two acquisitions per frame
19 Resource.RcvBuffer(1).colsPerFrame = Trans.numelements;
20 Resource.RcvBuffer(1).numFrames = 100; % 100 frames used for RF cineloop.
21 Resource.InterBuffer(1).numFrames = 1; % one intermediate buffer used.
22 Resource.ImageBuffer(1).numFrames = 10;
23 Resource.DisplayWindow(1).Title = 'P4-2vFlash_32LE';
24 Resource.DisplayWindow(1).pdelta = 0.35;
25 ScrnSize = get(0,'ScreenSize');
26 DwWidth = ceil(PData(1).Size(2)*PData(1).PDelta(1)/Resource.DisplayWindow(1).
    pdelta);
27 DwHeight = ceil(PData(1).Size(1)*PData(1).PDelta(3)/Resource.DisplayWindow(1).
    pdelta);
28 Resource.DisplayWindow(1).Position = [250, (ScrnSize(4)-(DwHeight+150))/2, ...
    % lower left corner position
29 DwWidth, DwHeight];
30 Resource.DisplayWindow(1).ReferencePt = [PData(1).Origin(1),0,PData(1).Origin
    (3)]; % 2D imaging is in the X,Z plane
31 Resource.DisplayWindow(1).Type = 'Verasonics';
32 Resource.DisplayWindow(1).numFrames = 20;
33 Resource.DisplayWindow(1).AxesUnits = 'mm';
34 Resource.DisplayWindow.Colormap = gray(256);

```

Listing 1: Variables and Resource Structure

The P shown in the code present a global structure variable, $P.iter$ is define for numbering the saved images, $P.record$ is to control the image saving, $P.startDepth$ and $P.endDepth$ are to set the ultrasound detection range, which is in the unit of wavelengths. All the basics parameter and system version are set in $Resource$ structure, including the interface of MATLAB.

```

1  Trans.name = 'P4-2v';
2  Trans.units = 'wavelengths'; % Explicit declaration avoids warning message
   when selected by default
3  Trans = computeTrans(Trans);
4  Trans.maxHighVoltage = 50; % set maximum high voltage limit for pulser supply
   .
5  Trans = computeUTAMux64(Trans); % Add HVMux field for use with UTA 260-Mux

```

Listing 2: Transducer structure

This piece of the script is used to define the transducer's structure parameters; in our case, we use a P4-2v ultrasound transducer, and the maximum voltage is 50 V. The vantage function $computeUTAMux64$ computed the result of attributes. The attributes of transmit waveform (TW) and transmit action (TX) was defined as following.

```

1  % Specify Transmit waveform structure.
2  TW.type = 'parametric';
3  TW.Parameters = [Trans.frequency, .67, 2, 1];
4
5  % Set up transmit delays in TX structure.
6  TX.waveform = 1;
7  TX.Origin = [0,0,0]; % set origin to 0,0,0 for flat focus.
8  TX.focus = -P.radius; % set focus to negative for concave TX.Delay profile
   .
9  TX.Steer = [0,0];
10 TX.Apod = ones(1,Trans.numelements); % set TX.Apod for 64 elements
11 TX.aperture = 1;
12 TX.Delay = computeTXDelays(TX);

```

Listing 3: Transmit waveform and action structure

The second step of the sequence programming is to define the parameters for receiving echo signals from the plane wave transmit and store in local memory. The analog signal amplifiers on each receive channel should be programmed and specify how they are digitized, filtered, and stored. The receiver amplifier gain controlled by and defined as a TGC (Time Gain Control) waveform, which defines the receiver gain as a function of time from the transmit burst as following

```

1  % Specify TGC Waveform structure.
2  TGC.CntrlPts = [0,467,535,653,690,811,942,1023];
3  TGC.rangeMax = P.endDepth;
4  TGC.Waveform = computeTGCWaveform(TGC);

```

Listing 4: Time Gain Control(TGC)

The receive operation should be defined to specify other attributes of the input signal processing. The Receive structure sets the parameters, including how long the receive period should run, which is used for the TGC waveform, how to sample and filter the received data, and The buffer for storing the RF data.

```

1  % Specify Receive structure arrays.
2  maxAcqLength = ceil(sqrt(P.aperture^2 + P.endDepth^2 - 2*P.aperture*P.endDepth
   *cos(P.theta-pi/2)) - P.startDepth);
3  Receive = repmat(struct('Apod', [zeros(1,16),ones(1,32),zeros(1,16)], ...
4  'startDepth', P.startDepth, ...
5  'endDepth', P.startDepth + maxAcqLength, ...
6  'aperture', 1,...
7  'TGC', 1, ...
8  'bufnum', 1, ...
9  'framenum', 1, ...
10 'acqNum', 1, ...
11 'sampleMode', 'NS200BW', ...
12 'mode', 0, ...
13 'callMediaFunc',0),1,2*Resource.RcvBuffer(1).numFrames);
14 % - Set event specific Receive attributes.
15 for i = 1:Resource.RcvBuffer(1).numFrames
16 Receive(2*i-1).framenum = i;
17 Receive(2*i).framenum = i;

```

```

18 Receive(2*i).acqNum = 2;
19 Receive(2*i).Apod = [ones(1,16), zeros(1,32), ones(1,16)];
20 Receive(2*i).callMediaFunc = 1; %active simulated media movement
21 end

```

Listing 5: Recieve Structure

The *Recon* structure contains the parameters for constructing the ultrasound image, which specifies the buffer number to use, construction mode, etc. The -1 in the structure means to use the latest image buffer.

```

1 % Specify Recon structure arrays.
2 Recon = struct('senscutoff', 0.5, ...
3 'pdatanum', 1, ...
4 'rcvBufFrame', -1, ...
5 'IntBufDest', [1,1], ...
6 'ImgBufDest', [1,-1], ...
7 'RINums', 1:2);
8
9 % Define ReconInfo structures.
10 ReconInfo(1) = struct('mode', 'replaceIQ', ...
11 'txnum', 1, ...
12 'rcvnum', 1, ...
13 'regionnum', 1);
14 ReconInfo(2) = struct('mode', 'accumIQ_replaceIntensity', ...
15 'txnum', 1, ...
16 'rcvnum', 2, ...
17 'regionnum', 1);

```

Listing 6: Reconstruction Structure

A series of processes are defined, including Receive, TX, Recon, SeqControl, in the process structure array. And a single sequence specification is defined as the event in a for-loop to specify all operations' order. Finally, the acquisition data was transferred from local memory on the Acquisition Modules to the RcvBuffer in the MATLAB.

```

1 % Specify Process structure array.

```

```

2  pers = 20;
3  Process(1).classname = 'Image';
4  Process(1).method = 'imageDisplay';
5  Process(1).Parameters = {'imgbufnum',1,... % number of buffer to process.
6  'framenum',-1,... % (-1 => lastFrame)
7  'pdatanum',1,... % number of PData structure to use
8  'pgain',1.0,... % pgain is image processing gain
9  'reject',3,... % reject level 50
10 'persistMethod','simple',...
11 'persistLevel',pers,...
12 'interpMethod','4pt',...
13 'grainRemoval','none',...
14 'processMethod','none',...
15 'averageMethod','none',...
16 'compressMethod','power',...
17 'compressFactor',100,...
18 'mappingMethod','full',...
19 'display',1,... % display image after processing
20 'displayWindow',1};
21
22 Process(2).classname = 'External';
23 Process(2).method = 'myProcFunction';
24 Process(2).Parameters = {'srcbuffer','image',...
25 'srcbufnum',1,...
26 'srcframenum',-1,...
27 'dstbuffer','none'};
28
29 % Specify SeqControl structure arrays. Missing fields are set to NULL.
30 SeqControl(1).command = 'jump'; % - Jump back to start.
31 SeqControl(1).argument = 1;
32 SeqControl(2).command = 'timeToNextAcq'; % set time between acquisitions
33 SeqControl(2).argument = 1000; % 1msec
34 SeqControl(3).command = 'timeToNextAcq'; % set time between frames
35 SeqControl(3).argument = 9000; % 10msec total frame interval (~100fps)
36 SeqControl(4).command = 'returnToMatlab';

```

```
37 nsc = 5; % nsc is count of SeqControl objects
```

Listing 7: Process Structure

```
1 % Acquire all frames defined in RcvBuffer
2 for i = 1:Resource.RcvBuffer(1).numFrames
3     Event(n).info = 'center of receive aperture';
4     Event(n).tx = 1;
5     Event(n).rcv = 2*i-1;
6     Event(n).recon = 0;
7     Event(n).process = 0;
8     Event(n).seqControl = 2; % acquisition PRI
9     n = n+1;
10
11     Event(n).info = 'edges of receive aperture';
12     Event(n).tx = 1;
13     Event(n).rcv = 2*i;
14     Event(n).recon = 0;
15     Event(n).process = 0;
16     Event(n).seqControl = [3,nsc];
17     SeqControl(nsc).command = 'transferToHost';
18     nsc = nsc + 1;
19     n = n+1;
20
21     Event(n).info = 'Reconstruct';
22     Event(n).tx = 0;
23     Event(n).rcv = 0;
24     Event(n).recon = 1;
25     Event(n).process = 1;
26     Event(n).seqControl = 0;
27     n = n+1;
28
29     Event(n).info = 'Call external Processing function';
30     Event(n).tx = 0;
31     Event(n).rcv = 0;
32     Event(n).recon = 0;
```

```

33     Event(n).process = 2;
34     Event(n).SeqControl = 0;
35     if floor(i/3) == i/3      % Exit to Matlab every 3rd frame
36     Event(n).seqControl = 4;
37     end
38     n = n + 1;
39 end
40
41 Event(n).info = 'Jump back to first event';
42 Event(n).tx = 0;
43 Event(n).rcv = 0;
44 Event(n).recon = 0;
45 Event(n).process = 0;
46 Event(n).seqControl = 1;

```

Listing 8: Event Sequence Specification

```

1  UI(3).Control = {'UserB2','Style','VsSlider','Label','Record',...
2  'SliderMinMaxVal',[0,1,0],'SliderStep',[1,1],'ValueFormat','%3.0f'};
3  UI(3).Callback = text2cell('%RecordCallback');
4
5  %RecordCallback
6  P = evalin('base','P');
7  P.record = UIValue;
8  assignin('base','P',P);
9  %RecordCallback

```

Listing 9: GUI and Callback Function

One additional GUI was define at *userB2* location with a *VsSlider*. This GUI slider is used to control the process of saving the ultrasound images. And the value of *P.record* was changed accordingly in its callback function. The callback functions are identified and enclosed by the symbol *% + name*.

```

1  %EF#1
2  myProcFunction(RData)
3  persistent myHandle

```

```

4  P = evalin('base','P');
5  gray_img = mat2gray(RData);
6  gray_img = imresize(gray_img, [500 NaN]);
7  if P.record
8      imwrite(gray_img, [pwd '/Verasonics_Haoran/Images/Scene/scene', num2str(P.
9          iter), '.png']);
10     imwrite(gray_img, [pwd '/Verasonics_Haoran/Images/scenel.png']);
11     P.iter = P.iter+1;
12     assignin('base','P', P);
13 end
14 %EF#1

```

Listing 10: External Function

The External process is defined in the process structure array, set to extract the latest frame buffer. In the external callback function shown above, the latest frame buffer is converted from the mat file to a gray-scale image, reshaped to a 500-pixel height frame. The if statement is controlled by *P.record*, and there are two *imwrite* inside it. One *imwrite* is used to save all the latest frames as individual images for future studies. Another one is keeping overwriting on the same image to reduce the transmission between MATLAB and ROS, instead of searching all the frames and finding the latest one. Such a process is that the script for the communication between MATLAB and ROS can not be added to the ultrasound setup script. And when the MATLAB executes the ultrasound script, the communication script can not be run as a multi-thread or other CPU core. However, taking advantage of a multi-core computer, the communication script is run in another MATLAB session. Moreover, there is no official way to share the variables between the workspace of two sessions. To fix this problem, we used the external function to save the frames to the directory during the scanning and used another script to grab the latest frames and transmit to ROS. Although this method is not elegant, and sometimes the latest frame can not be grabbed because the *imwrite* function is not completed, the high FPS (about 100 to 110FPS) compensated for this issue.

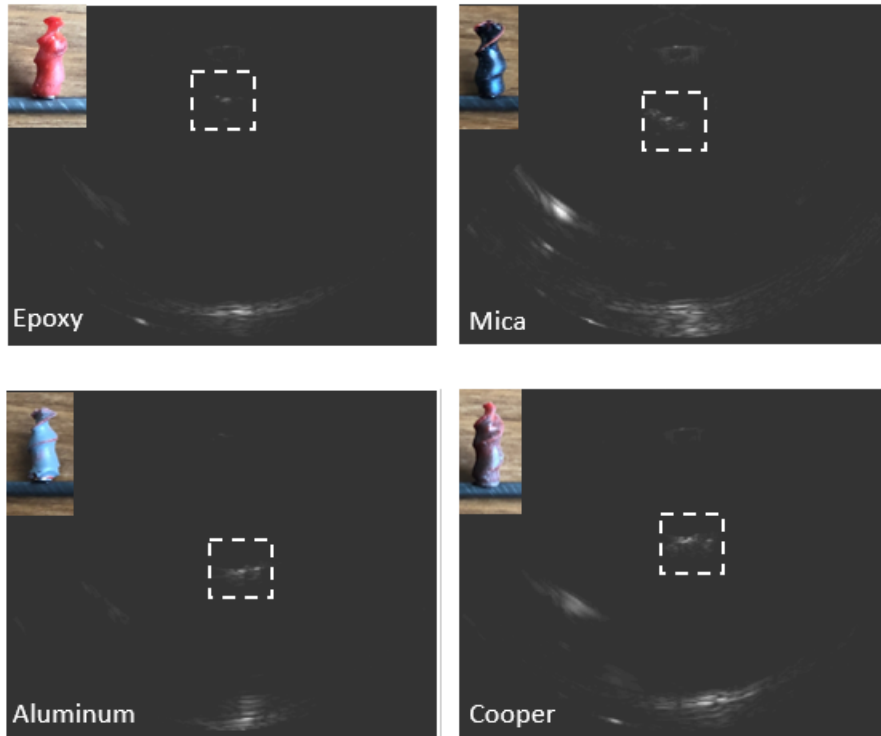


Figure 40: Echogenicity results of the metal coating.

4.3.2 Swimmer Detection

After saving, grab, and sending the latest frame from MATLAB to ROS, there is only one step missing: the swimmer detection. Due to our magnetic swimmer's size and echogenicity, which has the same design as 2.0 Swimmer. It can not be detected by ultrasound in static, because the reflected wave is too weak to be detected. However, we found that the metal material generally possesses a higher echogenicity, so a metal powder layer was coated on the swimmer to validate our hypothesis. The coating was manually coated for the preliminary tests with epoxy resin and metal powder mixture on two times upscaled design. The coating thickness may varied case to case. The results are shown in Fig. 40. As the results showed, the swimmer can be slightly seen when coated with the epoxy resin layer because of the inserted magnetic size. In this study, mica, aluminum, and copper have been used because they the most common commercially available powder on the market. The mica is slightly better than an epoxy layer. However, aluminum and copper can be well seen. So the metal powder can improve the echogenicity and visibility of our swimmer in the ultrasound image. So the final version of our swimmer 2.0 is coated with nichrome on one side.

For the swimmer detection study, the swimmer was put into a PMDS cube model with a 3 mm diameter water-filled channel. The PDMS model was placed in the middle of our magnetic manipulator's workspace. The swimmer is open-loop control to iteratively go forward from one side to another side then go backward. For the flash mode detection of ultrasound, which transmits a flat

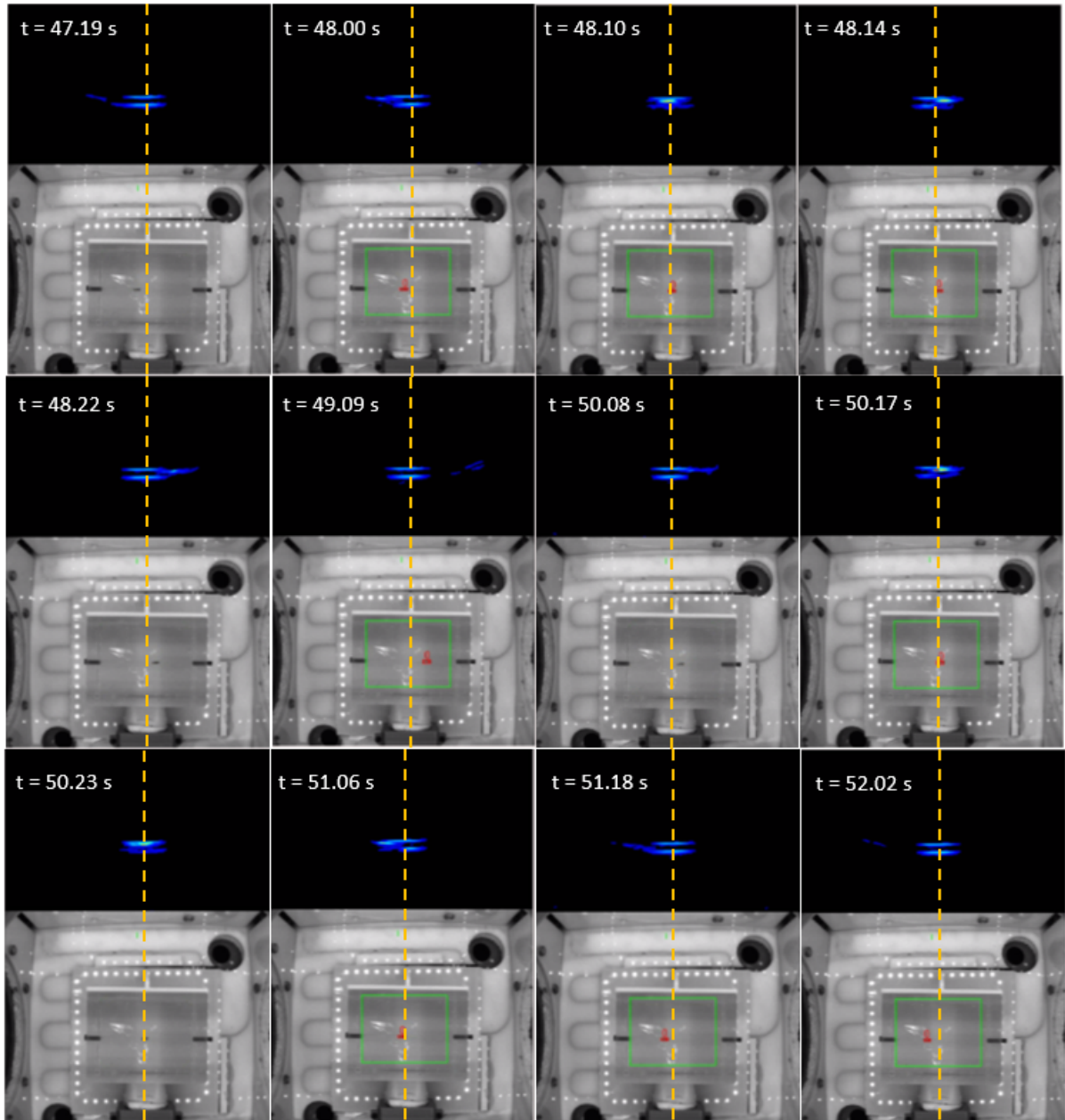


Figure 41: Ground truth study: The sequence images presented the Doppler detection results, which is aligned with the central axis of the ultrasound transducer.

wave, the ultrasound image is on a gray-scale. Because of the poor quality of this mode, the swimmer is detected with a long comet-tail due to the high echogenicity of the metal. Other detection modes can be chosen, the only reason to use this mode is that it has the highest PFS, about 110 FPS, compared to others, about 30 FPS. It is necessary for the transmission between MATLAB and ROS, considering frame losses. Because of the low quality, a method or an approximation should be proposed for the detection. So we record the video of the swimmer and save the ultrasound frames using Doppler mode. The Doppler mode can detect the object's velocity and the water flow, then code it with color. The ultrasound frame was converted as a video. The swimmer started and stopped simultaneously in both videos with the resolution of 0.01 ms. Then, the video is edited at the same duration as the video recorded by the camera. The results are shown in Fig. 41. The snapshots are shown in Fig. 41 were aligned between the central line of the ultrasound frames and the central line of the ultrasound probe. The time of this series of the snapshot was shown on the left corner. From the images, the swimmer and the walls of 1D channel is distinguished from the background. So we can conclude that the swimmer can be approximated at the moving shadow center. This assumption is used for later studies.

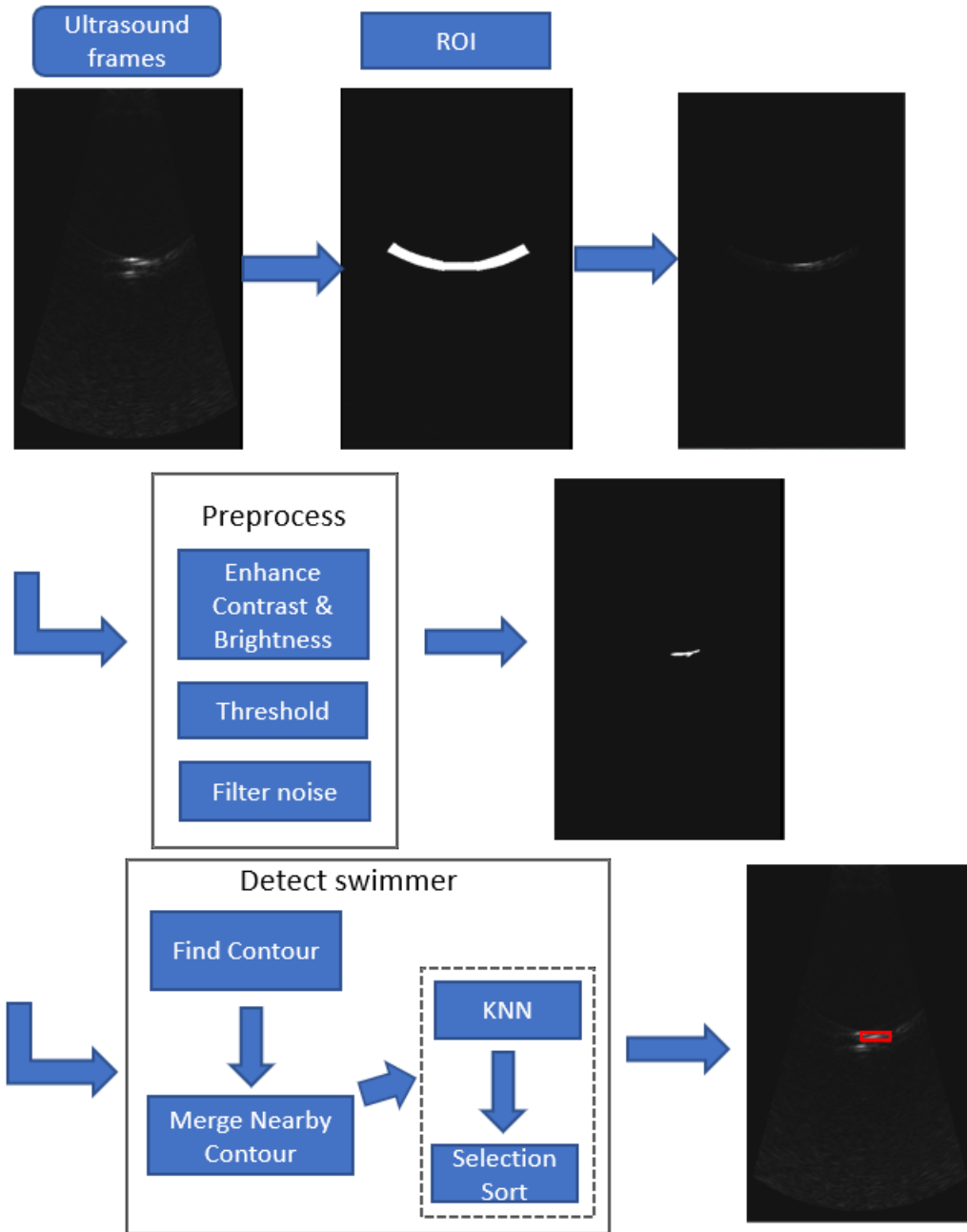


Figure 42: Detection diagram.

The detection algorithm is mainly programmed in Python using OpenCV and integrated as a topic in ROS. the diagram of the detection is shown as Fig. 42. After getting the read the latest frame at the ROS side, the frame is passed to the *contrast_brightness* function to adjust the pixel values, and the function is shown as following

```
1 def contrast_brightness(cur_frame_gray, alpha, beta):
```

```

2  new_image = cur_frame_gray.copy()
3  m, n = new_image.shape
4  new_image[:, :] = np.clip(np.ones([1, n]) * alpha * cur_frame_gray + np.ones
    ([1, n])*beta, 0, 255)
5  return new_image

```

The new image was converted as a binary image and applied with the ROI mask shown in Fig. 42. Because of the speckle and echo overlapping, there are white dots in the ultrasound frames. This noise was removed by OpenCV *findContours* function, and the white dots were filled as background according to the size. All describe steps are programmed in the *preprocess* function.

```

1  def preprocess(img, alpha=2, beta=-50):
2      img = contrast_brightness(img, alpha, beta)
3      _, img = cv2.threshold(img, 30, 255, cv2.THRESH_BINARY)
4      contours, _ = cv2.findContours(img, cv2.RETR_TREE, cv2.CHAIN_APPROX_SIMPLE)
5
6      for c in contours:
7          area = cv2.contourArea(c)
8
9          # Fill very small contours with zero (erase small contours).
10         if area < 30 or area > 2500:
11             cv2.fillPoly(img, pts=[c], color=0)
12             continue
13     return img

```

The new image after preprocess was passed to the *find'contour* function. In this function, we implemented two functions to localize the swimmer. The first functions are programmed, referring to the concept of K nearest neighbor(KNN). Even after the denoise process, there are still multi-contour boxes that appear around the swimmer position. These contours are produced by the high echogenicity of the metal powder. So to compensate for the effect, we implemented the concept of KNN to categorize and merge the nearby contour. The sorting algorithm, selection sorting, was then implemented to refine the merging. Finally, the swimmer's contour box was plotted on the frames, and the center of the contour was passed the control algorithm for the closed-loop control. The whole *find'contour* function is shown as following.

```

1  def find_contour(img):
2  contours, _ = cv2.findContours(img, cv2.RETR_EXTERNAL, cv2.CHAIN_APPROX_SIMPLE
   )
3  # merge nearby contour -->k nearest neighbour
4  contoursRect = []
5  for c in contours:
6  [x, y, w, h] = cv2.boundingRect(c)
7  if not contoursRect:
8  contoursRect.append((x, y, w, h))
9  else:
10 index = -1
11 mind = float('inf')
12 # find the closest contour landmark in contoursRect
13 for i, dims in enumerate(contoursRect):
14 [xr, yr, wr, hr] = dims
15 dist = np.sqrt((x + w / 2 - xr - wr / 2) ** 2 + (y + h / 2 - yr - hr / 2) **
   2)
16 if dist < mind and dist < 50:
17 mind = dist
18 index = i
19
20 if index == -1:
21 contoursRect.append((x, y, w, h))
22 else:
23 # merge the closest contour
24 arr = []
25 [xr, yr, wr, hr] = contoursRect[index]
26 arr.append((xr, yr))
27 arr.append((xr + wr, yr + hr))
28 arr.append((x, y))
29 arr.append((x + w, y + h))
30 x, y, w, h = cv2.boundingRect(np.asarray(arr))
31 contoursRect[index] = (x, y, w, h)
32
33 n = len(contoursRect)

```

```

34 i = 0
35 while i < n:
36     # refine contour landmarks and merge close contour (selection sort)
37     [x, y, w, h] = contoursRect[i]
38     index = -1
39     mind = float('inf')
40     if i + 1 < n:
41         for j in range(i + 1, n):
42             [xr, yr, wr, hr] = contoursRect[j]
43             dist = np.sqrt((x + w / 2 - xr - wr / 2) ** 2 + (y + h / 2 - yr - hr / 2) **
44                 2)
45             if dist < mind and dist < 50:
46                 mind = dist
47                 index = j
48             if index == -1:
49                 i += 1
50                 continue
51             else:
52                 arr = []
53                 [xr, yr, wr, hr] = contoursRect[index]
54                 arr.append((xr, yr))
55                 arr.append((xr + wr, yr + hr))
56                 arr.append((x, y))
57                 arr.append((x + w, y + h))
58                 x, y, w, h = cv2.boundingRect(np.asarray(arr))
59                 contoursRect[i] = (x, y, w, h)
60                 del contoursRect[index]
61                 n -= 1
62                 i += 1
63     return contoursRect

```

4.4 Experimental Studies

4.4.1 Experimental Setup

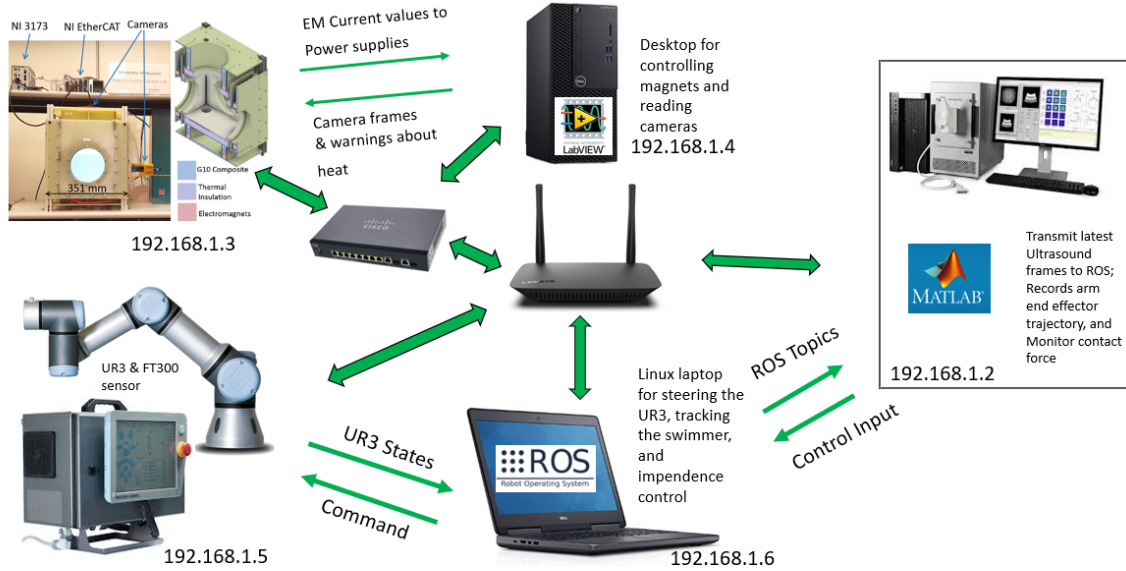


Figure 43: System network.

The final system for the ultrasound and UR3 studies consists of a LabVIEW PC, a Matlab PC, a ROS PC, a magnetic manipulator, a UR3, and an ultrasound, as shown in Fig. 43. All individuals were connected by a TP-link router, which has four ethernet ports. The cisco sg300-10mp ethernet switch was employed to connect the NI industrial controller and Labview PC to the router. Five different IP addresses were assigned to each component, which is shown at the bottom of each component in Fig. 43. The Matlab PC is mainly used to reconstruct ultrasound images, transmit the latest ultrasound frames to ROS PC, and record and monitor the end-effector trajectory and contact force. The ROS PC runs under the Linux system, mainly used to steer the UR3, track the swimmer, transmit robot arm status to Labview PC and Matlab PC, and implement control algorithms. The Labview PC is utilized to perform inverse magnetics calculation, monitor, and control our lab-built magnetic system.

As Fig 44 shown, the Ultrasound PC runs two Matlab sessions simultaneously. The first one generates and saves the latest frame to the desired directory, and the second session grabs the newest frame and transmits it to ROS PC through the local network. While the Matlab session runs the

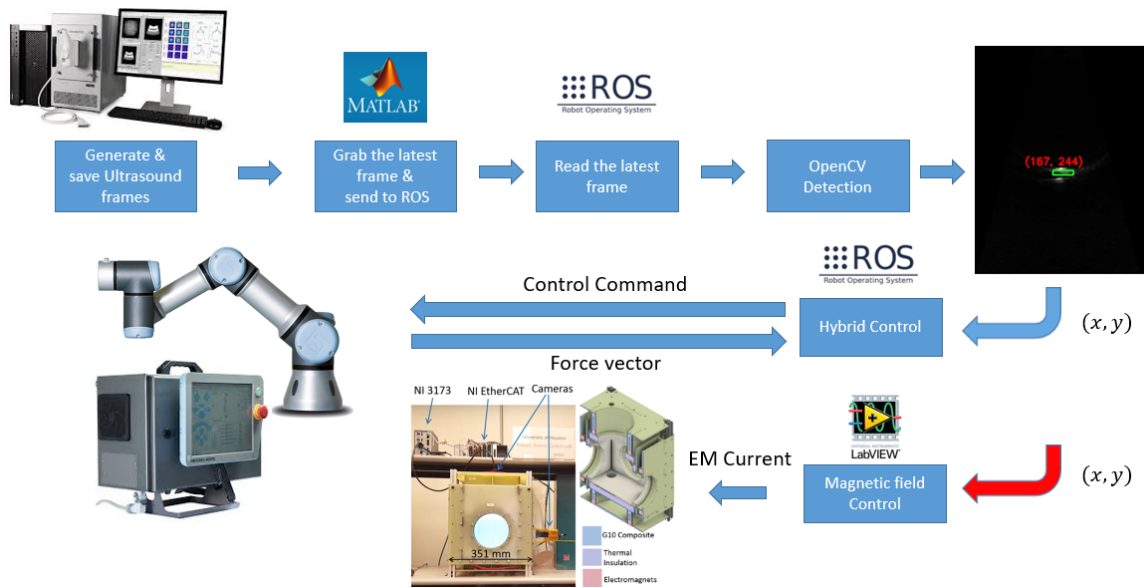


Figure 44: Flow diagram of the system.

ultrasound script, other scripts can not be executed in other threads. And the ROS and Matlab connections can not be added to the ultrasound script. By taking advantage of the multi-core PC, the second MATLAB session is opened and run for the data transmission. After ROS PC read the latest frame, the frame is sent to the ROS swimmer detection node, and the pixel coordinate of the swimmer position is sent to the ROS control node. The conversion ratio between a pixel and the physical world is 0.283 mm/pixel. The FT sensor's contact force is read by TCP/IP between ROS PC and UR3 control box. The force data is transmitted to the ROS control node for the hybrid control. The control command is then sent back to UR3 at the rate of 80 Hz. There is no subvi or module in Labview is developed for the communication between ROS and Labview, so the TCP/IP was used to exchange data. The end-effector coordinates (x, y, z) , and the swimmer pixel coordinate were encoded into a string and send to LabVIEW by TCP/IP socket programmed in Python, which is shown as the red arrow in Fig. 44. The reason for the red arrow is that currently, the data exchange process between ROS and Labview has been developed, but it was not implemented in 1D tracking experiments. This function will be implemented into 2D and 3D tracking in future work.

As presented in Section 3.2, the front panel of the magnetic manipulator was replaced by a new design. The new design has the same dimension except for the diameter of the opening hole in the center. The diameter of the opening hole in the previous design is 150 mm, and the diameter of the

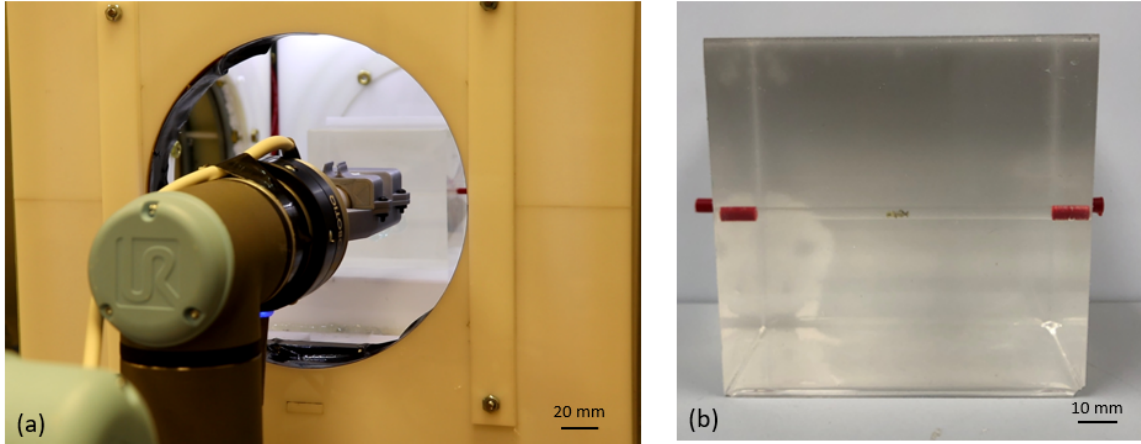


Figure 45: Hardware setup for 1D tracking study.

opening hole in the new design is 180 mm. The purpose of the replacement is to enlarge the move space of the transducer carried by UR3. The new front panel of the magnetic manipulator is shown as Fig. 45 (a). The human vasculature is mimic by the PDMS channel. The making process is as same as the procedure presented in Section 3.6.2. The PDMS mode was cured in a cube container made by an acrylic sheet and laser cutter, and a rod was inserted in the container to form the 1D channel. After the PDMS mode is cured, the rod was removed, and the 1D channel is formed and showed in Fig. 45 (b). The PDMS was placed on a based, and the base is glued on the workspace bottom of the magnetic manipulator.

4.4.2 Swimmer Detection Implementation

The swimmer detection studies and OpenCV process were proposed in Section 4.3.2. The imaging process presented in Section 4.3.2 was performed based on the saved ultrasound frames, which is not performed in real-time. In this section, we will demonstrate the workflow and results of the detection implementation. As shown in Fig. 46, on the left shows the detection process. It's the same process as illustrated in the previous section. However, it was performed after all individual components connected as a whole system by the local network. The ultrasound transducer is carried by the UR3 and pressed against the PDMS model. The docking process was performed. The transducer center and the 1D channel is manually aligned at the same height by controlling the UR3 with a joystick. The snapshots of the swimmer images of ROS, ultrasound, and Labview PC were

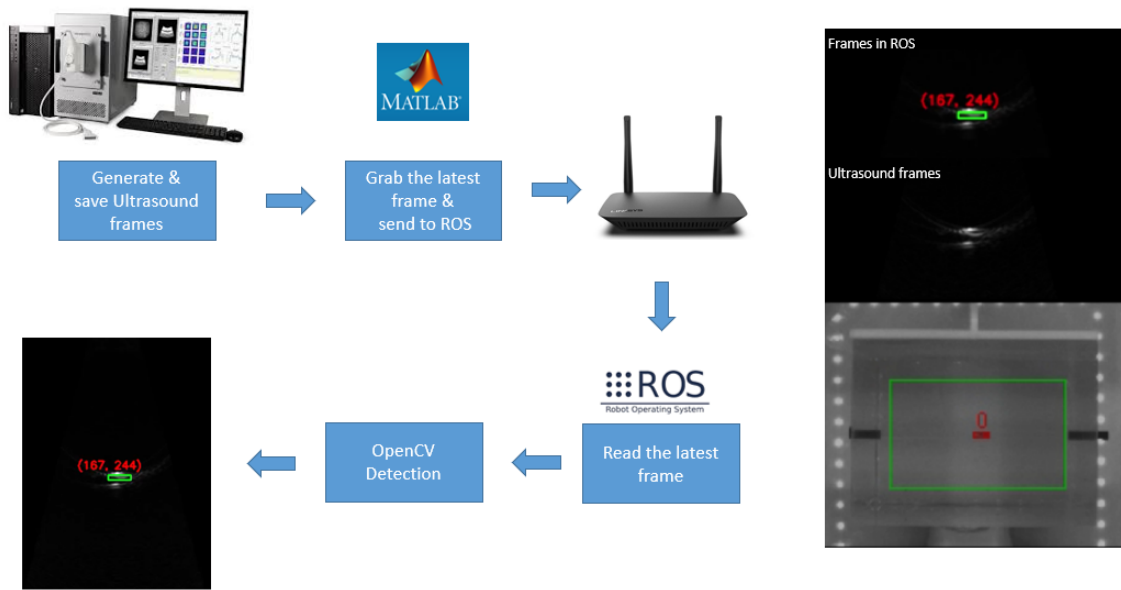


Figure 46: The flow diagram of the swimmer detection.

presented on the right of Fig. 46.

4.4.3 1D Tracking Studies

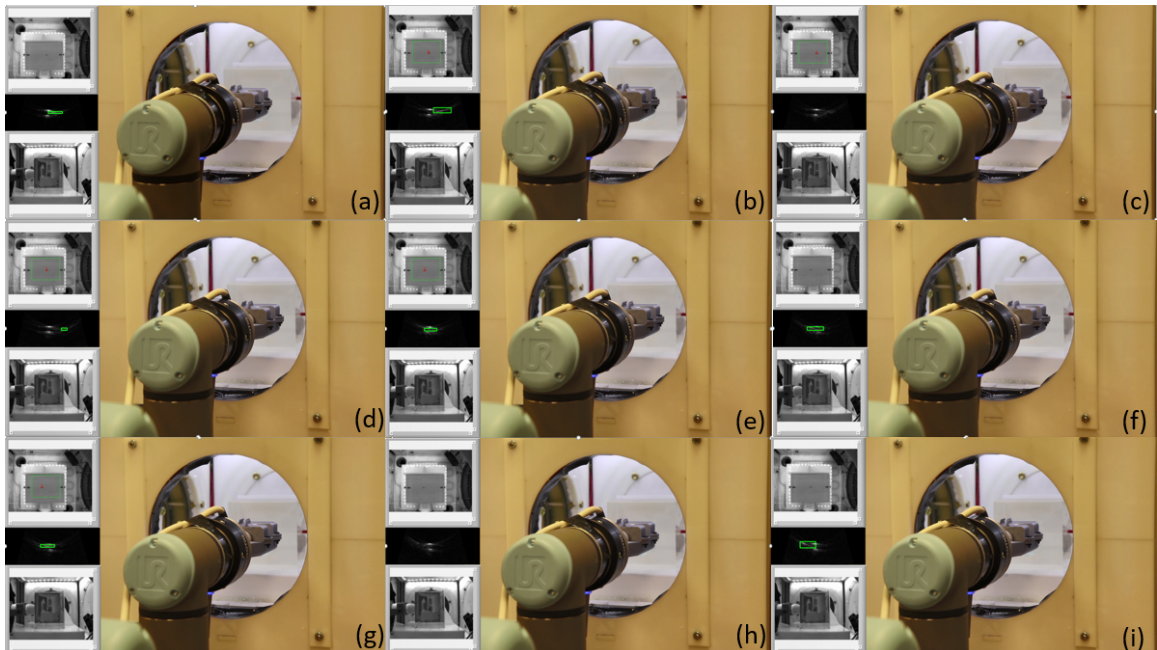


Figure 47: Sequence images of 1D tracking.

1D tracking studies are discussed in this section. The flux density of the magnetic field is 0.002

T. The swimmer was programmed to move back and forward in the 1D PDMS channel at 8Hz, and the moving length is 15 mm. The open-loop control was implemented and programmed in Labview because the swimmer moves in a constrained channel. And the vision detection from the camera was used to flip the motion direction while it reaches the boundary. The hybrid control algorithm was implemented to perform tracking and pressing. The snapshots of the tracking process are shown in Fig. 47 (a)-(i). The swimmer started from the center of the workspace, move to the right, then go back to the left. When the swimmer is not detected in the ultrasound frames, the robot arm will stop moving, such as Fig. 47 (c) and (g). The swimmer can be almost detected all the time while developing the OpenCV algorithm because the saved images were used. For the practical implementation, the ultrasound images were saved, grabbed, and sent to ROS in real-time. The ultrasound frame was overwritten on the same image file during the process, and the sequential images were saved in another folder for later analysis process. The average transmission speed can be significantly improved from 2s to 0.02s comparing to save the sequential frames and find the latest images. The desired contact force was set as 6 N. The impedance control failed during the implementation. The reasons are the following: (1) The contact between transducer and PDMS is soft-contact. (2) The base of the robot arm is unstable. (3) The PID controller is too simple to handle the complex situation. (4) The force sensor data is too noisy and has a drifting data problem. Although a low pass filter was implemented, it could not solve the problem.

5 Conclusion and Future work

5.1 Conclusion

The first part of this dissertation proposed a new force transmission technique called solid media transmission and mechanism compatible manipulators. These MR compatible mechanisms and manipulators are the main theme in interventional MRI, and pioneering groundbreaking works have advanced this concept to reality. Efforts are continuing toward new actuation and robot designs for eventual clinical use. SMT was introduced as a simple and low-cost transmission exhibiting certain features similar to fluidic systems for MR manipulation: conduit routing and remote transfer of actuation. The data presented herein illustrated that closed-loop SMT can achieve sub-millimeter accuracy yet underscored the main limitations that need to be addressed: friction and media packing to ensure the SMT backbone performs theoretically expected. The presented studies had certain restrictions. First, the friction model is a qualitative analysis that neglects COF differences and other physical characteristics, which can be solved using FEA software such as ANSYS and COMSOL. Second, benchtop studies were limited to 1 meter long SMT tubing. While we resulted in a valuable understanding of the mechanism, we plan to systematically characterize SMT performance after implementing a low-friction SMT version. It is noted that MR studies were performed with 4-meter long SMT lines but with open-loop control because the effect on MR images was the subject, not control. Third, the choice of material was not optimal. Nylon tubing and spheres have a coefficient of friction of 0.25, while PTFE-to-PTFE is 0.04. Those studies underscored the importance of material considerations affecting the elasticity of the system. Fourth, manual media packing was not optimal, causing small gaps in the SMT backbone. Friction, suboptimal media packing, and tube elasticity may have contributed to the system's nonlinearity and the long rise time during closed-loop control. A mechanism to establish and maintain media packing is under development. In this work, MRI studies employed servo motors inside the MR scanner room by placing them outside the 5 Gauss line and using filtering and shielding to reduce EMI. Additional studies are needed to characterize the conditions for their use further, as well as further improve EMI reduction. SMT is a new mechanism and is not well investigated. In Section 2.4, we have explored this transmission

for actuating manipulators. The investigation and optimization of materials selection and SMT-specific manipulators have been presented. The data presented herein illustrated that closed-loop SMT can quickly and accurately respond to a reference signal. Additionally, the error for lengths from 1 to 4 m can be regulated within the resolution of a 0.05 mm optical encoder. From the system studies, we concluded that our one-DoF manipulator's experiment results verified the hypothesis of four primary factors (friction, length, expansion, and mechanical design) proposed in our previous work [46]. We also presented and analyzed an SMT-actuated two-DoF manipulator design and its closed-loop positioning control performance. Because of the high nonlinear characteristics presented in the experiment results, the system identification step is necessary. With a better-identified system, we can achieve better control results. Moreover, the mechanical design optimization of SMT-based manipulators can also be further investigated.

In the second part of this dissertation, the studies of controlling a milli-scale magnetic swimmer were presented. We reported a lab-build magnetic manipulator as an external magnetic input source, and the magnetics calculations were illustrated for the magnetic field control. In the preliminary studies of the magnetic swimmer, the spiral-typed design was proposed. The swimmers can travel through a tube with a diameter of 15 mm using a PI controller. A new design with a spiral tip and an orientation controller was proposed to improve the tracking performance. The experiments showed that millimeter-scale robots could navigate 3D paths with an average error of 2.3 mm. We found that the undesired gradient force existed during the experiments as the side effect of the magnetic field control. Thus, we propose an efficient online calculation to compensate for the undesired gradient force applied to the swimmer during 3D navigation. Although it only provided a modest result, it can still be implemented for extreme cases; for example, the swimmer is closed to the EM coil. Five thread-pitch values were experimentally investigated to evaluate the relationship between pitch and stability of the swimmer design. A swimmer with a 2.0 mm pitch had the best stability among all designs tested. A direct model reference adaptive controller (MRAC) was implemented further to improve the path-following accuracy of the 3D guidance. The comparison proves a higher performance of MRAC than the PI controller. The path-following mean error is 3.8 ± 1.8 mm, which is smaller than one body length of the swimmer (6 mm). The path-following performance

on a complex trajectory and forward & backward motion using MRAC were also performed and analyzed. The magnetic swimmer has a huge potential value for clinical application. As discussed before, one imaginable task that can be achieved by a magnetic swimmer is blood clot removal. As the in vivo studies shown in Section 3.6, the results showed that these magnetic robots could remove blood clots at rates of up to $20.13 \text{ mm}^3/\text{min}$, which is the first successful complete removal of clots in vitro by a magnetically-propelled tetherless robot. The removal rate is significantly higher than streptokinase (thrombolytic medication), which was reported to remove blood clots at a rate of $0.17 \text{ mm}^3/\text{s}$ in similar size channels [117]. As shown in Section 3.6.4, our miniature swimmer can navigate inside a tube having a diameter of 15 mm without touching the walls. The diameter is less than the diameter of the ascending aorta. Not touching the walls of the aorta would prevent plaque detachment or disturbances of the endothelium. Miniature swimmers could reduce infection risk and recovery time, improve patient outcomes and comfort, and provide treatment options for inoperable clots. Blood clot removal could be performed inside large vessels like the pulmonary arteries. Clots could also be removed in smaller vessels. Preventing the swimmer from touching the walls of small vessels is challenging. The swimmers presented in this dissertation have a diameter of 2.5 mm, and a length of 6 mm. This size could allow the swimmer's insertion within the bloodstream of a patient using conventional catheter insertion methods [136]. In our study, blood clots are removed from only slightly larger channels than the swimmer (3 mm diameter). Our experimental setup does not regulate the swimmer's radial position inside the channel during the clot removal. Therefore, the swimmer's sides do rub against the walls of the channel. The effect of this rubbing action on the endothelium is not investigated in the present paper. It should be noted that the damage to the vessels might be minimal because no significant force is applied by the swimmer in the radial direction (direction perpendicular to the vessel wall). Additionally, the abrasive coating is only present at the swimmer's tip and would, therefore, not be in contact with the artery walls during clot removal. As the last part of the magnetic swimmer studies, the ultrasound and UR3 were integrated into the existing system shown in Section 4. The local network connects the whole system through a router and an ethernet switch; the hybrid control was proposed to track and force control of the UR3 and ultrasound transducer; the UR3 dynamics and kinematics were discussed and implemented in

ROS. The Ultrasound scripts were illustrated, and an external function was programmed to save the frames in real-time. The algorithm of swimmer detection in an ultrasound frame was proposed and programmed using OpenCV. The ultrasound echogenicity was experimentally analyzed and demonstrated that the metal power could improve the swimmer ultrasound scanning's visibility and image quality. Finally, the hardware implementation was successfully performed by tracking the swimmer moving in a 1D channel. Although the impedance control failed, we still demonstrated the concept's feasibility to integrate the UR3 and ultrasound into our existing system.

5.2 Future Work

For gradient force compensation, one key component is the magnetization direction of the swimmer during movement. Due to the swimmer size and limited measure sensors, the swimmer's magnetization direction can not be directly obtained. Thus, in the previous discussion, the magnetization is approximately calculated by an orthogonal vector of the swimmer movement direction. Referring to the synchronous motor, there is a delay angle between the magnetization of the external magnetic field and the swimmer, from 0 to 90deg. Because the magnetic field rotates in the UV plane, the delay angle can be experimentally measured and modeled versus applied torque in the future to approximate the magnetization direction accurately.

Adding an L_1 adaptive controller could improve the path-following and navigation in a 3D environment. The L_1 adaptive controller can provide a wider stability margin and better disturbance rejection, as analyzed and discussed in [137]. The L_1 adaptive controller is an indirect model adaptive algorithm, which means it contains a system estimator. After fine-tuning the L_1 adaptive controller, the estimator's parameters can be saved and abstracted as a system model. This system model could then be used for off-line reinforcement learning control studies using simulations.

For the ultrasound and UR3 studies, the computer vision for detecting the swimmer from the ultrasound image is not robust. The demonstrated case is relatively simple compared to the clinical application. Some advanced algorithms and techniques should be implemented to detect high-dimension or complex environments better. Computer vision studies of machine learning and deep learning should be investigated in future work. As the current work demonstrated, the ultrasound

image could be lost during the transmission between Matlab PC and ROS PC, causing the task to fail and the robot arm's jerky movement. The hard drive disk (HDD) can be replaced by a solid-state drive (SSD) to improve the reading and writing speed. The impedance control is one necessary component of the blood clot studies. The robust control algorithm should be implemented rather than a PID controller. The feedback linearization control of the robot arm and other hybrid control structures such as the inner-outer loop should be investigated in future work. The experimental setup should also be improved in future work as following:

1. A stable base of the robot arm.
2. Replace the phased array transducer with a linear array transducer to fix the distortion problem.
3. PMDS workspace design for high dimension studies.
4. Improve the force sensor and measurement accuracy by optimizing the transducer holder with finite element analysis software.

This dissertation is just the beginning! There are many avenues for future work.

References

- [1] S. Yim and M. Sitti, "Design and rolling locomotion of a magnetically actuated soft capsule endoscope," *IEEE Transactions on Robotics*, vol. 28, no. 1, pp. 183–194, 2011.
- [2] O. Ergeneman, G. Dogangil, M. P. Kummer, J. J. Abbott, M. K. Nazeeruddin, and B. J. Nelson, "A magnetically controlled wireless optical oxygen sensor for intraocular measurements," *IEEE Sensors Journal*, vol. 8, no. 1, pp. 29–37, 2008.
- [3] S. Martel, J.-B. Mathieu, O. Felfoul, A. Chanu, E. Aboussouan, S. Tamaz, P. Pouponneau, L. Yahia, G. Beaudoin, and G. Soulez, "Automatic navigation of an untethered device in the artery of a living animal using a conventional clinical magnetic resonance imaging system," *Applied physics letters*, vol. 90, no. 11, p. 114105, 2007.
- [4] F. Munoz, G. Alici, and W. Li, "A review of drug delivery systems for capsule endoscopy," *Advanced drug delivery reviews*, vol. 71, pp. 77–85, 2014.
- [5] S. P. Woods and T. G. Constandinou, "Wireless capsule endoscope for targeted drug delivery: mechanics and design considerations," *IEEE Transactions on Biomedical Engineering*, vol. 60, no. 4, pp. 945–953, 2012.
- [6] J. Cui, X. Zheng, W. Hou, Y. Zhuang, X. Pi, and J. Yang, "The study of a remote-controlled gastrointestinal drug delivery and sampling system," *Telemedicine and e-Health*, vol. 14, no. 7, pp. 715–719, 2008.
- [7] P. Xitian, L. Hongying, W. Kang, L. Yulin, Z. Xiaolin, and W. Zhiyu, "A novel remote controlled capsule for site-specific drug delivery in human gi tract," *International Journal of Pharmaceutics*, vol. 382, no. 1-2, pp. 160–164, 2009.

- [8] S. Yim, K. Goyal, and M. Sitti, "Magnetically actuated soft capsule with the multimodal drug release function," *IEEE/ASME Transactions on Mechatronics*, vol. 18, no. 4, pp. 1413–1418, 2013.
- [9] K. E. Peyer, S. Tottori, F. Qiu, L. Zhang, and B. J. Nelson, "Magnetic helical micromachines," *Chemistry—A European Journal*, vol. 19, no. 1, pp. 28–38, 2013.
- [10] F. Qiu and B. J. Nelson, "Magnetic helical micro-and nanorobots: Toward their biomedical applications," *Engineering*, vol. 1, no. 1, pp. 021–026, 2015.
- [11] T. Xu, J. Yu, X. Yan, H. Choi, and L. Zhang, "Magnetic actuation based motion control for microrobots: An overview," *Micromachines*, vol. 6, no. 9, pp. 1346–1364, 2015.
- [12] K. Ishiyama, M. Sendoh, and K. Arai, "Magnetic micromachines for medical applications," *Journal of Magnetism and Magnetic Materials*, vol. 242, pp. 41–46, 2002.
- [13] V. Agrawal, W. J. Peine, and B. Yao, "Modeling of transmission characteristics across a cable-conduit system," *IEEE Transactions on Robotics*, vol. 26, no. 5, pp. 914–924, 2010.
- [14] G. Palli, G. Borghesan, and C. Melchiorri, "Modeling, identification, and control of tendon-based actuation systems," *IEEE Transactions on Robotics*, vol. 28, no. 2, pp. 277–290, 2012.
- [15] R. Dhaouadi, K. Kubo, and M. Tobise, "Two-degree-of-freedom robust speed controller for high-performance rolling mill drives," *IEEE transactions on industry applications*, vol. 29, no. 5, pp. 919–926, 1993.
- [16] H. Elliott, T. Depkovich, J. Kelly, and B. Draper, "Nonlinear adaptive control of mechanical linkage systems with application to robotics," in *American Control Conference, 1983*. IEEE, 1983, pp. 1050–1055.

- [17] D. McCloy and H. R. Martin, "Control of fluid power: analysis and design," *Chichester, Sussex, England, Ellis Horwood, Ltd.; New York, Halsted Press, 1980. 505 p.*, 1980.
- [18] R. S. Hartenberg and J. Denavit, *Kinematic synthesis of linkages*. McGraw-Hill, 1964.
- [19] A. Salimi, A. Ramezanifar, J. Mohammadpour, and K. Grigoriadis, "Gain-scheduling control of a cable-driven MRI-compatible robotic platform for intracardiac interventions," in *American Control Conference (ACC), 2013*. IEEE, 2013, pp. 746–751.
- [20] N. V. Tsekos, A. Khanicheh, E. Christoforou, and C. Mavroidis, "Magnetic resonance-compatible robotic and mechatronics systems for image-guided interventions and rehabilitation: a review study," *Annu. Rev. Biomed. Eng.*, vol. 9, pp. 351–387, 2007.
- [21] T. Fisher, A. Hamed, P. Vartholomeos, K. Masamune, G. Tang, H. Ren, and Z. T. Tse, "Intra-operative magnetic resonance imaging-conditional robotic devices for therapy and diagnosis," *Proceedings of the Institution of Mechanical Engineers, Part H: Journal of Engineering in Medicine*, vol. 228, no. 3, pp. 303–318, 2014.
- [22] P. Mozer, J. Troccaz, and D. Stoianovici, "Urologic robots and future directions," *Current opinion in urology*, vol. 19, no. 1, p. 114, 2009.
- [23] M. Moche, D. Zajonz, T. Kahn, and H. Busse, "MRI-guided procedures in various regions of the body using a robotic assistance system in a closed-bore scanner: Preliminary clinical experience and limitations," *Journal of Magnetic Resonance Imaging*, vol. 31, no. 4, pp. 964–974, 2010.
- [24] M. M. Arnolli, N. C. Hanumara, M. Franken, D. M. Brouwer, and I. A. Broeders, "An overview of systems for CT-and MRI-guided percutaneous needle placement in the thorax and abdomen," *The International Journal of Medical Robotics and Computer Assisted*

Surgery, vol. 11, no. 4, pp. 458–475, 2015.

- [25] G. S. Fischer, A. Krieger, I. Iordachita, C. Csoma, L. L. Whitcomb, and G. Fichtinger, “MRI compatibility of robot actuation techniques—a comparative study,” in *International Conference on Medical Image Computing and Computer-Assisted Intervention*. Springer, 2008, pp. 509–517.
- [26] N. V. Tsekos, E. Yacoub, P. V. Tsekos, and I. G. Koutlas, “Design of an MRI-compatible robotic stereotactic device for minimally invasive interventions in the breast,” *J. Biomechanical Eng.*, vol. 126, no. 4, pp. 458–465, 2004.
- [27] G. Li, H. Su, G. A. Cole, W. Shang, K. Harrington, A. Camilo, J. G. Pilitsis, and G. S. Fischer, “Robotic system for MRI-guided stereotactic neurosurgery,” *IEEE Transactions on Biomedical Engineering*, vol. 62, no. 4, pp. 1077–1088, 2015.
- [28] N. V. Tsekos, A. Özcan, and E. Christoforou, “A prototype manipulator for magnetic resonance-guided interventions inside standard cylindrical magnetic resonance imaging scanners,” *Journal of Biomechanical Engineering*, vol. 127, no. 6, pp. 972–980, 2005.
- [29] A. Krieger, I. Iordachita, S.-E. Song, N. B. Cho, P. Guion, G. Fichtinger, and L. L. Whitcomb, “Development and preliminary evaluation of an actuated MRI-compatible robotic device for MRI-guided prostate intervention,” in *Robotics and Automation (ICRA), 2010 IEEE International Conference on*. IEEE, 2010, pp. 1066–1073.
- [30] M. Muntener, A. Patriciu, D. Petrisor, D. Mazilu, H. Bagga, L. Kavoussi, K. Cleary, and D. Stoianovici, “Magnetic resonance imaging compatible robotic system for fully automated brachytherapy seed placement,” *Urology*, vol. 68, no. 6, pp. 1313–1317, 2006.

- [31] S.-E. Song, N. B. Cho, G. Fischer, N. Hata, C. Tempany, G. Fichtinger, and I. Iordachita, "Development of a pneumatic robot for MRI-guided transperineal prostate biopsy and brachytherapy: New approaches," in *Robotics and Automation (ICRA), 2010 IEEE International Conference on*. IEEE, 2010, pp. 2580–2585.
- [32] A. Kapoor, B. Wood, D. Mazilu, K. A. Horvath, and M. Li, "MRI-compatible hands-on cooperative control of a pneumatically actuated robot," in *Robotics and Automation, 2009. ICRA'09. IEEE International Conference on*. IEEE, 2009, pp. 2681–2686.
- [33] M. Li, A. Kapoor, D. Mazilu, and K. A. Horvath, "Pneumatic actuated robotic assistant system for aortic valve replacement under MRI guidance," *IEEE Transactions on Biomedical Engineering*, vol. 58, no. 2, pp. 443–451, 2011.
- [34] G. Ganesh, R. Gassert, E. Burdet, and H. Bleuler, "Dynamics and control of an MRI compatible master-slave system with hydrostatic transmission," in *Robotics and Automation, 2004. Proceedings. ICRA'04. 2004 IEEE International Conference on*, vol. 2. IEEE, 2004, pp. 1288–1294.
- [35] R. Gassert, R. Moser, E. Burdet, and H. Bleuler, "MRI/fMRI-compatible robotic system with force feedback for interaction with human motion," *IEEE/ASME transactions on mechatronics*, vol. 11, no. 2, pp. 216–224, 2006.
- [36] D. Stoianovici, A. Patriciu, D. Petrisor, D. Mazilu, and L. Kavoussi, "A new type of motor: pneumatic step motor," *IEEE/ASME Transactions On Mechatronics*, vol. 12, no. 1, pp. 98–106, 2007.
- [37] E. G. Christoforou, A. Ozcan, and N. V. Tsekos, "Robotic arm for magnetic resonance imaging guided interventions," in *Biomedical Robotics and Biomechanics, 2006. BioRob 2006*.

- The First IEEE/RAS-EMBS International Conference on.* IEEE, 2006, pp. 911–916.
- [38] A. A. Goldenberg, J. Trachtenberg, W. Kucharczyk, Y. Yi, M. Haider, L. Ma, R. Weersink, and C. Raoufi, “Robotic system for closed-bore MRI-guided prostatic interventions,” *IEEE/ASME Transactions On Mechatronics*, vol. 13, no. 3, pp. 374–379, 2008.
- [39] G. S. Fischer, G. Cole, and H. Su, “Approaches to creating and controlling motion in MRI,” in *Engineering in Medicine and Biology Society, EMBC, 2011 Annual International Conference of the IEEE.* IEEE, 2011, pp. 6687–6690.
- [40] A. E. Sonmez, A. G. Webb, W. M. Spees, A. Ozcan, and N. V. Tsekos, “A system for endoscopic mechanically scanned localized proton MR and light-induced fluorescence emission spectroscopies,” *Journal of Magnetic Resonance*, vol. 222, pp. 16–25, 2012.
- [41] N. Yu, C. Hollnagel, A. Blickenstorfer, S. S. Kollias, and R. Riener, “Comparison of MRI-compatible mechatronic systems with hydrodynamic and pneumatic actuation,” *IEEE/ASME transactions on mechatronics*, vol. 13, no. 3, pp. 268–277, 2008.
- [42] X. Liu, D. Biediger, R. Kopru, E. G. Christoforou, and N. V. Tsekos, “A new transmission mechanism for the actuation of manipulators for magnetic resonance imaging (MRI) guided interventions,” in *XIV Mediterranean Conference on Medical and Biological Engineering and Computing 2016.* Springer, 2016, pp. 673–678.
- [43] L. Huang, X. Liu, N. V. Tsekos, and A. T. Becker, “Two missing components for solid media transmission: Amplifiers and manifolds,” in *Automation Science and Engineering (CASE), 2016 IEEE International Conference on.* IEEE, 2016, pp. 207–212.

- [44] N. C. von Sternberg, J. An, K. Chin, D. J. Shah, and N. V. Tsekos, “A new method for MR compatible actuation: Solid media flexible transmission,” Joint Annual Meeting ISMRM-ESMRMB 2014, Milan, Italy, 2014.
- [45] N. V. Tsekos and M. J. Heffernan, “Robotic device for image-guided surgery and interventions,” Greek and German Patent US20170135772A1, May 18, 2017, US Patent App. 15/402,135. [Online]. Available: <https://patents.google.com/patent/US20170135772A1/en>
- [46] H. Zhao, X. Liu, H. M. Zaid, D. J. Shah, M. J. Heffernan, A. T. Becker, and N. V. Tsekos, “Early studies of a transmission mechanism for mr-guided interventions,” in *Bioinformatics and Bioengineering (BIBE), 2017 IEEE 17th International Conference on*. IEEE, 2017, pp. 450–456.
- [47] H. Zhao and A. T. Becker, *BlockPushingIROS2015*, March 2017. [Online]. Available: <https://github.com/RoboticSwarmControl/SMT1m1DOFpaper/code>
- [48] K. J. Åström and B. Wittenmark, *Computer-controlled systems: theory and design*. Courier Corporation, 2013.
- [49] M. Nordin and P.-O. Gutman, “Controlling mechanical systems with backlash, a survey,” *Automatica*, vol. 38, no. 10, pp. 1633–1649, 2002.
- [50] J. Tal, “General dual loop improves backlash compensation,” *ServoTrends*, vol. 14, no. 4, pp. 3–4, 1998.
- [51] H. Garnier, M. Mensler, and A. Richard, “Continuous-time model identification from sampled data: implementation issues and performance evaluation,” *International Journal of Control*, vol. 76, no. 13, pp. 1337–1357, 2003.

- [52] L. Ljung, "Experiments with identification of continuous time models," *IFAC Proceedings Volumes*, vol. 42, no. 10, pp. 1175–1180, 2009.
- [53] N. C. von Sternberg, Y. S. Hedayati, H. M. Zaid, E. Yeniaras, E. Christoforou, and N. V. Tsekos, "An actuated phantom for developing and studying MRI-guided interventions in dynamic environments," in *Biomedical Robotics and Biomechatronics (BioRob), 2012 4th IEEE RAS & EMBS International Conference on*. IEEE, 2012, pp. 1669–1674.
- [54] *Standard Practice for Marking Medical Devices and Other Items for Safety in the Magnetic Resonance Environment*, American Society for Testing and Materials International, West Conshohocken, PA, 2003.
- [55] "Three multileaf collimators," <http://www.maxonmotorusa.com/maxon/view/content/application/viewray>.
- [56] M. S. Jackson, S. R. Igo, T. E. Lindsey, D. Maragiannis, K. E. Chin, K. Autry, R. Schutt III, D. J. Shah, P. Valsecchi, and W. B. Kline, "Development of a multi-modality compatible flow loop system for the functional assessment of mitral valve prostheses," *Cardiovascular Engineering and Technology*, vol. 5, no. 1, pp. 13–24, 2014.
- [57] F. J. Perez-Pinal, C. Nunez, R. Alvarez, and I. Cervantes, "Comparison of multi-motor synchronization techniques," in *IEEE Industrial Electronics Society. Annual conference*, 2004.
- [58] B. J. Nelson, I. K. Kaliakatsos, and J. J. Abbott, "Microrobots for minimally invasive medicine," *Annual review of biomedical engineering*, vol. 12, pp. 55–85, 2010.
- [59] S. Tottori, L. Zhang, F. Qiu, K. K. Krawczyk, A. Franco-Obregón, and B. J. Nelson, "Magnetic helical micromachines: fabrication, controlled swimming, and cargo transport," *Advanced materials*, vol. 24, no. 6, pp. 811–816, 2012.

- [60] K. E. Peyer, L. Zhang, and B. J. Nelson, “Bio-inspired magnetic swimming microrobots for biomedical applications,” *Nanoscale*, vol. 5, no. 4, pp. 1259–1272, 2013.
- [61] H. C. Berg and R. A. Anderson, “Bacteria swim by rotating their flagellar filaments,” *Nature*, vol. 245, no. 5425, p. 380, 1973.
- [62] E. M. Purcell, “Life at low Reynolds number,” *American Journal of Physics*, vol. 45, no. 1, pp. 3–11, 1977.
- [63] T. Honda, K. Arai, and K. Ishiyama, “Micro swimming mechanisms propelled by external magnetic fields,” *IEEE Transactions on Magnetics*, vol. 32, no. 5, pp. 5085–5087, 1996.
- [64] A. W. Mahoney, J. C. Sarrazin, E. Bamberg, and J. J. Abbott, “Velocity control with gravity compensation for magnetic helical microswimmers,” *Advanced Robotics*, vol. 25, no. 8, pp. 1007–1028, 2011.
- [65] M. E. Alshafeei, A. Hosney, A. Klingner, S. Misra, and I. S. Khalil, “Magnetic-based motion control of a helical robot using two synchronized rotating dipole fields,” in *5th IEEE RAS/EMBS International Conference on Biomedical Robotics and Biomechanics*, 2014, pp. 151–156.
- [66] T. Xu, Y. Guan, J. Liu, and X. Wu, “Image-based visual servoing of helical microswimmers for planar path following,” *IEEE Transactions on Automation Science and Engineering*, 2019.
- [67] K. Yoshida and H. Onoe, “Soft spiral-shaped micro-swimmer with propulsion force control by pitch change,” in *2019 20th International Conference on Solid-State Sensors, Actuators and Microsystems & Eurosensors XXXIII (TRANSDUCERS & EUROSENSORS XXXIII)*. IEEE, 2019, pp. 217–220.

- [68] A. Oulmas, N. Andreff, and S. Régnier, “Closed-loop 3D path following of scaled-up helical microswimmers,” in *2016 IEEE International Conference on Robotics and Automation (ICRA)*. IEEE, 2016, pp. 1725–1730.
- [69] T. Xu, G. Hwang, N. Andreff, and S. Régnier, “Planar path following of 3-D steering scaled-up helical microswimmers,” *IEEE Transactions on Robotics*, vol. 31, no. 1, pp. 117–127, 2015.
- [70] J. Van Bladel and J. Van Bladel, *Singular electromagnetic fields and sources*. Clarendon Press Oxford, 1991.
- [71] T. W. Fountain, P. V. Kailat, and J. J. Abbott, “Wireless control of magnetic helical micro-robots using a rotating-permanent-magnet manipulator,” in *2010 IEEE International Conference on Robotics and Automation*. IEEE, 2010, pp. 576–581.
- [72] L. Yang, X. Du, E. Yu, D. Jin, and L. Zhang, “Deltamag: An electromagnetic manipulation system with parallel mobile coils,” in *2019 International Conference on Robotics and Automation (ICRA)*. IEEE, 2019, pp. 9814–9820.
- [73] Z. Yang, L. Yang, and L. Zhang, “3D visual servoing of magnetic miniature swimmers using parallel mobile coils,” *IEEE Transactions on Medical Robotics and Bionics*, 2020.
- [74] K. Ishiyama, M. Sendoh, A. Yamazaki, and K. Arai, “Swimming micro-machine driven by magnetic torque,” *Sensors and Actuators A: Physical*, vol. 91, no. 1-2, pp. 141–144, 2001.
- [75] K. Ishiyama, K. Arai, M. Sendoh, and A. Yamazaki, “Spiral-type micro-machine for medical applications,” in *MHS2000. Proceedings of 2000 International Symposium on Micromechanics and Human Science (Cat. No. 00TH8530)*. IEEE, 2000, pp. 65–69.

- [76] H. Zhou, G. Alici, T. D. Than, and W. Li, "Modeling and experimental characterization of propulsion of a spiral-type microrobot for medical use in gastrointestinal tract," *IEEE Transactions on Biomedical engineering*, vol. 60, no. 6, pp. 1751–1759, 2012.
- [77] J. Leclerc, Z. Haoran, and A. T. Becker, "3D control of rotating millimeter-scale swimmers through obstacles," *IEEE International Conference on Robotics and Automation*, p. forthcoming, 2019.
- [78] J. Leclerc, H. Zhao, D. Z. Bao, A. T. Becker, M. Ghosn, and D. J. Shah, "Agile 3D-navigation of a helical magnetic swimmer," in *2020 IEEE International Conference on Robotics and Automation (ICRA)*. IEEE, 2020, pp. 7638–7644.
- [79] J. Leclerc, H. Zhao, D. Bao, and A. T. Becker, "In vitro design investigation of a rotating helical magnetic swimmer for combined 3-D navigation and blood clot removal," *IEEE Transactions on Robotics*, 2020.
- [80] H. Zhao, J. Leclerc, M. Feucht, O. Bailey, and A. T. Becker, "3D path-following using mrac on a millimeter-scale spiral-type magnetic robot," *IEEE Robotics and Automation Letters*, vol. 5, no. 2, pp. 1564–1571, 2020.
- [81] J. Leclerc, B. Isichei, and A. T. Becker, "A magnetic manipulator cooled with liquid nitrogen," *IEEE Robotics and Automation Letters*, vol. 3, no. 4, pp. 4367–4374, 2018.
- [82] J. C. Simpson, J. E. Lane, C. D. Immer, and R. C. Youngquist, "Simple analytic expressions for the magnetic field of a circular current loop," NASA, Kennedy Space Center, Florida, Tech. Rep., 2001. [Online]. Available: <https://ntrs.nasa.gov/archive/nasa/casi.ntrs.nasa.gov/20140002333.pdf>

- [83] M. P. Kummer, J. J. Abbott, B. E. Kratochvil, R. Borer, A. Sengul, and B. J. Nelson, "Oc-tomag: An electromagnetic system for 5-DoF wireless micromanipulation," *IEEE Transactions on Robotics*, vol. 26, no. 6, pp. 1006–1017, 2010.
- [84] A. N. Tikhonov, A. Goncharsky, V. Stepanov, and A. G. Yagola, *Numerical Methods for the Solution of Ill-posed Problems*. Springer Science & Business Media, 2013, vol. 328.
- [85] H. Kaufman, I. Barkana, and K. Sobel, *Direct adaptive control algorithms: theory and applications*. Springer Science & Business Media, 2012.
- [86] D. Zhang and B. Wei, "Convergence performance comparisons of pid, mrac, and pid+ mrac hybrid controller," *Frontiers of Mechanical Engineering*, vol. 11, no. 2, pp. 213–217, 2016.
- [87] S. Xiao, Y. Li, and J. Liu, "A model reference adaptive pid control for electromagnetic actuated micro-positioning stage," in *2012 IEEE International Conference on Automation Science and Engineering (CASE)*. IEEE, 2012, pp. 97–102.
- [88] P. Jain and M. Nigam, "Design of a model reference adaptive controller using modified mit rule for a second order system," *Advance in Electronic and Electric Engineering*, vol. 3, no. 4, pp. 477–484, 2013.
- [89] T. Yucelen, "Model reference adaptive control," *Wiley Encyclopedia of Electrical and Electronics Engineering*, pp. 1–13, 2019.
- [90] L. J. J. Scheres, W. M. Lijfering, and S. C. Cannegieter, "Current and future burden of venous thrombosis: Not simply predictable," *Research and Practice in Thrombosis and Haemostasis*, vol. 2, no. 2, pp. 199–208, 2018. [Online]. Available: <https://onlinelibrary.wiley.com/doi/abs/10.1002/rth2.12101>

- [91] D. D. Ribeiro, W. M. Lijfering, S. M. Barreto, F. R. Rosendaal, and S. M. Rezende, “Epidemiology of recurrent venous thrombosis,” *Brazilian Journal of Medical and Biological Research*, vol. 45, no. 1, pp. 1–7, 2012.
- [92] I. A. Næss, S. Christiansen, P. Romundstad, S. Cannegieter, F. R. Rosendaal, and J. Hammerstrøm, “Incidence and mortality of venous thrombosis: a population-based study,” *Journal of Thrombosis and Haemostasis*, vol. 5, no. 4, pp. 692–699, 2007.
- [93] M. Cushman, “Epidemiology and risk factors for venous thrombosis,” *Seminars in hematology*, vol. 44, no. 2, pp. 62–69, 2007.
- [94] V. Tagalakakis, V. Patenaude, S. R. Kahn, and S. Suissa, “Incidence of and mortality from venous thromboembolism in a real-world population: the Q-VTE study cohort,” *The American Journal of Medicine*, vol. 126, no. 9, pp. 832–e13, 2013.
- [95] J. A. Heit, “The epidemiology of venous thromboembolism in the community,” *Arteriosclerosis, thrombosis, and vascular biology*, vol. 28, no. 3, pp. 370–372, 2008.
- [96] A. M. Wendelboe and G. E. Raskob, “Global burden of thrombosis,” *Circulation Research*, vol. 118, no. 9, pp. 1340–1347, 2016. [Online]. Available: <https://www.ahajournals.org/doi/abs/10.1161/CIRCRESAHA.115.306841>
- [97] C. Castaño, L. Dorado, C. Guerrero, M. Millán, M. Gomis, N. Perez de la Ossa, M. Castellanos, M. R. García, S. Domenech, and A. Dávalos, “Mechanical thrombectomy with the solitaire ab device in large artery occlusions of the anterior circulation: a pilot study,” *Stroke*, vol. 41, no. 8, pp. 1836–1840, 2010.

- [98] W. S. Smith, G. Sung, J. Saver, R. Budzik, G. Duckwiler, D. S. Liebeskind, H. L. Lutsep, M. M. Rymer, R. T. Higashida, and S. Starkman, "Mechanical thrombectomy for acute ischemic stroke: final results of the multi merci trial," *Stroke*, vol. 39, no. 4, pp. 1205–1212, 2008.
- [99] J. E. Delgado Almandoz, Y. Kayan, M. L. Young, J. L. Fease, J. M. Scholz, A. M. Milner, T. H. Hehr, P. Roohani, M. Mulder, and R. M. Tarrel, "Comparison of clinical outcomes in patients with acute ischemic strokes treated with mechanical thrombectomy using either solumbra or adapt techniques," *Journal of NeuroInterventional Surgery*, vol. 8, no. 11, pp. 1123–1128, 2016. [Online]. Available: <https://jn.is.bmj.com/content/8/11/1123>
- [100] E. Zeitler, W. Schoop, and W. Zahnw, "The Treatment of Occlusive Arterial Disease by Transluminal Catheter Angioplasty," *Radiology*, vol. 99, no. 1, pp. 19–26, apr 1971. [Online]. Available: <http://pubs.rsna.org/doi/10.1148/99.1.19>
- [101] G. Thomalla, C. Schwark, J. Sobesky, E. Bluhmki, J. B. Fiebach, J. Fiehler, O. Zaro Weber, T. Kucinski, E. Juettler, and P. A. Ringleb, "Outcome and symptomatic bleeding complications of intravenous thrombolysis within 6 hours in MRI-selected stroke patients: comparison of a german multicenter study with the pooled data of atlantis, ecass, and ninds tpa trials," *Stroke*, vol. 37, no. 3, pp. 852–858, 2006.
- [102] S. Schulman, R. J. Beyth, C. Kearon, and M. N. Levine, "Hemorrhagic complications of anticoagulant and thrombolytic treatment: American college of chest physicians evidence-based clinical practice guidelines," *Chest*, vol. 133, no. 6, pp. 257S–298S, 2008.
- [103] M. Hamon, J.-C. Baron, F. Viader, and M. Hamon, "Periprocedural Stroke and Cardiac Catheterization," *Circulation*, vol. 118, no. 6, pp. 678–683, aug 2008. [Online]. Available: <https://www.ahajournals.org/doi/10.1161/CIRCULATIONAHA.108.784504>

- [104] P. Khatri and S. E. Kasner, "Ischemic Strokes After Cardiac Catheterization," *Archives of Neurology*, vol. 63, no. 6, p. 817, jun 2006.
- [105] F. Ullrich, F. Qiu, J. Pokki, T. Huang, S. Pane, and B. J. Nelson, "Swimming characteristics of helical microrobots in fibrous environments," in *2016 6th IEEE International Conference on Biomedical Robotics and Biomechanics (BioRob)*. IEEE, jun 2016, pp. 470–475. [Online]. Available: <http://ieeexplore.ieee.org/document/7523671/>
- [106] A. Hosney, A. Klingner, S. Misra, and I. S. M. Khalil, "Propulsion and steering of helical magnetic microrobots using two synchronized rotating dipole fields in three-dimensional space," in *2015 IEEE/RSJ International Conference on Intelligent Robots and Systems (IROS)*. IEEE, sep 2015, pp. 1988–1993. [Online]. Available: <http://ieeexplore.ieee.org/document/7353639/>
- [107] T. Xu, G. Hwang, N. Andreff, and S. Regnier, "Planar Path Following of 3-D Steering Scaled-Up Helical Microswimmers," *IEEE Transactions on Robotics*, vol. 31, no. 1, pp. 117–127, feb 2015. [Online]. Available: <http://ieeexplore.ieee.org/document/7015549/>
- [108] W. Lee, S. Jeon, J. Nam, and G. Jang, "Dual-body magnetic helical robot for drilling and cargo delivery in human blood vessels," *Journal of Applied Physics*, vol. 117, no. 17, p. 17B314, may 2015. [Online]. Available: <http://aip.scitation.org/doi/10.1063/1.4917067>
- [109] T. Xu, G. Hwang, N. Andreff, and S. Regnier, "Characterization of three-dimensional steering for helical swimmers," in *2014 IEEE International Conference on Robotics and Automation (ICRA)*. IEEE, may 2014, pp. 4686–4691. [Online]. Available: <http://ieeexplore.ieee.org/document/6907544/>

- [110] A. W. Mahoney, N. D. Nelson, K. E. Peyer, B. J. Nelson, and J. J. Abbott, "Behavior of rotating magnetic microrobots above the step-out frequency with application to control of multi-microrobot systems," *Applied Physics Letters*, vol. 104, no. 14, p. 144101, apr 2014. [Online]. Available: <http://aip.scitation.org/doi/10.1063/1.4870768>
- [111] K. Ishiyama, K. Arai, M. Sendoh, and A. Yamazaki, "Spiral-type micro-machine for medical applications," in *MHS2000. Proceedings of 2000 International Symposium on Micromechatronics and Human Science (Cat. No.00TH8530)*. IEEE, 2000, pp. 65–69. [Online]. Available: <http://ieeexplore.ieee.org/document/903292/>
- [112] W. Gao, X. Feng, A. Pei, C. R. Kane, R. Tam, C. Hennessy, and J. Wang, "Bioinspired Helical Microswimmers Based on Vascular Plants," *Nano Letters*, vol. 14, no. 1, pp. 305–310, jan 2014. [Online]. Available: <http://pubs.acs.org/doi/10.1021/nl404044d>
- [113] I. S. M. Khalil, D. Mahdy, A. E. Sharkawy, R. R. Moustafa, A. F. Tabak, M. E. Mitwally, S. Hesham, N. Hamdi, A. Klingner, A. Mohamed, and M. Sitti, "Mechanical Rubbing of Blood Clots Using Helical Robots Under Ultrasound Guidance," *IEEE Robotics and Automation Letters*, vol. 3, no. 2, pp. 1112–1119, apr 2018. [Online]. Available: <http://ieeexplore.ieee.org/document/8253812/>
- [114] I. S. M. Khalil, A. F. Tabak, K. Sadek, D. Mahdy, N. Hamdi, and M. Sitti, "Rubbing Against Blood Clots Using Helical Robots: Modeling and In Vitro Experimental Validation," *IEEE Robotics and Automation Letters*, vol. 2, no. 2, pp. 927–934, apr 2017. [Online]. Available: <http://ieeexplore.ieee.org/document/7820160/>
- [115] I. S. Khalil, D. Mahdy, A. El Sharkawy, R. R. Moustafa, A. F. Tabak, M. E. Mitwally, S. Hesham, N. Hamdi, A. Klingner, and A. Mohamed, "Mechanical rubbing of blood clots using

- helical robots under ultrasound guidance,” *IEEE Robotics and Automation Letters*, vol. 3, no. 2, pp. 1112–1119, 2018.
- [116] D. Mahdy, R. Reda, N. Hamdi, and I. S. Khalil, “Ultrasound-guided minimally invasive grinding for clearing blood clots: promises and challenges,” *IEEE Instrumentation & Measurement Magazine*, vol. 21, no. 2, pp. 10–14, 2018.
- [117] I. S. Khalil, A. F. Tabak, K. Sadek, D. Mahdy, N. Hamdi, and M. Sitti, “Rubbing against blood clots using helical robots: modeling and in vitro experimental validation,” *IEEE Robotics and Automation Letters*, vol. 2, no. 2, pp. 927–934, 2017.
- [118] S. Lee, S. Lee, S. Kim, C.-H. Yoon, H.-J. Park, J.-Y. Kim, and H. Choi, “Fabrication and characterization of a magnetic drilling actuator for navigation in a three-dimensional phantom vascular network,” *Scientific reports*, vol. 8, no. 1, p. 3691, 2018.
- [119] X. Wu, J. Liu, C. Huang, M. Su, and T. Xu, “3-D path following of helical microswimmers with an adaptive orientation compensation model,” *IEEE Transactions on Automation Science and Engineering*, 2019.
- [120] A. Oulmas, N. Andreff, and S. Régnier, “3D closed-loop swimming at low reynolds numbers,” *The International Journal of Robotics Research*, vol. 37, no. 11, pp. 1359–1375, 2018.
- [121] H. Zhao, L. Julien, M. Feucht, O. Bailey, and A. Becker, “3D path-following using mrac on a millimeter-scale spiral-type magnetic robot,” *IEEE Robotics and Automation Letters*, pp. 1–1, 2020.
- [122] N. Korin, M. Kanapathipillai, B. D. Matthews, M. Crescente, A. Brill, T. Mammoto, K. Ghosh, S. Jurek, S. A. Bencherif, and D. Bhatta, “Shear-activated nanotherapeutics for drug targeting to obstructed blood vessels,” *Science*, p. 1217815, 2012.

- [123] R. A. Freitas, “Nanotechnology, nanomedicine and nanosurgery,” *International Journal of Surgery*, vol. 4, no. 3, pp. 243–246, 2005.
- [124] M. Vonthron, V. Lalande, G. Bringout, C. Tremblay, and S. Martel, “A mri-based integrated platform for the navigation of micro-devices and microrobots,” in *2011 IEEE/RSJ International Conference on Intelligent Robots and Systems*. IEEE, 2011, pp. 1285–1290.
- [125] “Parameters for calculations of kinematics and dynamics,” <https://www.universal-robots.com/articles/ur/parameters-for-calculations-of-kinematics-and-dynamics/>, 2020-08.
- [126] M. W. Gilbertson and B. W. Anthony, “Ergonomic control strategies for a handheld force-controlled ultrasound probe,” in *2012 IEEE/RSJ International Conference on Intelligent Robots and Systems*. IEEE, 2012, pp. 1284–1291.
- [127] T. Schimmoeller, R. Colbrunn, T. Nagle, M. Lobosky, E. E. Neumann, T. M. Owings, B. Landis, J. E. Jelovsek, and A. Erdemir, “Instrumentation of off-the-shelf ultrasound system for measurement of probe forces during freehand imaging,” *Journal of Biomechanics*, vol. 83, pp. 117–124, 2019.
- [128] J. De Schutter and H. Van Brussel, “Compliant robot motion i. a formalism for specifying compliant motion tasks,” *The International Journal of Robotics Research*, vol. 7, no. 4, pp. 3–17, 1988.
- [129] S. Chiaverini and L. Sciavicco, “The parallel approach to force/position control of robotic manipulators,” *IEEE Transactions on Robotics and Automation*, vol. 9, no. 4, pp. 361–373, 1993.

- [130] J. Roy and L. L. Whitcomb, “Adaptive force control of position/velocity controlled robots: theory and experiment,” *IEEE Transactions on Robotics and Automation*, vol. 18, no. 2, pp. 121–137, 2002.
- [131] Y. Li, S. Sam Ge, and C. Yang, “Learning impedance control for physical robot–environment interaction,” *International Journal of Control*, vol. 85, no. 2, pp. 182–193, 2012.
- [132] T. Tsuji, K. Ito, and P. G. Morasso, “Neural network learning of robot arm impedance in operational space,” *IEEE Transactions on Systems, Man, and Cybernetics, Part B (Cybernetics)*, vol. 26, no. 2, pp. 290–298, 1996.
- [133] R. J. Anderson and M. W. Spong, “Hybrid impedance control of robotic manipulators,” *IEEE Journal on Robotics and Automation*, vol. 4, no. 5, pp. 549–556, 1988.
- [134] J. Luh, M. Walker, and R. Paul, “Resolved-acceleration control of mechanical manipulators,” *IEEE Transactions on Automatic Control*, vol. 25, no. 3, pp. 468–474, 1980.
- [135] MathWorks, *Robot Operating System (ROS)*, 2020. [Online]. Available: <https://www.mathworks.com/help/ros/gs/robot-operating-system-ros.html>
- [136] E. Hulse and G. Thomas, “Vascular access on the 21st century military battlefield,” *Journal of the Royal Army Medical Corps*, vol. 156, pp. 385–90, 12 2010.
- [137] E. Kharisov, N. Hovakimyan, and K. Astrom, “Comparison of several adaptive controllers according to their robustness metrics,” in *AIAA Guidance, Navigation, and Control Conference*, 2012. [Online]. Available: <https://arc.aiaa.org/doi/abs/10.2514/6.2010-8047>

